



**UNIVERSIDADE ESTADUAL DE CAMPINAS**

Faculdade de Engenharia Mecânica

**DANILO BRAGHINI**

**Stability and Performance of Non-Reciprocal  
Metastructures Exhibiting the Non-Hermitian Skin  
Effect**

*Estabilidade e Desempenho de Metaestruturas  
Não-Recíprocas Exibindo o Efeito Pelicular  
Não-Hermitiano*

Campinas

2024

DANILO BRAGHINI

**Stability and Performance of Non-Reciprocal  
Metastructures Exhibiting the Non-Hermitian Skin  
Effect**

*Estabilidade e Desempenho de Metaestruturas  
Não-Recíprocas Exibindo o Efeito Pelicular  
Não-Hermitiano*

Master's Thesis submitted to the School of Mechanical Engineering at the State University of Campinas in partial fulfillment of the requirements for the degree of Master of Science in Mechanical Engineering, with a focus in Solid Mechanics and Mechanical Design.

Dissertação de Mestrado Acadêmico apresentada à Faculdade de Engenharia Mecânica da Universidade Estadual de Campinas como parte dos requisitos exigidos para a obtenção do título de Mestre em Engenharia Mecânica, na Área de Mecânica dos Sólidos e Projeto Mecânico.

Orientador: Prof. Dr. José Roberto de França Arruda

ESTE TRABALHO CORRESPONDE À VERSÃO FINAL DA DISSERTAÇÃO DE MESTRADO ACADÊMICO DEFENDIDA PELO ALUNO DANILO BRAGHINI, E ORIENTADA PELO PROF. DR. JOSÉ ROBERTO DE FRANÇA ARRUDA.

Campinas

2024

Ficha catalográfica  
Universidade Estadual de Campinas (UNICAMP)  
Biblioteca da Área de Engenharia e Arquitetura  
Elizangela Aparecida dos Santos Souza - CRB 8/8098

B730s Braghini, Danilo, 1996-  
Stability and performance of non-reciprocal metastructures exhibiting the non-hermitian skin effect / Danilo Braghini. – Campinas, SP : [s.n.], 2024.

Orientador: José Roberto de França Arruda.  
Dissertação (mestrado) – Universidade Estadual de Campinas (UNICAMP), Faculdade de Engenharia Mecânica.

1. Metamateriais. 2. Estabilidade. 3. Teoria do controle. 4. Física aplicada. 5. Física da matéria condensada. I. Arruda, José Roberto de França, 1954-. II. Universidade Estadual de Campinas (UNICAMP). Faculdade de Engenharia Mecânica. III. Título.

Informações Complementares

**Título em outro idioma:** Estabilidade e desempenho de metaestruturas não-recíprocas exibindo o efeito pelicular não-hermitiano

**Palavras-chave em inglês:**

Metamaterials

Stability

Control theory

Applied physics

Condensed matter physics

**Área de concentração:** Mecânica dos Sólidos e Projeto Mecânico

**Titulação:** Mestre em Engenharia Mecânica

**Banca examinadora:**

José Roberto de França Arruda [Orientador]

Alberto Luiz Serpa

Carlos De Marqui Jr.

**Data de defesa:** 12-07-2024

**Programa de Pós-Graduação:** Engenharia Mecânica

**Identificação e informações acadêmicas do(a) aluno(a)**

- ORCID do autor: <https://orcid.org/0000-0003-2469-0213>

- Currículo Lattes do autor: <http://lattes.cnpq.br/4475647290285786>

**UNIVERSIDADE ESTADUAL DE CAMPINAS  
FACULDADE DE ENGENHARIA MECÂNICA**

**DISSERTAÇÃO DE MESTRADO ACADÊMICO**

**Stability and Performance of Non-Reciprocal  
Metastructures Exhibiting the Non-Hermitian Skin  
Effect**

*Estabilidade e Desempenho de Metaestruturas  
Não-Recíprocas Exibindo o Efeito Pelicular  
Não-Hermitiano*

Autor: Danilo Braghini

Orientador: Prof. Dr. José Roberto de França Arruda

A Banca Examinadora composta pelos membros abaixo aprovou esta Dissertação de Mestrado Acadêmico:

**Prof. Dr. José Roberto de França Arruda, Presidente**  
Departamento de Mecânica Computacional/ Faculdade de Engenharia Mecânica/  
UNICAMP

**Prof. Dr. Alberto Luiz Serpa**  
Departamento de Mecânica Computacional/ Faculdade de Engenharia Mecânica/  
UNICAMP

**Prof. Dr. Carlos De Marqui Junior**  
Departamento de Engenharia Aeronáutica/ Escola de Engenharia de São Carlos/ USP

A Ata de Defesa com as respectivas assinaturas dos membros encontra-se no SIGA/Sistema de Fluxo de Dissertação/Tese e na Secretaria do Programa da Unidade.

Campinas, 12 de Julho de 2024

*Aos meus pais, Luis Augusto e Eliana da Silva,  
A minha esposa, Karen Nardi,  
e a minha avó, Nilda Belcorso.*

## ACKNOWLEDGEMENTS

This work would be hardly possible without the financial aid provided by the São Paulo Research Foundation (FAPESP), which supported my master's in Brazil and an internship abroad by the grants numbers # 2021/05140-1 and # 2021/14611-8, respectively. It would be impossible, though, without the vision and brilliance of my supervisor, Dr. José Roberto de França Arruda. His professionalism is well known in the field for a long time; I would rather acknowledge him in a more personal way. I remember knocking on his door for the first time long before considering a master's degree. I was young and insecure, casually seeking something to work on, with only vague ideas of what I could accomplish. At that time, I was lost, and he welcomed me into his research group, unfolding the academic world, which until then was a complete mystery to me. For this, I will be forever in debt for his trust and guidance over the past six years, which made me ambitious and well-prepared to pursue my PhD abroad.

To the committee members, Dr. Carlos De Marqui Jr. and Dr. Alberto Luiz Serpa, thank you for helping me refine this work and smooth the rough edges. To Matheus Inguaggiato Nora Rosa, I sincerely appreciate all the help in introducing me to this challenging topic, the fruitful discussions, and the personal bits of advice. I also thank Dr. Matthew Peet for kindly receiving me in the Cybernetics Systems and Control Laboratory at ASU and for all he has been teaching me since then as a supervisor. In the last years, I had unbelievable experiences in international congresses thanks to my outstanding supervisors and the financial support from FAPESP's ENVIBRO work package, number # 2018/15894-0, a group that combines the efforts of researchers from USP, UNICAMP, UNESP, ITA, and other Brazilian and international collaborators to investigate periodic structures in the context of mechanical metamaterials, from whom I learned so much. For this, I must again praise Dr. Carlos De Marqui Jr.

When it comes to family, a quote from Roger Waters in "When We Were Young", track # 1 of "Is This the Life We Really Want?" from 2017, comes to my mind: "*Our parents made us who we are. Or was it God?*". Parents' influence on our destiny is, one way or another, inevitable; if I can call myself a scientist now, I owe it to my father, Luis Augusto, and mother, Eliana da Silva. I am grateful to have been able to share so many special moments with my family. This path is, however, undeniably challenging; sometimes, the financial hardships and the pressures from the job would have been unbearable without the support and love of my wife,

Karen Nardi, who stands by my side every day and inspires me to keep dreaming. With her, I am grateful to share the joys of life.

I also thank Sachin Shivakumar, Declan Jagt, and Alexandr Talitsky for being so kind and helpful in Arizona. Finally, The job in the Vibroacoustics Laboratory in Campinas was lightened thanks to all my colleagues: Luiz Henrique Marra da Silva Ribeiro, Vinicius Dias Lima, Nicolas Londero Gass, Caroline Beatriz Simões Valentim, Theodoro Becker Geraldi, Jean Pietro, Wanderson Monteiro, Rafael Pilotto, and Fernando Ortolano. Let the future be bright for you; this is just the beginning for us all.

## RESUMO

Metamateriais ativos têm atraído a atenção devido à sua flexibilidade e à possibilidade de ajuste; no entanto, parece haver uma lacuna significativa na literatura a respeito da estabilidade e do desempenho de metaestruturas ativas. Esses materiais podem exibir comportamento topológico, o que pode superar a sensibilidade à variabilidade de fabricação e defeitos. Nesse contexto, projetar metamateriais ativos com modos de película associados à física de sistemas não-Hermitianos é uma tarefa importante e desafiadora. Os modos de película já haviam sido observados em sistemas quânticos e foram recentemente reproduzidos na mecânica clássica, onde potenciais aplicações tecnológicas incluem controle de vibração e ruído, filtragem e multiplexação de ondas, sensores altamente sensíveis e controle de filamentos sintéticos e membranas em meios biológicos. No entanto, tais metaestruturas ativas são intrinsecamente instáveis.

Este trabalho aborda o problema da estabilidade de metamateriais ativos visando reduzir a necessidade de soluções heurísticas no projeto de metaestruturas ativas não-Hermitianas. Nesse sentido, a principal contribuição reside em usar simples arranjos unidimensionais massa-mola-amortecedor para se investigar os limites de estabilidade das metaestruturas em malha fechada e uma métrica da propagação direcional causada pelo efeito pelicular, que caracteriza o desempenho desejado.

O desempenho de qualquer modo topológico não pode, entretanto, ser analisado sem considerar a natureza topológica dos metamateriais e suas implicações na dinâmica da metaestrutura resultante. Por isso, este trabalho também fornece uma visão extensa e geral de sistemas periódicos com interações de realimentação não-recíprocas aplicadas periodicamente, abrangendo diferentes tipos de leis de realimentação, tanto locais quanto não-locais, em sistemas de parâmetros concentrados e distribuídos, amortecidos ou não. Por um lado, modelos espectrais para o movimento de ondas longitudinais são usados para mostrar as particularidades dos diagramas de dispersão dessa família de metamateriais. Por outro lado, utilizando esquemas de integração temporal baseados em uma formulação geral de espaço de estados, respostas no domínio do tempo são calculadas para analisar a dinâmica ímpar resultante e os problemas de estabilidade associados a eles.

**Palavras-chave:** metamateriais topológicos; estruturas não-recíprocas; efeito pelicular não-Hermitiano; análise de estabilidade.

## Abstract

Active metamaterials have been in the spotlight due to their flexibility and the possibility of tuning; however, there appears to be a significant gap in the literature regarding active metastructures stability and performance. These materials may exhibit topological behavior, which can overcome the sensitivity to manufacturing variability and defects. In this context, designing active metamaterials with skin modes associated with the physics of non-Hermitian systems is an important and challenging task. The skin modes had previously been observed in quantum systems and have recently been reproduced in classical mechanics, where potential technological applications include vibration and noise control, wave filtering and multiplexing, highly sensitive sensors, and control of synthetic filaments and membranes in biological media. Nevertheless, such active metastructures are intrinsically unstable.

This work addresses the problem of active metamaterial stability and is motivated to reduce the need for heuristic solutions in designing non-Hermitian active metastructures. The main contribution relies on using simple one-dimensional spring-mass-damper arrays to investigate the stability limits of the closed-loop metastructure and a metric of the directional propagation caused by the skin effect, which characterizes the desired performance.

The performance of any topological mode cannot, though, be analyzed with disregard for the topological nature of the metamaterials and its implications in the resulting metastructure dynamics. Thus, this work also provides an extensive and general view of periodic systems with periodically applied non-reciprocal feedback interactions, encompassing different kinds of feedback laws, both local and non-local, in lumped-parameter and distributed-parameter systems, damped and undamped. On the one hand, spectral models for longitudinal wave motion are used to show the particularities of the dispersion diagrams of this family of metamaterials. On the other hand, using time-integration schemes based on a general state-space framework, time-domain responses are computed to analyze the odd resultant dynamics and associated stability issues.

**Keywords:** topological metamaterials; non-reciprocal structures; non-hermitian skin effect; stability analysis.

## LIST OF FIGURES

<p>Figure 1.1 – 1D mass-spring-damper chain with feedback indicating the unit cell (dashed lines). . . . .</p>	27
<p>Figure 1.2 – Dispersion diagram of system in Fig. 1.1 for local and proportional feedback with <math>m = 1kg</math>, <math>k = 10N/m</math>, <math>\gamma_p = -1</math>, without damping. The red curve in (a) represents the dispersion in the 3D <math>\mu \times \Omega</math> space, whereas (b) is the projection of the curve in the complex plane restricted to <math>\Omega_R \geq 0</math> with the winding number <math>\nu</math> corresponding to the direction of the black arrows over the curve. Moreover, black bubbles indicate the eigenfrequencies of a finite system of 7 masses, blue bubbles indicate the eigenfrequencies of the corresponding finite passive system, and black and blue arrows highlight selected modes from the active and passive systems, respectively. . . . .</p>	28
<p>Figure 1.3 – Dispersion diagram of an acoustic distributed-parameter system presented in Chapter 2. The first four pass-bands, each one represented by a different color, in <math>\kappa \times \omega</math> space are displayed in (a), where black curves represent the projection on the green plane of constant wavenumber. This projection is shown in (b) with the arrows indicating the winding number <math>\nu</math> of each band and black bubbles representing eigenfrequencies of a corresponding metastructure. Two selected modes are associated with different winding numbers <math>\nu</math> in orange and purple. . . . .</p>	30
<p>Figure 2.1 – Comparison of the two solutions <math>\omega(\mu)</math> for a system with <math>m = 1kg</math> and <math>k = 10N/m</math>, between passive undamped system (Hermitian), passive damped system (trivially non-Hermitian), and undamped system with local proportional feedback (topologically non-Hermitian). The real part of the frequency against wavenumber is divided into (a) <math>\text{Re}(\omega) \leq 0</math>, with the sign convention of the wavenumber indicated by the arrows, and (b) <math>\text{Re}(\omega) \geq 0</math>. The imaginary part of the frequency against wavenumber is depicted in (c) corresponding to <math>\text{Re}(\omega) \leq 0</math> and (d) for <math>\text{Re}(\omega) \geq 0</math>. Finally, the projection on the complex plane is shown in (e). . . . .</p>	38

Figure 2.2 – Finite systems (metastructures) for generally non-local feedback with external excitation $w(t)$ on the $j$ -th cell. . . . .	39
Figure 2.3 – Transient response of a single band NH system with proportional local feedback ( $\gamma_p = -0.1$ and $a = 0$ ) on an undamped system ( $b = 0$ ). The tone-burst external excitation $w(t)$ is shown in (a) on both time and frequency domain (computed via the fast <i>Fourier</i> transform (FFT) algorithm); it is applied at $j = \frac{N-1}{2}$ in a structure with $N = 1499$ masses. The 2DFFT-on both space and time- of the transient response shown in waterfall plots in (c) and normalized in (d), where $\tau = t/\omega_n$ , is depicted in (b) superposed on the real part of the dispersion diagram. . . . .	41
Figure 2.4 – Dispersion and skin modes of a single band NH system with proportional non-local feedback ( $\gamma_p = -0.1$ and $a = 2$ ) on an undamped system ( $b = 0$ ). In (a), the projection of the dispersion on the complex plane is depicted, with the non-zero winding numbers of each enclosed region and black bubbles indicating eigenfrequencies of a finite system with $N = 97$ masses. The real part of the frequency against the wavenumber is shown in (b), whereas the imaginary part is depicted in (c). In (d), (e), and (f), selected normalized eigenmodes from different diagram branches are illustrated. . . . .	43
Figure 2.5 – Dispersion and skin modes of a single band NH system with derivative local feedback ( $\gamma_d = -1$ and $a = 0$ ) on an undamped system ( $b = 0$ ). In (a), the projection of the dispersion on the complex plane is depicted, with the non-zero winding numbers of each enclosed region and black bubbles indicating eigenfrequencies of a finite system with $N = 97$ masses, whereas in (b), the projection is zoomed. The real part of the frequency against the wavenumber is shown in (c), whereas (d) depicts the imaginary part. In (e) and (f), selected normalized eigenmodes are illustrated. . . . .	44

- Figure 2.6 – Transient response of a single band NH system with derivative local feedback ( $\gamma_d = -1$  and  $a = 0$ ) on an undamped system ( $b = 0$ ). The tone-burst external excitation  $w(t)$  is shown in (a) on both time and frequency domain (computed via the fast *Fourier* transform (FFT) algorithm); it is applied at  $j = \frac{N-1}{2}$  in a structure with  $N = 1499$  masses. The 2DFFT-on both space and time- of the transient response shown in waterfall plots in (c) and normalized in (d), where  $\tau = t/\omega_n$ , is depicted in (b) superposed on the real part of the dispersion diagram. . . . . 45
- Figure 2.7 – Dispersion and skin modes of a single band NH system with double derivative local feedback ( $\gamma_{dd} = 0.01$  and  $a = 0$ ) on an undamped system ( $b = 0$ ). In (a), the projection of the dispersion on the complex plane is depicted, with the non-zero winding numbers of each enclosed region and black bubbles indicating eigenfrequencies of a finite system with  $N = 97$  masses. (The real part of the frequency against the wavenumber is shown in (b), whereas (c) depicts the imaginary part. In (d), a selected normalized eigenmode is illustrated. . . . . 46
- Figure 2.8 – Transient response of a single band NH system with double derivative local feedback ( $\gamma_{dd} = 0.01$  and  $a = 0$ ) on an undamped system ( $b = 0$ ). The tone-burst external excitation  $w(t)$  is shown in (a) on both time and frequency domain (computed via the fast *Fourier* transform (FFT) algorithm); it is applied at  $j = \frac{N-1}{2}$  in a structure with  $N = 1499$  masses. The 2DFFT-on both space and time- of the transient response shown in waterfall plots in (c) and normalized in (d), where  $\tau = t/\omega_n$ , is depicted in (b) superposed on the real part of the dispersion diagram. . . . . 47
- Figure 2.9 – Dispersion and skin modes of a single band NH system with double derivative non-local feedback ( $\gamma_{dd} = 0.01$  and  $a = 1$ ) on an undamped system ( $b = 0$ ). In (a), the projection of the dispersion on the complex plane is depicted, with the non-zero winding numbers of each enclosed region and black bubbles indicating eigenfrequencies of a finite system with  $N = 97$  masses. (The real part of the frequency against the wavenumber is shown in (b), whereas (c) depicts the imaginary part. In (d) and (e) selected normalized eigenmodes are illustrated. . . . . 48

Figure 2.10–Transient response of a single band NH system with double derivative non-local feedback ( $\gamma_{dd} = 0.01$ , $a = 1$ , $k = 1N/m$ , $m = 1kg$ ) on an undamped system ( $b = 0$ ). The tone-burst external excitation $w(t)$ is shown in (a) on both time and frequency domain (computed via the fast <i>Fourier</i> transform (FFT) algorithm); it is applied at $j = \frac{N-1}{2}$ in a structure with $N = 1499$ masses. The 2DFFT-on both space and time- of the transient response shown in waterfall plots in (c) and normalized in (d), where $\tau = t/\omega_n$ , is depicted in (b) superposed on the real part of the dispersion diagram. . . . .	49
Figure 2.11–Dispersion projection on the complex plane for $l = 5$ and $a = 6$ with proportional gain (a) $\gamma_p = -0.1$ , and (b) $\gamma_p = -0.5$ . Each band is depicted with a different color. . . . .	51
Figure 2.12–Dispersion and skin modes of a dimer ( $l = 2$ ) NH system with proportional local feedback ( $\gamma_p = -1$ and $a = 0$ ) on an undamped system ( $b = 0$ ). In (a), the projection of the dispersion on the complex plane is depicted, with the non-zero winding numbers of each enclosed region and black bubbles indicating eigenfrequencies of a finite system with $N = 97$ masses. (The real part of the frequency against the wavenumber is shown in (b), whereas (c) depicts the imaginary part. In (d), (e), and (f) selected normalized eigenmodes are illustrated: modes in blue are skin modes of the NH system, the trivial modes of the Hermitian system are depicted in orange, and (f) depicts a defect edge mode corresponding to the frequency outside the closed loops of the complex plane ( $\nu = 0$ ). . . . .	55
Figure 2.13–Transient response of a dimmer ( $l = 2$ ) NH system with proportional local feedback ( $\gamma_p = 0.1$ and $a = 0$ ) on an undamped system ( $b = 0$ ). The two tone-burst external excitation $w(t)$ shown in (a) and (b) on both time and frequency domain are applied at $j = \frac{N-1}{2}$ in a structure with $N = 1499$ masses and their corresponding responses are aligned bellow them. The 2DFFT-on both space and time- of the transient responses shown in waterfall plots in (c) and (d) are depicted in (g) and (h) superposed on the real part of the dispersion diagram. Additionally, the corresponding passive system responses are depicted in (e) and (f). . . . .	56

Figure 2.14–Acoustic unit cell with local feedback. The cell has a length of $L_A + L_B$ and a uniform circular cross-section area with diameter $d$ . The measure is taken at $x_1$ , and the feedback actuation is concentrated at $x_2$ . . . . .	57
Figure 2.15–Bulk-boundary correspondence for local proportional feedback. Complex frequency plane of the system with the feedback defined in Eq. (2.61) for local ( $r = 0$ ) and proportional action ( $\gamma_D = \gamma_{DD} = 0$ ), with gain $\gamma_P = 0.015$ . Dispersion relations (solid curves) and eigenmodes of the structure (circles) are compared under (a) PBC and (b) OBC. . . . .	67
Figure 2.16–Stable duct under proportional feedback gain. (a) Bulk-boundary correspondence on the dispersion relation for the structure under OBCs. (b) FRF of both ends of the duct, the left end in red and the right end in black, for external volume velocity applied to the central DOF of the duct’s mesh. (c) Transient response to a tone-burst excitation highlighting non-reciprocal wave propagation resulting from the NHSE. . . . .	68
Figure 2.17–FRF of the non-reciprocal periodic duct with excitation at the central DOF. FRF for proportional feedback under OBC, fixed viscous damping with $\eta = 12.5$ , 18 cells, and (a) $\gamma_P = -0.0015$ (b) $\gamma_P = 0.015$ . The FRF of the passive counterpart ( $\gamma_P = 0$ ) is also included in (b). to highlight the frequency-dependent energy concentration. . . . .	68
Figure 2.18–Dispersion diagram $\omega(\kappa)$ of a non-reciprocal duct with non-local proportional feedback. First four pass-bands of the dispersion relation for non-local undamped proportional feedback with $\eta = 0$ , $\gamma_P = -0.0015$ and $a = 2$ (a) real frequency against wavenumber and (b) imaginary frequency against wavenumber. . . . .	69
Figure 2.19–Bulk-boundary correspondance of non-local proportional feedback. The dispersion diagrams were computed using $\eta = 0$ and $\gamma_P = -0.0015$ , whereas the vibration modes assume 18 cells and open-open acoustic duct. The non-locality feedback was defined by (a) $a = 1$ and (b) $a = 2$ . . . . .	69
Figure 2.20–Compared dispersion diagrams using PWE and SEM methods. The dispersions were computed using PWE (dashed red lines) and SEM (solid black lines) applied to the unit cell of Fig. 2.14 with $\eta = 0$ , $\gamma_P = 0.015$ , and $a = 0$ . . . . .	70

Figure 2.21–PZT unit cell made of local feedback. The scheme in (a) shows an amplifier  $\kappa_g$  providing a feedback gain generated as a voltage at the actuator terminals ( $L_a$ ), which is proportional to the voltage at the sensor terminals ( $L_s$ ) using the PZT effects. (b) Block diagram of the system. . . . . 77

Figure 2.22–Non-reciprocal amplification and attenuation of waves in structures with local feedback interactions ( $a = 0$ ). (a) and (c) Propagation modes of the dispersion relation for  $\kappa_g = 1.5$  and  $\kappa_g = -2$ , respectively. The First and second PBs are shown in solid red lines, superimposed to results for the equivalent passive lattice (making  $\kappa_g = 0$ ) displayed in dashed black lines. Attenuation and amplification zones are identified, respectively, by shaded magenta and green areas. (b) and (d) Transient responses to sine-burst with center frequency 300kHz illustrating the non-reciprocal wave propagation for  $\kappa_g = 1.5$  and  $\kappa_g = -2$ , respectively. Non-reciprocal wave propagation is further confirmed by their dispersion estimation through the 2D *Fourier* transform displayed as contours in (a) and (c), which are normalized by their maximum value. (e) and (f) Zoom on the imaginary dispersion diagrams to show the small and reciprocal results for damped passive lattices. . . . . 78

Figure 2.23–Dispersion topology and NH skin effect with local feedback interactions ( $a = 0$ ). (a) The complex frequency plane was obtained as a projection of the dispersion relation from the first four PBs with  $\kappa_g = 1.5$ . Shaded blue and red areas represent regions with winding numbers  $\nu = -1$  and  $\nu = 1$ , respectively. (b) The same is done for negative feedback  $\kappa_g = -2$ . Eigenfrequencies of a finite structure are displayed as black dots in (a). Selected eigenmodes were shown for (c) 1PB,(d) 2PB,(e) 3PB, and (f) 4PB. Solid purple lines are used for negative feedback, whereas orange ones are used for positive feedback. The same colors mark the selected eigenfrequencies on (a) and (b). . . . . 79

Figure 2.24–Frequency responses of the structure in terms of displacement exhibiting energy concentration and non-reciprocal behavior - local feedback interactions.(a) The scheme of the transmission simulation is depicted in (b). (b) Results of displacement spectrum estimated at the right extremity $ \hat{u}(L_c) $ with left extremity excitation (red lines) and at the left extremity $ \hat{u}(0) $ with right extremity excitation (blue lines). (c) Two-dimensional plot of the harmonic response $ \hat{u}(x) $ - in dB - with excitation at the middle of the structure ( $x = 0.2\text{m}$ ). . . . .	80
Figure 2.25–Unfolded dispersion diagrams comparing SEM and FEM using $\kappa_g = -2$ and $a = 0$ . Red lines represent the FEM approximation, and black lines the SEM results. . . . .	81
Figure 2.26–Unfolded dispersion diagrams comparing SEM and FEM using $\kappa_g = -0.7$ and $a = 1$ . Red lines represent the FEM approximation, and black lines the SEM results. . . . .	82
Figure 3.1 – Geometrical interpretation of performance measure $S$ . The Frequency Response of the considered passive structure (no feedback) is displayed in (a), whereas the green area in (b) illustrates the non-zero metric $S$ for a system with feedback; $q_1$ is the displacement on the first mass and $q_N$ on the $N$ -th mass of the chain 2.2 considering a symmetric array and excitation on the central mass. . . . .	84
Figure 3.2 – Stability margins for damped and undamped systems, with feedback or not. The maximum real part of the eigenvalues is displayed against feedback gain for undamped systems in (a), with proportional feedback for $b = 0.01$ in (b), for undamped derivative feedback in (c), and damped double derivative feedback with $b = 0.01$ in (d). . . . .	89
Figure 3.3 – Performance against proportional feedback gain depending on damping. The damping factor $b$ varies as in Table 3.1. . . . .	91
Figure 3.4 – Root locus plot for the structure with $b = 0.01$ and proportional feedback. Results are shown for $g < 0$ in (a) and $g > 0$ in (b). Magenta $x$ denotes the poles of the open loop structure, and the red line highlights the stability limit, intersecting the open left and right half-planes. . . . .	91
Figure 3.5 – Frequency response of the structure with derivative feedback and $\gamma_d = -10$ . . . . .	92

Figure 3.6 – Root locus plot for the structure with $b = 0.01$ and derivative feedback. Results are shown for $g < 0$ in (a) and $g > 0$ in (b). Magenta $x$ denotes the poles of the open loop structure, and the red line highlights the stability limit, intersecting the open left and right half-planes. . . . .	93
Figure 3.7 – Root locus plot for the structure with $b = 0.01$ and double derivative feedback. Results are shown for $g < 0$ in (a) and $g > 0$ in (b). Magenta $x$ denotes the poles of the open loop structure, and the red line highlights the stability limit, intersecting the open left and right half-planes. . . . .	93
Figure 3.8 – Stability and performance results by varying the feedback gain and damping factor. Frequency responses of stable structures ( $b = 0.01$ ) with (a) proportional feedback with $\gamma = -3$ , (b) derivative feedback with $\gamma = -1.1$ , and (c) double derivative feedback with $\gamma = 10$ . Stability margins under purely (d) proportional feedback, (e) derivative feedback, and (f) double derivative feedback, varying $\gamma$ for increasing values of $b$ . Performance under purely (g) proportional feedback, (h) derivative feedback, and (i) double derivative feedback with fixed $b = 0.01$ and varying $\gamma$ within the stability range. . . . .	95
Figure 3.9 – Stability under proportional feedback gain for different boundary conditions. In (a), (c), and (e) the root locus under proportional feedback gain varying from $\gamma_p = -10$ to $10$ is shown considering free-free, fixed-fixed, and wrap-around boundary conditions, respectively, and fixed values of $b = 0.01$ and $N = 7$ . (b), (d), and (f) show the corresponding maximum real part of the eigenvalues of the system. . . . .	96
Figure 3.10–Maximum real part of the eigenvalues of the NH system under proportional feedback by varying the number of masses. The maximum real part of the eigenvalues of the NH system is depicted for fixed parameters $\gamma_p = -0.1$ . . . . .	97
Figure 3.11–Performance of undamped ( $b = 0$ ) NH system under proportional and derivative feedback as a function of parameters $g_p$ and $g_d$ . (a) Shows the maximum real part of the eigenvalues with a black line indicating the stability limit point $\lambda_{max} = \max_j(\text{Re}(\lambda_j)) = 0$ . (b) shows the measure $S$ compared with $H_1$ , $H_2$ , and $H_\infty$ norms as defined in this Chapter, represented in (c), (d), and (e), respectively. . . . .	98

Figure 3.12–Stability margin of the acoustic NH system by varying $\gamma$ computed with a different number of finite elements. The <i>spill-over</i> effect may be inferred. . . . .	99
Figure A.1 – $(S, H)$ interconnection scheme with corresponding signals $w, z, u$ and $y$ . . . . .	117
Figure B.1 – Transient response of the state variable $\dot{x}(t, s)$ by simulating the ODE-PDE model (B.4) and (B.6) with $u(t) = 0$ for external disturbance $w(t) = \sin(5t)e^{-t}$ . . . . .	131
Figure B.2 – Transient response $r(t)$ of the ODE-PDE model (B.4) and (B.6) with $u(t) = 0$ for external disturbance $w(t) = \sin(5t)e^{-t}$ . . . . .	132
Figure B.3 – Transient response of the state variable $\dot{x}(t, s)$ on the closed-loop system for external disturbance $w(t) = \sin(5t)e^{-t}$ . . . . .	134
Figure B.4 – (a) Transient response of the output $r(t)$ and controlled input $u(t)$ of the closed-loop system for external disturbance $w(t) = \sin(5t)e^{-t}$ . (b) Transient response of the output $r(t)$ and controlled input $u(t)$ of the closed-loop system for external disturbance $w(t) = \sin(5t)e^{-t}$ . . . . .	135
Figure C.1 – Acoustic duct to be used as an experimental platform (a) with the electroacoustic components in (b). . . . .	143
Figure C.2 – Scheme of the experimental platform. . . . .	143

## LIST OF TABLES

Table 3.1 – Proportional feedback from $-10$ to $10$ with precision $10^{-4}$ . . . . .	90
Table 3.2 – Derivative feedback varying $\gamma_d$ from $-10$ to $10$ with precision $10^{-2}$ . . . . .	92
Table 3.3 – Double Derivative feedback varying $\gamma_{dd}$ from $-10$ to $10$ with precision $10^{-2}$ . . . . .	94

## LIST OF ABBREVIATIONS AND ACRONYMS

DOF	Degrees of Freedom
FBZ	First <i>Brillouin</i> Zone
FEM	Finite Elements Method
FFT	Fast <i>Fourier</i> Transform
FRF	Frequency Response Function
LMI	Linear Matriz Inequality
LPI	Linear Partial Integral Inequality
LVA-UNICAMP	Laboratório de Vibroacústica da Universidade Estadual de Campinas
NH	Non-Hermitian
NHSE	Non-Hermitian Skin Effect
OBC	Open Boundary Conditions
ODE	Ordinary Differential Equation
PBC	Periodic Boundary Conditions
PDE	Partial Differential Equation
PIE	Partial Integral Equation
PWE	Plane Wave Expansion
PZT	Lead zirconate titanate
SDP	Semi-Definite Programming
SEM	Spectral Elements Method
SSH	<i>Su-Shrieffer-Heeger</i>
TDS	Time-Delay Systems

# CONTENTS

<b>1</b>	<b>Introduction</b>	<b>23</b>
1.1	Phononic crystals and topological metamaterials	24
1.2	Non-Hermitian metamaterials	26
1.3	Notes on the analysis of distributed-parameter systems	31
1.4	Organization	33
<b>2</b>	<b>Dynamics and Topology of Non-Reciprocal NH Metamaterials</b>	<b>34</b>
2.1	The lumped-parameter system	35
2.1.1	Single-band system	35
2.1.2	Band-gaped systems with non-local feedback	45
2.2	Lumped-parameter models for distributed-parameter systems	54
2.2.1	Linear acoustic system with mass flow source	54
2.2.2	Piezoelectric material under longitudinal vibration	67
<b>3</b>	<b>Stability and Performance of Non-Reciprocal NH Metastructures</b>	<b>83</b>
3.1	A metric for the NHSE	84
3.2	Results	88
3.2.1	Proportional Feedback	89
3.2.2	Derivative Feedback	90
3.2.3	Double Derivative feedback	92
<b>4</b>	<b>Concluding Remarks and Outlooks</b>	<b>100</b>
4.1	Summary	101
4.2	Outlooks	102
4.3	List of Publications	102
	<b>References</b>	<b>104</b>
	<b>Annex</b>	<b>110</b>
	<b>ANNEX A Circuit Implementation for the Experimental Platform</b>	<b>111</b>
	<b>APPENDIX A Numerical Methods</b>	<b>113</b>
	A.1 FEM	114

A.1.1	A state-space framework for periodically applied output feedback . . .	115
A.2	SEM . . . . .	119
A.3	Plane wave expansion (PWE) . . . . .	120
<b>APPENDIX B</b>	<b>Stability Analysis and Control of Infinite-Dimensional Systems . . .</b>	<b>125</b>
B.1	ODE-PDE systems . . . . .	126
B.2	PI Operators for 1D ODE-PDE systems . . . . .	127
B.3	PIE representation of ODE-PDE systems . . . . .	128
B.4	PIETOOLS: A Toolbox for Analysis and Control of Infinite-Dimensional Systems	128
B.5	$H_2$ Norm: A Metric for Initial-Condition to Output Performance . . . . .	135
B.6	Numerical examples of the $H_2$ norm . . . . .	138
<b>APPENDIX C</b>	<b>Concept of an Experimental Realization . . . . .</b>	<b>141</b>

# 1 INTRODUCTION

*“Beauty in mathematics is seeing the truth without effort.”*

*(George Polya)*

## 1.1 Phononic crystals and topological metamaterials

Phononics is a new branch of condensed matter physics that has grown due to its potential technological applications in mechanical engineering, akin to how electronics and photonics were earlier embodied by electrical engineering. Progress in all these fields relies on controlling waves that occur in solids and fluids (Maldovan, 2013). In electronics and photonics, electromagnetic waves are associated with the phenomenology of different kinds of elementary particles: electrons, which are fermions, and photons, which are bosons, respectively. Conversely, in the case of phononics, the observed mechanical waves are the result of the collective behavior of particles that gives rise to the vibration of the crystalline lattices (VanGessel *et al.*, 2018).

The interest in periodic systems is at least as old as *Newton's* studies on sound velocity by modeling air as a simple mass-spring array. Further mathematical developments in differential equations with periodic coefficients by *Bloch* (1883) and *Floquet* (1928) allowed deeper wave analysis of non-homogeneous media with periodic spatial properties. *Brillouin's* work from the 1930's proved that the wave properties of periodic systems can be fully characterized by the analysis of subdomains of the wavenumber space  $\kappa \times \omega$  named *Brillouin zones* after him; this fact is used over this entire work and over the literature. Originally, the field was motivated by structural studies in, for example, train rail, oil and gas pipelines, aircraft and spacecraft fuselages, submarine hulls, turbines, and composite materials; however, with the introduction of photonics new paradigms, the range of possibilities in mechanical wave manipulation have grown considerably (Beli *et al.*, 2018). For a comprehensive historical overview, making justice to the landmarks in the field, the reader is referred, particularly, to the introduction of two thesis: (Beli *et al.*, 2018) and (Silva *et al.*, 2015).

The so-called phononic crystals were built to manipulate the transmission of sound and heat in analogy to previous developments in electronics and photonics (Maldovan, 2013; Hussein *et al.*, 2014). Perhaps the first and most celebrated successful result of this analogy was the possibility of producing gaps in the band structure of mechanical systems (Sigalas; Economou, 1993). The bands under analysis here lie in the wavenumber space, also called the reciprocal space, produced by the relation between frequency  $\omega$  and wavenumber  $\kappa$  of the wave solution; the wave solution  $\omega(\kappa)$  will henceforth be called dispersion relation and its graphical representation, the band structure, will be called dispersion diagram.

From the wave perspective, a mechanical band gap occurs due to surface impedance

mismatches; the phases of incident and reflected waves may differ, causing a destructive interference called *Bragg* scattering. The phase of an incident wave traveling in the medium is altered based on whether it falls within a band gap or within a pass band; if the wave frequency is inside a band gap, it means that there will be out-of-phase waves, while a pass band retains the phases, causing mostly constructive interference (Hussein *et al.*, 2006). In practice, the pattern of the displacement field in a band gap will be an exponential amplitude decay (as expressed by the non-zero imaginary part of the wavenumber), which is often called an evanescent wave and means that the wave pattern does not effectively propagate through the system. Conversely, a wave within the pass band is allowed to propagate without attenuation (except for damping effects), which becomes evident from its purely real wavenumber (in the case of undamped simple waveguides). Naturally, other phenomena typical of the quantum dynamics of electrons would be explored in phonons; here lies the principle of mechanical metamaterials: structures artificially designed to exhibit a specific wave behavior not usually found in natural materials.

As the word suggests (from Greek, *meta* means “after”/ “beyond”), metamaterials extend the possibilities of designing wave control devices beyond the hitherto used natural materials; for comprehensive works on acoustic and elastic metamaterials the reader is referred to (Fok *et al.*, 2008) and (Bertoldi *et al.*, 2017), respectively. Examples of properties achieved in the mechanical context include but are not limited to, negative *Poisson’s* ratio (Huang; Chen, 2016), negative mass, and *Young’s* modulus (Wang, 2014), and acoustic cloaking (Zigoneanu *et al.*, 2014).

Some of these metamaterials have inaugurated the field of topological mechanics, inspired by the phenomenology of electrons in the so-called topological insulators (Hasan; Kane, 2010). The robustness of the transport of electrons has attracted interest in applications for classical mechanical systems, where such properties are sought mainly for vibrations and acoustics. For this purpose, topology was used to unfold a bridge between two fundamentally different realms: the quantum world of electrons on one side and everyday macroscopic mechanical phenomena on the other. From the 1980’s on, geometrical phases and topological invariants have been used to study non-relativistic quantum dynamics (Simon, 1983), and it turns out that these notions can also be used in classical mechanics by investigating the topology of the dispersion diagrams (Huber, 2016; Ma *et al.*, 2019).

As an example in one-dimensional systems, the interface mode was extensively investigated theoretically and numerically in, for example, (Rosa *et al.*, 2017). In acoustic and

elastic systems, the pressure and vibration energy concentration at the interface may be explored for technological applications. Mathematically, it is described by the association of a geometric phase, called Zak phase, to the metamaterial dispersion diagram, whereas, phenomenologically, it is expressed by a localized mode both in space and frequency; its frequency lies inside a common band-gap of two phononic crystals with different topological characteristics and its spatial concentration occurs in the interface of two periodic arrays, each one build with one of the these crystals. The Zak phase characterizes each pass band according to symmetry properties of the band-edge modes, whereas the topological characteristic of a band gap is the accumulation of the phases of all the bands below it (Xiao *et al.*, 2015; Zhou *et al.*, 2019).

The *Su-Schrieffer-Heeger* (SSH) quantum model is an important “toy model” used to study the behavior of topological insulators, as it encompasses an important concept from topological matter: the bulk-boundary correspondence, i.e., the relation between a topological invariant from the dispersion diagram and the dynamics of a corresponding finite-structure (Batra; Sheet, 2020). It is quite interesting that the same mass-spring model used back in the seventeenth century to investigate periodic systems has been recently used in the literature as a tentative classical mechanical analog of the SSH model; naturally, this motives the introduction of lumped-parameter systems used in this work.

## 1.2 Non-Hermitian metamaterials

In this context, an intriguing topological mode called Non-Hermitian Skin Effect (NHSE) has been largely investigated in non-Hermitian (NH) metamaterials within the branch of condensed matter physics. The present work explores the phenomena resulting from the dynamics of this class of topological metamaterials and their design configurations. The research team of LVA-UNICAMP has made contributions to this topic by numerically observing and investigating topological modes in mechanical structures based on periodic non-reciprocal and NH metamaterials (Braghini *et al.*, 2021).

Consider a system that is a classical equivalence to the NH SSH models, like the *Hatano-Nelson* model (Maddi *et al.*, 2024; Bergholtz *et al.*, 2021); it distinguishes itself from simple spring-mass-damper chains by being active rather than passive. Using periodically applied feedback interactions, it is possible to design macroscale NH metamaterials analogous to the *Hatano-Nelson* model, which is endowed with exceptional topology, giving rise to the NHSE (Rosa; Ruzzene, 2020; Okuma *et al.*, 2020). An experimental acoustic platform un-

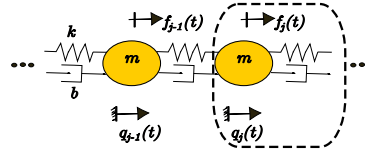


Figure 1.1 – 1D mass-spring-damper chain with feedback indicating the unit cell (dashed lines).

der development, detailed in Appendix C, will be used in the attempt to realize the NHSE and explore the plethora of possible feedback laws and their effects on both the topology of the metamaterial dispersion relation and the dynamics of the corresponding metastructure. Consider the simplest possible example: the metamaterial formed by the periodic array shown in Fig. 1.1, where the mass  $m$  is connected to other identical cells by a linear spring with constant  $k$  and the applied force  $f_j(t) = g_p(q_j(t) - q_{j-1}(t))$ ,  $\forall j \in \mathbb{Z}$  is a feedback interaction proportional to the relative displacement between the  $j$ -th cell and its immediate neighbor in the chain, the mass indexed as  $j - 1$ . This design will be further clarified in the next Chapter. This is an ordinary differential equation (ODE) system, henceforth denoted lumped-parameter system, differently from partial differential equation (PDE) systems, henceforth denoted distributed-parameter systems. Their dispersion relations can be easily obtained analytically (see next Chapter), as

$$\Omega = \pm \sqrt{4\sin^2(\mu/2) - \gamma_p(1 - e^{i\mu})}, \quad (1.1)$$

where the normalized quantities are  $\gamma_p = g_p/k$ ,  $\Omega = \frac{\omega}{\sqrt{k/m}}$ , and  $\mu = \kappa j$ .

The dispersion diagram of this kind of system is depicted in Fig. 1.2. Some general properties of this solution must be recalled. Firstly, space periodicity implies periodicity with respect to  $\mu$ . Thus, one may display the diagram on the domain  $\mu \in [-\pi, \pi)$ , which is called the first *Brillouin zone*. Furthermore, the sign of  $\mu$  corresponds to left or right propagating waves. Secondly, the nonlinearity of the dispersion relation implies dispersive wave propagation, i.e., velocity depends on frequency. Finally, for frequencies  $\Omega_R = \text{Re}(\Omega) > \sqrt{4 - 2\gamma_p}$  there is a stop band extending to infinity, which results from the lumped nature of the unit cell (Brillouin, 1946; Hussein *et al.*, 2014).

The resulting diagram consists of a single band  $\Omega(\mu) = \Omega_R + i\Omega_I \in \mathbb{C}$  computed from Eq. (1.1) by imposing  $\mu \in \mathbb{R}$  to consider only propagating modes. Two critical additional properties must be highlighted now: complex frequencies and asymmetric wave behavior. Note that the proposed feedback law is mathematically equivalent to connecting an artificial spring that breaks *Newton's* third law of action and reaction between each one of the masses, in parallel to the springs of stiffness  $k$ , from where the resulting asymmetry may be inferred.

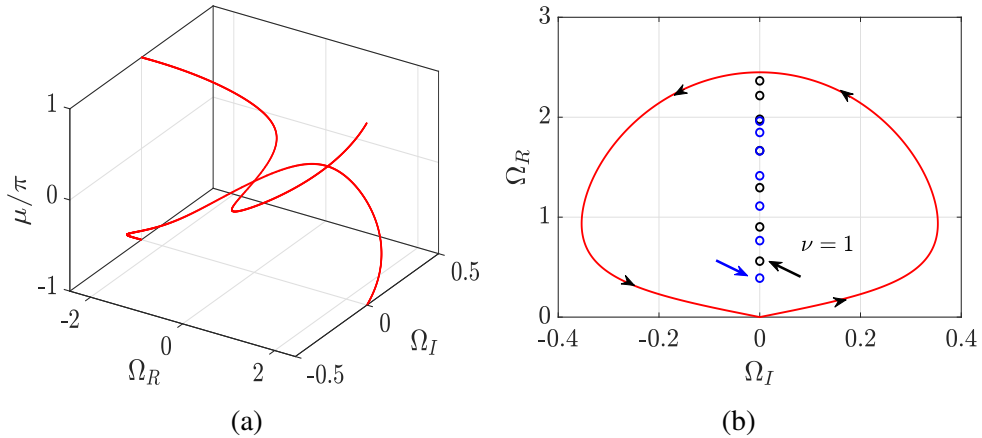


Figure 1.2 – Dispersion diagram of system in Fig. 1.1 for local and proportional feedback with  $m = 1kg$ ,  $k = 10N/m$ ,  $\gamma_p = -1$ , without damping. The red curve in (a) represents the dispersion in the 3D  $\mu \times \Omega$  space, whereas (b) is the projection of the curve in the complex plane restricted to  $\Omega_R \geq 0$  with the winding number  $\nu$  corresponding to the direction of the black arrows over the curve. Moreover, black bubbles indicate the eigenfrequencies of a finite system of 7 masses, blue bubbles indicate the eigenfrequencies of the corresponding finite passive system, and black and blue arrows highlight selected modes from the active and passive systems, respectively.

The first property arises from non-Hermiticity: by the dispersion relation, it is clear that a non-zero feedback gain  $g_p$  makes the frequency non-real, in general. This implies that, in the dispersion diagram, there will be branches corresponding to exponential amplification or attenuation of waves by a factor of  $e^{-\Omega_I}$ , depending on the sign of  $\Omega_I$ ; this corresponds to energy gain or loss provided by the source of external forces  $f_j$  and may cause stability issues of the system.

The second property is easier to observe by projecting the curve on the complex plane, as done in Fig. 1.2b (note that only  $\Omega_R \geq 0$  is displayed due to symmetry, as explained in Chapter 2). By moving on the curve within the first *Brillouin* zone, by the path indicated by the arrows, the curve makes a closed loop instead of going backward and overlaps the path from 0 to  $\pi$ ; the usually observed symmetry with respect to  $\mu$ ,  $\Omega(\mu) = \Omega(-\mu)$  is broken. Actually,  $\Omega_I(\mu) = -\Omega_I(-\mu)$ , which leads to non-reciprocity: waves propagating in one direction will be amplified, whereas waves propagating in the opposite direction will be attenuated (Rosa, 2022; Braghini *et al.*, 2021). For waves traveling in a finite waveguide in steady state, after reflections at the boundaries, the resulting vibration will be concentrated at one of the boundaries of the structure, as demonstrated in (Rosa, 2022) for lumped-parameter systems and in (Braghini *et al.*, 2021) for distributed-parameter systems.

In Fig. 1.2,  $\nu$  denotes the winding number, the topological invariant associated with the NHSE; it is 1 because the curve makes one counter-clockwise rotation around the corresponding finite-system eigenfrequencies (in black bubbles), indicating that the eigenmodes are topological modes. As shown in the next chapter, these modes are edge modes localized at one of the boundaries, depending on the sign of  $\nu$ . The broken symmetry may also be observed by the two selected eigenvectors from Fig. 1.2b, for an array of 7 cells, given in a normalized form: the skin mode pointed by the black arrow,  $V_s$  and the trivial vibration mode indicated by the blue arrow,  $V$ ,

$$V_s = \begin{bmatrix} 0.2349 \\ 0.3961 \\ 0.5942 \\ 0.8038 \\ 0.9708 \\ 1 \\ 0.7446 \end{bmatrix}, \quad V = \begin{bmatrix} 0.3827 \\ 0.7071 \\ 0.9239 \\ 1 \\ 0.9239 \\ 0.7071 \\ 0.3827 \end{bmatrix}.$$

This odd localization of energy is what defines the NHSE; its topological edge modes receive the special name of skin modes. The winding number (see Chapter 10 of (Walter, 1987)) of the eigenfrequencies with respect to the dispersion diagram are the number of times the curve closes around the eigenfrequency, and gives an efficient indirect way to tell if the corresponding skin mode is left or right localized. This relation between the winding number and the vibration modes, displayed in Fig. 1.2b, is the key to the bulk-boundary correspondence in the systems covered by this work.

Finally, when this artificially built system is extended to a distributed-parameter system, a more suitable model for technological applications, the result is an infinite countable number of bands. For example, Fig. 1.3a depicts four of these bands for one case of an acoustic system that is discussed in the next chapter, each one with a different color, along with their projection - in black solid lines - on the green complex plane;  $L_c$  is the length of the unit cell and  $f = \omega/2\pi$  is expressed in  $kHz$ . Moreover, Fig. 1.3b provides a better image of the projection, with the eigenmodes of the finite structure indicated by black bubbles and black arrows indicating the curve's path, again; the resultant winding numbers  $\nu$  for two selected modes are displayed in orange and magenta.

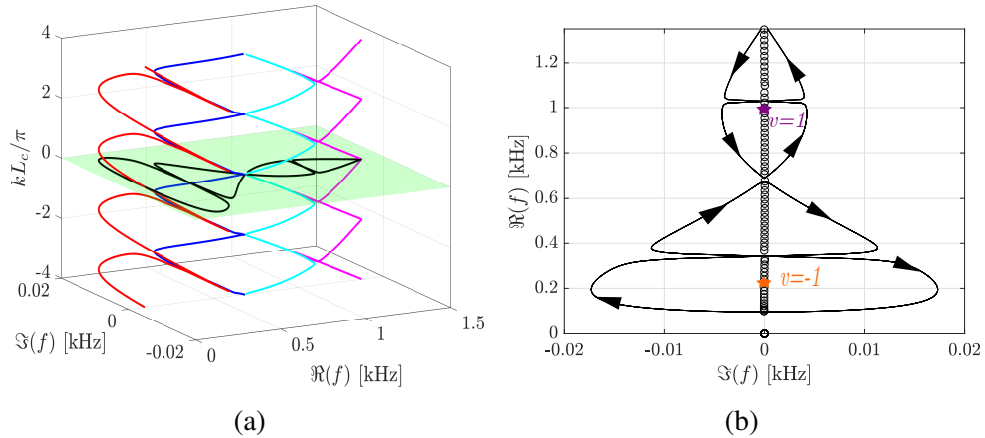


Figure 1.3 – Dispersion diagram of an acoustic distributed-parameter system presented in Chapter 2. The first four pass-bands, each one represented by a different color, in  $\kappa \times \omega$  space are displayed in (a), where black curves represent the projection on the green plane of constant wavenumber. This projection is shown in (b) with the arrows indicating the winding number  $\nu$  of each band and black bubbles representing eigenfrequencies of a corresponding metastructure. Two selected modes are associated with different winding numbers  $\nu$  in orange and purple.

Potential applications of such phenomena include but are not limited to structural control, as the structure is a classical mechanical waveguide with programmable dynamics. An example can be found in (Brandenbourger *et al.*, 2019); the authors have designed a mechatronic metamaterial that reaches non-reciprocity and unidirectional amplification of pulses, yielding new possibilities for applications where unidirectional transmission of energy is useful, e.g., communication and sensing. On the other hand, on (Budich; Bergholtz, 2020), a topologically protected sensor was proposed based on the sensitivity of NH systems to boundary conditions. Even the control of filaments and membranes in biological systems was envisioned in (Chen *et al.*, 2021). In summary, the main advantage of the proposed technology is its robustness in the face of structural imperfections and external disturbances. This robustness is attributed to topological properties of the reciprocal space; investigations on the degree of robustness of some topological behavior of periodic matter were recently performed in (Ribeiro *et al.*, 2023), though this topic still requires more investigation. Additionally, the NHSE may be used to achieve wide-range interface modes and tunable directional propagation in 2D systems, as shown in (Rosa, 2022).

Another possibility explored in the literature about NH metamaterials is the realization of topological pumping. This can be done by both time or space modulation of some parameters, such as the feedback gain of the active system. With space modulation (Pal *et al.*, 2019; Rosa *et al.*, 2019; Gupta; Ruzzene, 2020), quasi-periodic systems can introduce determin-

istic disorders in the SSH-like models. These systems are endowed with topological modes in higher dimensions and, thus, could be used, in theory, to explore higher-order NHSE in lower-dimensional physical platforms. This work won't treat quasiperiodic extensions of topological modes and pumping; for a comprehensive introduction to this topic, the reader is referred to the thesis (Rosa, 2022).

Regarding the metastructures built upon these metamaterials, the atypical bulk-boundary correspondence of NH systems and their extreme sensitivity to boundary conditions – see section III of (Bergholtz *et al.*, 2021) and section II.B.3 of (Hasan; Kane, 2010) – leads to stability problems that may naturally be explored from an engineering perspective since they influence experimental realizations and, thus, practical applications, for the NHSE cannot be applied in structural engineering if the structure cannot be stabilized. This work starts investigations in this direction, not explored so far in the literature to the best of the author's knowledge. Since the structures are already active, the idea is to apply control techniques aiming at stabilizing the system and enhancing metrics of performance related to envisioned engineering applications. The methodology used herein can be applied to pretty much any platform for the NHSE, keeping the wave behavior of the metamaterial as a beacon in every step of the design.

### 1.3 Notes on the analysis of distributed-parameter systems

Regarding distributed-parameter models, they fundamentally differ from lumped-parameter models in that they give rise to an equivalent symbolic state-space realization of infinite-dimensional states rather than the standard finite-dimensional models frequently used in engineering, e.g., finite element models. Furthermore, computation using state-space formulation is limited due to the state's dependence on continuity constraints and boundary conditions (Peet, 2021a). Nevertheless, from the point of view of the metamaterial community, the extension of the studies to continuous media is an important step (Huber, 2016).

There are mainly two well-established approaches to control systems modeled by PDEs (particular classes of infinite-dimensional systems): early and late-lumping (Morris; Levine, 2010; Das *et al.*, 2019). However, both inherently require the truncation of an infinite number of higher-order modes. As a result, these methods are either non-optimal or provide conservative stability and performance measures with no a priori bounds on accuracy (Shivakumar *et al.*, 2019; Das *et al.*, 2019; Shivakumar *et al.*, 2020; Peet, 2021a). Even though analytical solutions exist in some cases, these are limited to very special cases and do not provide general

methods.

Furthermore, the accuracy of early and late lumping methods depends heavily on the dimension of the projected state space; such methods may become numerically intractable when accurate estimates are required (Braghini; Peet, 2023), making it mandatory to apply order-reduction methods in some cases. Moreover, it is well known in structural mechanics that the truncation of the solution projected in finite-dimensional basis may cause the *spill-over* effect (see, for instance, (Zhao *et al.*, 1978), and (Eshraqi *et al.*, 2016)), which destabilizes the closed loop system and requires ad-hoc solutions like filters for the unstable modes.

Previous works on lumping-free analysis and control of distributed-parameter systems include the use of *Lyapunov* functions and the method known as backstepping. *Lyapunov* methods are based on parametrizing an energy-like function; if this function is uniformly decreasing, the resulting system is stable. Thus, the accuracy of these methods depends on the functions used and how to verify the negativity restriction on its derivative. Successful examples of finding stability certificates for a class of distributed-parameter systems can be found in (Gahlawat; Valmorbida, 2019) for linear systems and in (Valmorbida *et al.*, 2015) for non-linear PDEs. In particular, because distributed-parameter systems are defined in terms of unbounded operators, bounding the derivative of the *Lyapunov* function typically requires ad hoc steps such as integration by parts along with conservative inequalities such as the *Poincaré* inequality (Braghini; Peet, 2023).

Conversely, in backstepping, boundary control and state estimation measuring at the boundaries is obtained by transforming the system to a target form with desired properties (Krstic; Smyshlyaev, 2008). However, to date, the backstepping approach has not been used to compute input-output properties such as the  $H_2$  and  $H_\infty$  norms (Braghini; Peet, 2023; Shivakumar *et al.*, 2020).

Aiming to avoid the use of ad-hoc methods associated with typical *Lyapunov functions*, an alternative framework for representation, analysis, control, and simulation of distributed-parameter systems was recently developed (see, for example, (Peet, 2021a), (Shivakumar *et al.*, 2022), and (Jagt; Peet, 2022a)). These works use Partial Integral Equations (PIEs) and the algebraic structure of bounded linear Partial Integral (PI) operators parametrizing PIEs, an approach further explored in Appendix B. The authors envision the future integration of no-lumping control methods with the metamaterial's stability problems like the one explored in this work.

## 1.4 Organization

Firstly, in Chapter 2, models of different classes of one-dimensional systems are introduced as physical platforms to explore the NHSE: lumped-parameter systems as the simplest platforms, and their extension to distributed-parameter systems, more realistic PDE models (Braghini *et al.*, 2021; Longhi, 2021; Zhong *et al.*, 2021). Local and non-local feedback of different kinds and their influence on topological modes are explored after describing the numerical methods used.

After exploring the dynamics of the investigated systems and showing their topological characteristics, stability and performance can finally be addressed in Chapter 3, using the simplest models. A metric is defined aiming at engineering applications where non-reciprocal wave-propagation is sought; the work focuses on finding optimal solutions of non-reciprocity while restricting the design to stable metastructures. From the methods presented in Chapters 2 and 3, a general protocol to optimize the NHSE in one-dimensional systems considering different kinds of non-reciprocal periodic feedback interactions, with different numbers of unit cells in the metastructures, and damping effects are finally developed as the main contribution of this work.

All Matlab scripts used in this work are freely accessible in Github by the link [https://github.com/DanBraghini/LVA\\_NHMetamaterials](https://github.com/DanBraghini/LVA_NHMetamaterials). The reader's participation with questions or specific requests of any kind is encouraged and sincerely appreciated.

## 2 DYNAMICS AND TOPOLOGY OF NON-RECIPROCAL NH META-MATERIALS

*“I hate everything that merely instructs me without augmenting or directly invigorating my activity.”*  
*(Goethe)*

This Chapter presents numerical simulations that explore both the topology of dispersion relations and the non-reciprocal dynamics obtained by the feedback design. On the one hand, analytical and numerical spectral models for longitudinal motion are used in the systems under periodic boundary conditions (PBC). On the other hand, using time-integration schemes suited for each application and based on a general state-space framework, time-domain responses are computed and shown to confirm the predictions from the topological invariants. The Chapter is divided between the two kinds of systems characterized by the finiteness of the number of degrees of freedom in the unit cell.

## 2.1 The lumped-parameter system

The simple lumped-parameter system used in section 1.2 was artificially designed in (Rosa; Ruzzene, 2020) as a lattice to study the NHSE. In a more general approach, the unit cell may be formed by  $l \in \mathbb{N}$  different masses, and the feedback interactions  $f_j$  may connect masses distant by  $a \in \mathbb{N}$  masses; if  $a > 0$ , the feedback is called non-local. Furthermore, the feedback force may be written more generally as  $f_j(t) = \mathcal{G}(q_{j-a}(t) - q_{j-a-1}(t))$ ,  $\forall j \in \mathbb{N}$ , with  $j$  indexing the cells and the linear operator  $\mathcal{G}$  defining the feedback law. As will be shown in this section, the dispersion relation of the metamaterial proposed here is non-trivial.

### 2.1.1 Single-band system

First, consider the particular case of a single-mass cell ( $l = 1$ ) with local-feedback design ( $a = 0$ ). In this case, the dispersion may be obtained analytically. The equilibrium equation of the unit cell in Fig. 1.1, including different types of feedback actuation, can be written as

$$m\ddot{q}_j(t) = k(q_{j+1}(t) - q_j(t)) + b(\dot{q}_{j+1}(t) - \dot{q}_j(t)) - k(q_j(t) - q_{j-1}(t)) - b(\dot{q}_j(t) - \dot{q}_{j-1}(t)) + \dots \\ \dots + g_p(q_j(t) - q_{j-1}(t)) + g_d(\dot{q}_j(t) - \dot{q}_{j-1}(t)) + g_{dd}(\ddot{q}_j(t) - \ddot{q}_{j-1}(t)), \quad (2.1)$$

where the gain  $g_p$  represents pure proportional feedback, given by a multiplicative operator  $\mathcal{G}q(t) = g_p q(t)$ ;  $g_d$ , and  $g_{dd}$  represent the time derivative and double time derivative, respectively, given by the operators  $\mathcal{G}q(t) = g_d \dot{q}(t)$  and  $\mathcal{G}q(t) = g_{dd} \ddot{q}(t)$ . These feedback laws can be implemented through different kinds of commonly used measurement devices: displacement, velocity, or acceleration sensors.

The equations of motion may be rearranged as

$$(m - g_{dd})\ddot{q}_j + g_{dd}\ddot{q}_{j-1} = k(q_{j+1} - q_j) + (g_p - k)(q_j - q_{j-1}) + \dots \\ \dots + gb(\dot{q}_{j+1} - \dot{q}_j) + (g_d - b)(\dot{q}_j - \dot{q}_{j-1}),$$

where the dependence on the independent variable was omitted for the sake of simplicity. Assuming a harmonic solution  $q_j(t) = \hat{q}_j(\omega)e^{i\omega t}$ , the following equation is obtained

$$-(m - g_{dd})\omega^2\hat{q}_j - \omega^2g_{dd}\hat{q}_{j-1} = k(\hat{q}_{j+1} - \hat{q}_j) + (g_p - k)(\hat{q}_j - \hat{q}_{j-1}) + i\omega b(\hat{q}_{j+1} - \hat{q}_j) + \dots \\ \dots + gi\omega(g_d - b)(\hat{q}_j - \hat{q}_{j-1}).$$

The dispersion relation  $\Omega(\mu)$  requires assuming a periodic system where waves propagate. In this scenario, a solution of the kind  $e^{i(\Omega t - \mu n)}$  is sought, thus the *Bloch-Floquet* theorem states that  $\hat{q}_{j+1}(\omega) = e^{-i\mu}\hat{q}_j(\omega)$  and  $\hat{q}_{j-1}(\omega) = e^{i\mu}\hat{q}_j(\omega)$  yields

$$(g_{dd} - m)\omega^2 + 2k - g_p + i(2b - g_d)\omega = \\ k(e^{-i\mu} + e^{i\mu}) + ib(e^{-i\mu} + e^{i\mu})\omega - g_p e^{i\mu} - ig_d e^{i\mu}\omega + g_{dd} e^{i\mu}\omega^2,$$

which implies

$$\omega^2 = \frac{2k}{m}(1 - \cos(\mu)) - \frac{g_p}{m}(1 - e^{i\mu}) + \frac{g_{dd}}{m}(1 - e^{i\mu})\omega^2 + i\frac{2b}{m}(1 - \cos(\mu))\omega - i\frac{g_d}{m}(1 - e^{i\mu})\omega.$$

Dividing by the squared natural frequency,  $\omega_n^2 = k/m$ , and rearranging,

$$(1 - \gamma_{dd}\omega_n^2(1 - e^{i\mu}))\Omega^2 + i\left(\gamma_d\omega_n(1 - e^{i\mu}) - \frac{2b}{\sqrt{mk}}(1 - \cos(\mu))\right)\Omega + \dots \\ \dots + (\gamma_p(1 - e^{i\mu}) - 2(1 - \cos(\mu))) = 0, \quad (2.2)$$

which is a quadratic equation in the adimensional frequency  $\Omega \in \mathbb{C}$ , where the normalized gains  $\gamma_p, \gamma_d, \gamma_{dd}$  were obtained by dividing the original gains by  $k$ . Therefore, there are two solutions for each wavenumber. Considering the simplest case, without feedback and damping, yields

$$\Omega^2 - 2(1 - \cos(\mu)) = 0,$$

with solutions

$$\Omega = \pm\sqrt{2(1 - \cos(\mu))}, \quad (2.3)$$

which is always real, an implication of the system being Hermitian. On the other hand, if damping is added to the model, the equation becomes

$$\Omega^2 - i\left(\frac{2b}{\sqrt{mk}}(1 - \cos(\mu))\right)\Omega - 2(1 - \cos(\mu)) = 0,$$

implying

$$\Omega(\mu) = \frac{b}{\sqrt{mk}}(1 - \cos(\mu))i \pm \frac{1}{2} \sqrt{\frac{-4b^2(1 - \cos(\mu))^2}{mk} + 8(1 - \cos(\mu))}, \quad (2.4)$$

which is a complex solution in general. It turns out that  $\omega(\mu) = \omega(-\mu)$ , as depicted in Fig. 2.1.

However, when considering the proportional feedback case without damping, for example, Eq. (2.2) yields

$$\Omega^2 + (\gamma_p(1 - e^{i\mu}) - 2(1 - \cos(\mu))) i\omega = 0,$$

resulting in Eq. (1.1), which is generally complex for nonzero values of  $g_p$ . Actually, Fig. 2.1 shows that, although  $\Omega_R(\mu) = \Omega_R(-\mu)$ ,  $\Omega_I(\mu) = -\Omega_I(-\mu)$ , breaking the symmetry of the dispersion relation and implying that waves propagating to one direction will be exponentially attenuated in time, whereas waves propagating to the opposite direction will be exponentially amplified. Furthermore, the projection of the dispersion curves on the complex plane shows that this band makes closed loops, to which winding numbers can be attributed. This geometric feature guarantees the topological nature of the non-reciprocal wave modes, called skin modes, as shown and discussed in (Rosa; Ruzzene, 2020).

As Fig. 2.1 shows, for this kind of feedback, both solutions are symmetrical with respect to the real axis. Thus, only  $\text{Re}(\Omega) \geq 0$  may be considered. Additionally, the picture clarifies the differences in topology between a Hermitian, a trivial NH system, and a topological NH system with respect to a wave solution with wavenumber  $\mu$  and frequency  $\Omega(\mu)$ , of the form  $e^{i(\Omega t - \mu n)}$  (which gives rise to the sign convention of Fig. 2.1 (a)). The Hermitian system has a purely real frequency, indicating a purely propagating wave, whereas a damped passive system has negative imaginary frequency for some range of the wavenumbers, corresponding to exponential decay in the wave solutions with time, since  $e^{i(\Omega_R + i\Omega_I)t} = e^{-\Omega_I t} e^{i\Omega_R t}$ . Conversely, the topological NH system has non-reciprocal wave solutions indicated, in this case, by the negative imaginary frequency, which implies exponential growth with time and the closed loops encircling non-zero areas in the complex plane. This dynamical behavior is in accordance with intuitively expected results from the energy loss and gain resulting from damping effects and external control, respectively.

The NHSE is phenomenologically described by the simulation result of Fig. 2.3: topologically protected unidirectional wave propagation due to a transient excitation, as also observed in (Rosa; Ruzzene, 2020). The external force is a tone-burst signal,

$$w(t) = \sin(\omega_c t) \sin^2(\omega_2 t) H(T_2/2 - t),$$

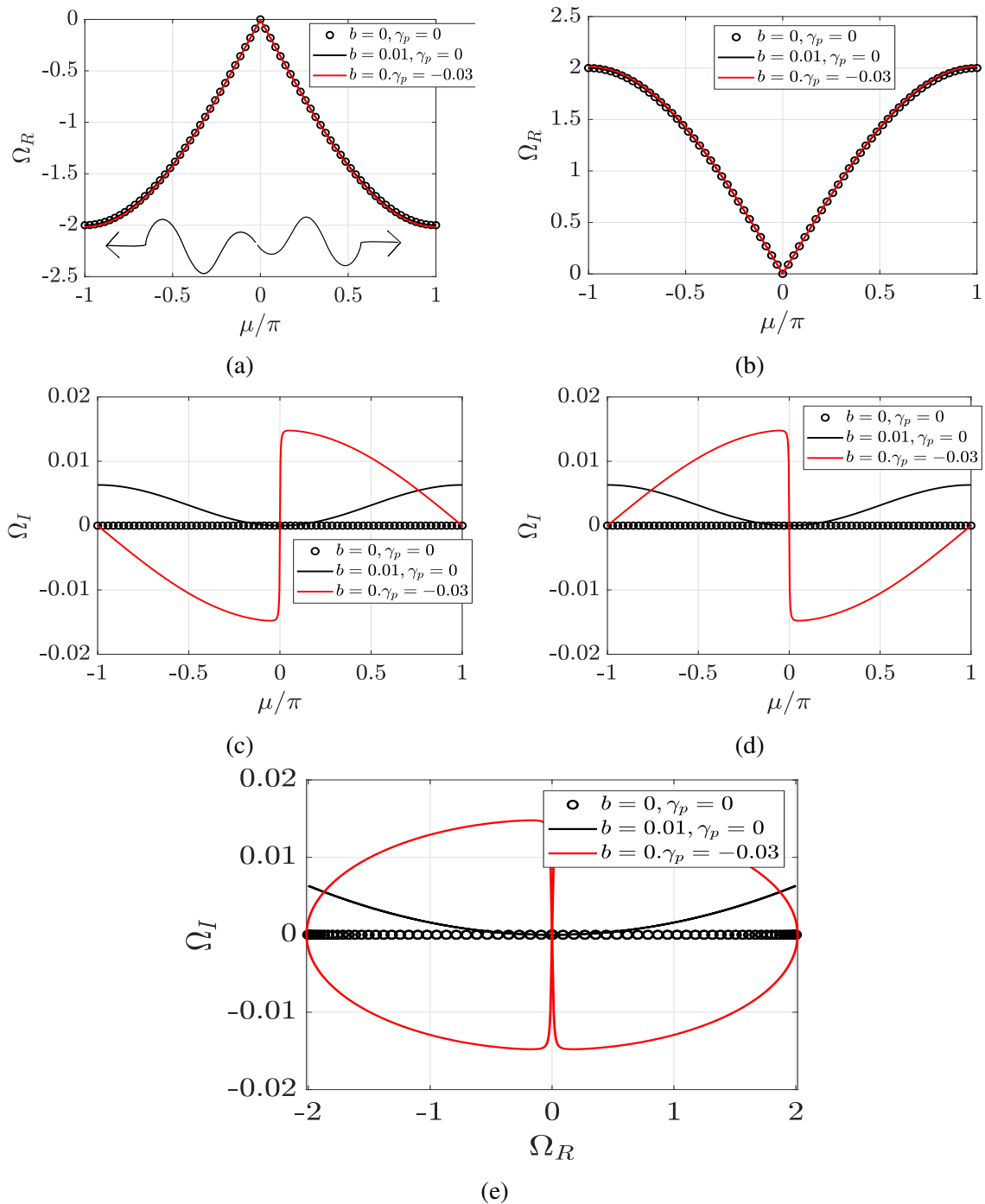


Figure 2.1 – Comparison of the two solutions  $\omega(\mu)$  for a system with  $m = 1\text{kg}$  and  $k = 10\text{N/m}$ , between passive undamped system (Hermitian), passive damped system (trivially non-Hermitian), and undamped system with local proportional feedback (topologically non-Hermitian). The real part of the frequency against wavenumber is divided into (a)  $\text{Re}(\omega) \leq 0$ , with the sign convention of the wavenumber indicated by the arrows, and (b)  $\text{Re}(\omega) \geq 0$ . The imaginary part of the frequency against wavenumber is depicted in (c) corresponding to  $\text{Re}(\omega) \leq 0$  and (d) for  $\text{Re}(\omega) \geq 0$ . Finally, the projection on the complex plane is shown in (e).

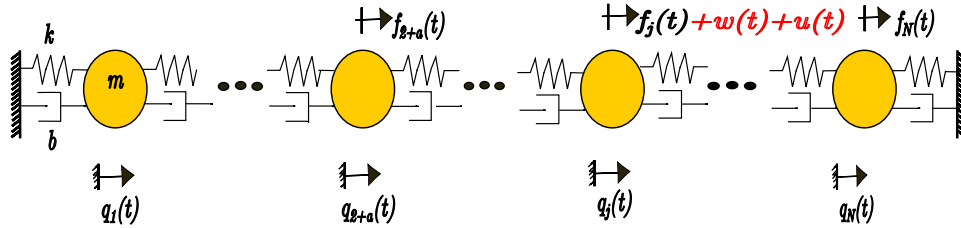


Figure 2.2 – Finite systems (metastructures) for generally non-local feedback with external excitation  $w(t)$  on the  $j$ -th cell.

where the carrier frequency  $\omega_c = 0.1581\omega_n$ , the envelope frequency  $\omega_2 = \frac{2\pi}{T_2}$ ,  $T_2 = Nc\frac{2\pi}{\omega_c}$  is chosen to envelope  $Nc$  cycles (5 in this example), and  $H$  denotes the Heaviside step function; the behavior observed in the transient responses depends on the frequencies excited by the external force. The force dynamics and spectrum transformed via *Fourier* transform is shown in 2.3a. Given the single-band dispersion from Fig. 2.1 and the wavenumber sign convention, this behavior is clearly predictable and exemplifies, once again, the close relation between topology and dynamics.

The 2D *Fourier* transform of the space-time transient response until the first reflection at the boundaries, which is shown in Fig. 2.3c and Fig. 2.3d, is overlapped with the dispersion in Fig. 2.3b and highlights the excited frequency and wavenumber, in agreement with the dispersion relation. The spatial sample frequency of 1 is chosen since it represents the inverse of the unitary distance between unit cells  $j$  and  $j + 1$ , integer numbers. Notably, the unidirectional wave propagation of the simulation response through the right direction corresponds to the positive wavenumber that is depicted in *Fourier* transform for positive real frequency  $\Omega_r$ ; negative  $\Omega_r$  has no physical mean here.

Next, the method to generate the simulation shown in Fig. 2.3 is described. For the system in Fig. 2.2, which is connected to rigid supports to remove rigid-body modes and to guarantee strictly positive-definiteness of the stiffness and damping matrices, a model in the form of Eq. (A.3), in the Appendix, is directly obtained from the equations of motion. It is easy to show that the following matrices define the damping, stiffness, and mass matrices, and the non-symmetric gain matrices of the structure.

$$\begin{aligned}
\mathbf{G}_p &= g_p D_1, & \mathbf{G}_d &= g_d D_1, & \mathbf{G}_{dd} &= g_{dd} D_1, \\
\mathbf{R} &= b D_2, & \mathbf{K} &= k D_2, & \mathbf{M} &= m \mathbf{I}_N,
\end{aligned}$$

$$D_1 = \begin{bmatrix} 0 & 0 & 0 & 0 \\ 1 & -1 & 0 & 0 \\ 0 & 1 & -1 & 0 \\ \vdots & & \ddots & \vdots \\ 0 & 0 & 1 & -1 \end{bmatrix}, \quad D_2 = \begin{bmatrix} 2 & -1 & 0 & 0 \\ -1 & 2 & -1 & 0 \\ \vdots & & \ddots & \vdots \\ 0 & 0 & -1 & 2 \end{bmatrix}.$$

By defining the state  $\mathbf{x}(t) = (\mathbf{q}(t), \dot{\mathbf{q}}(t))$ , the dynamic equation in state-space form becomes the usual state-space representation of Eq. (A.4). Next, to follow the general state-space framework presented in Appendix A, inputs and outputs must be introduced. The external disturbance and controlled input actions are defined by matrices  $\mathbf{W}$  and  $\mathbf{U}$ , respectively, given in Eq. (2.5) (assuming the disturbance on the central mass, without loss of generality, and an odd number of masses).

$$\mathbf{W} = \begin{bmatrix} \mathbf{0}_{(N-1)/2 \times 1} \\ 1 \\ \mathbf{0}_{(N-1)/2 \times 1} \end{bmatrix} \quad \mathbf{U} = \begin{bmatrix} \mathbf{0}_{1 \times N-1} \\ \mathbf{I}_{N-1} \end{bmatrix} \quad (2.5)$$

Conversely, the measured output equation depends on the feedback law. For example, if the output is relative displacement, as in the proportional feedback described in Chapter 1, the periodically applied static output feedback is  $u_i(t) = g_p(q_{i+1}(t) - q_i(t)) = g_p y_i(t)$ ,  $\forall 1 \leq i \leq N - 1$ . Thus, by defining  $D_c = g_p \mathbf{I}_{N-1}$ ,  $\mathbf{u}(t) = \mathbf{D}_c \mathbf{y}(t)$  is a particular case of Eq. (A.14), where  $y(t)$  is given by

$$\mathbf{y}(t) = \begin{bmatrix} \mathbf{Y} & \mathbf{0}_{N-1 \times N} \end{bmatrix} \mathbf{x}(t). \quad (2.6)$$

Similarly, for derivative feedback  $u_i(t) = g_d(\dot{q}_{i+1}(t) - \dot{q}_i(t))$ , the measured output is given by

$$\mathbf{y}(t) = \begin{bmatrix} \mathbf{0}_{N-1 \times N} & \mathbf{Y} \end{bmatrix} \mathbf{x}(t), \quad (2.7)$$

whereas for double-derivative feedback  $u_i(t) = g(\ddot{q}_{i+1}(t) - \ddot{q}_i(t))$ , the output is given by

$$\mathbf{y}(t) = \begin{bmatrix} -\mathbf{Y}\mathbf{M}^{-1}\mathbf{K} & -\mathbf{Y}\mathbf{M}^{-1}\mathbf{R} \end{bmatrix} \mathbf{x}(t) + \mathbf{Y}\mathbf{M}^{-1}\mathbf{F}w(t) + \mathbf{Y}\mathbf{M}^{-1}\mathbf{T}\mathbf{u}(t). \quad (2.8)$$

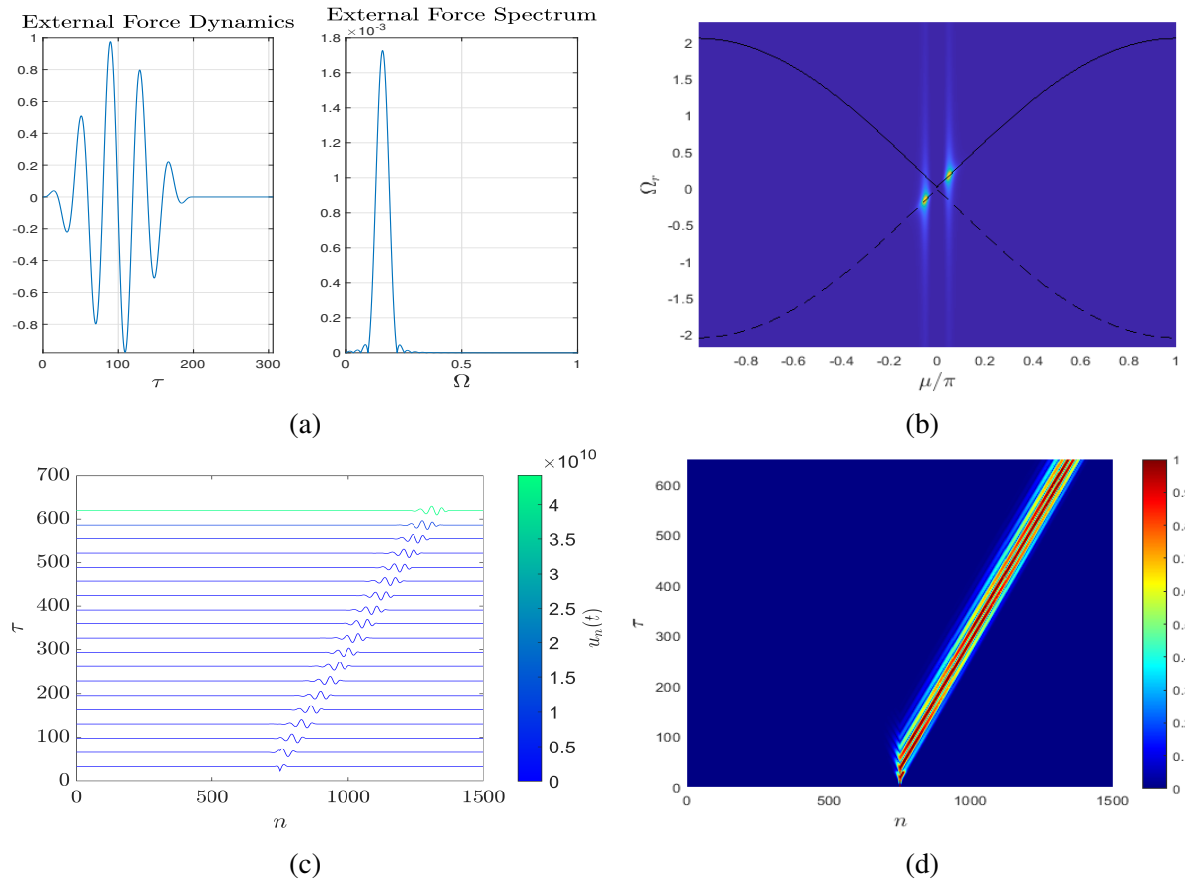


Figure 2.3 – Transient response of a single band NH system with proportional local feedback ( $\gamma_p = -0.1$  and  $a = 0$ ) on an undamped system ( $b = 0$ ). The tone-burst external excitation  $w(t)$  is shown in (a) on both time and frequency domain (computed via the fast *Fourier* transform (FFT) algorithm); it is applied at  $j = \frac{N-1}{2}$  in a structure with  $N = 1499$  masses. The 2DFFT-on both space and time- of the transient response shown in waterfall plots in (c) and normalized in (d), where  $\tau = t/\omega_n$ , is depicted in (b) superposed on the real part of the dispersion diagram.

In all the above cases, the observed output is defined by the auxiliary matrix

$$\mathbf{Y} = \begin{bmatrix} -1 & 1 & 0 & \cdots & 0 \\ 0 & -1 & 1 & 0 & \cdots \\ \vdots & \ddots & \ddots & \ddots & \ddots \end{bmatrix} \in \mathbb{R}^{N-1 \times N}. \quad (2.9)$$

Regarding non-locality, Fig. 2.4 shows, for a particular case of non-local proportional feedback, how it breaks the band into branches with different topologies; the winding numbers  $\nu$  are inferred by the auxiliary arrows that indicate the curves' path within the first *Brillouin* zone, in the same way done before in Fig. 1.2 and Fig. 1.3.

The theory states that positive winding numbers (counter-clockwise loops of the curve) are associated with right-localized skin modes. In contrast, negative values (clockwise

loops) of the topological invariant create left-localized skin modes (Rosa; Ruzzene, 2020); The computed eigenmodes on Fig. 2.4 with the model in Fig. 2.2 using  $w(t) = u(t) = 0$  and non-local feedback ( $a = 2$ ), also verify this prediction. For the eigenfrequencies within the first and third branches of the band depicted in Fig. 2.4a, with winding number  $\nu = 1$ , the eigenmodes in Fig. 2.4d and Fig. 2.4f are right-localized, whereas for the eigenfrequency in the second branch, with  $\nu = -1$ , the eigenmode in Fig. 2.4e is left-localized. Additionally, Fig. 2.4b shows the same symmetric real frequency against wavenumber observed in the local case, and Fig. 2.4c shows the asymmetric imaginary part that is divided in three branches due to non-local feedback. This split behavior as a consequence of non-locality was already observed in (Rosa; Ruzzene, 2020) and in (Braghini *et al.*, 2021) in lumped-parameter and distributed-parameter models, respectively.

Back to Eq. (2.2), by considering purely derivative feedback and no damping, one has the equation

$$\Omega^2 + i\gamma_d\omega_n(1 - e^{i\mu})\Omega - 2(1 - \cos(\mu)) = 0,$$

with solutions

$$\Omega = -\frac{\gamma_d\omega_n}{2}(1 - e^{i\mu})i \pm \frac{1}{2}\sqrt{-\gamma_d^2\omega_n^2(1 - e^{i\mu})^2 + 8(1 - \cos(\mu))}. \quad (2.10)$$

Fig. 2.5 shows that the solutions are also non-symmetric; in this case,  $\Omega_R(\mu) = -\Omega_R(-\mu)$ , even though  $\Omega_I(\mu) = \Omega_I(-\mu)$  for both solutions. Some differences from the proportional case are immediately observed. Firstly, the same solution has positive and negative  $\Omega_R$ , breaking the previous symmetry and preventing one from relying on only one of them. Furthermore,  $\Omega_I$  is non-negative, which may be explained by the similarity of this feedback case with a viscous damping element; while the proportional feedback acts like a non-reciprocal spring, the derivative feedback acts like a non-reciprocal damping element, indicating that instead of unidirectional amplification of waves, the outcome of this control will be unidirectional attenuation: waves traveling in one direction will be more attenuated than waves traveling in the opposite direction. Finally, since the resulting closed loops of both solutions on the complex plane intersect each other, there will be a region where the winding number must consider both paths; the resulting sum will be  $\nu = 0$  in this case, as shown in Fig. 2.5b.

Fig. 2.6 further corroborates with the physical damping interpretation; left propagating waves are more attenuated until the transient solution vanishes, even though no damping elements are considered ( $b = 0$ ).

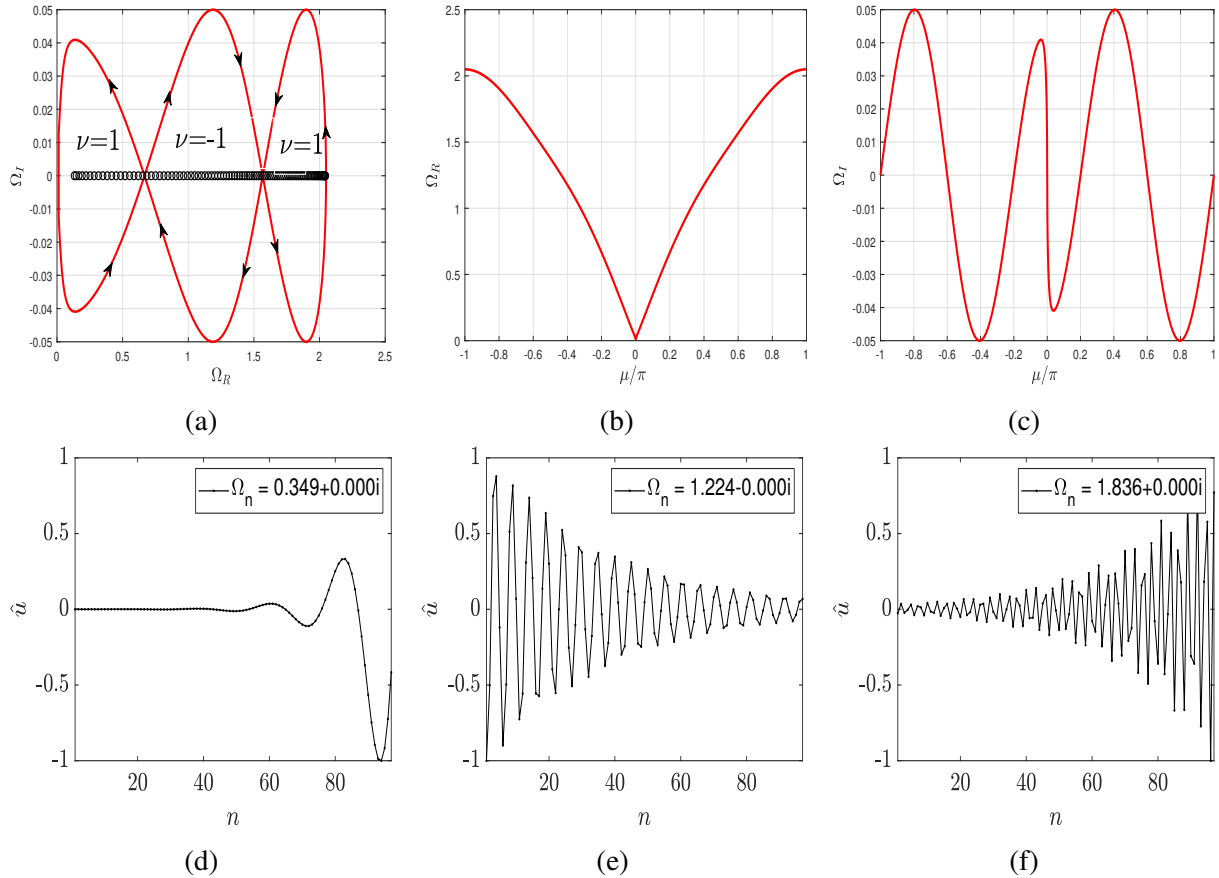


Figure 2.4 – Dispersion and skin modes of a single band NH system with proportional non-local feedback ( $\gamma_p = -0.1$  and  $a = 2$ ) on an undamped system ( $b = 0$ ). In (a), the projection of the dispersion on the complex plane is depicted, with the non-zero winding numbers of each enclosed region and black bubbles indicating eigenfrequencies of a finite system with  $N = 97$  masses. The real part of the frequency against the wavenumber is shown in (b), whereas the imaginary part is depicted in (c). In (d), (e), and (f), selected normalized eigenmodes from different diagram branches are illustrated.

The double derivative feedback remains to be considered. Again, disregarding damping effects for this first result, Eq. (2.2) becomes

$$(1 - \gamma_{dd}\omega_n^2(1 - e^{i\mu}))\Omega^2 - 2(1 - \cos(\mu)) = 0,$$

which implies

$$\Omega^2 = (1 - \gamma_{dd}\omega_n^2(1 - e^{i\mu}))^{-1} 2(1 - \cos(\mu)),$$

and finally

$$\Omega = \pm \sqrt{2(1 - \cos(\mu)) (1 - \gamma_{dd}\omega_n^2(1 - e^{i\mu}))^{-1}}. \quad (2.11)$$

The result is depicted in Fig. 2.7. The transient response in 2.8 confirms once again the interpretation of the dispersion diagram.

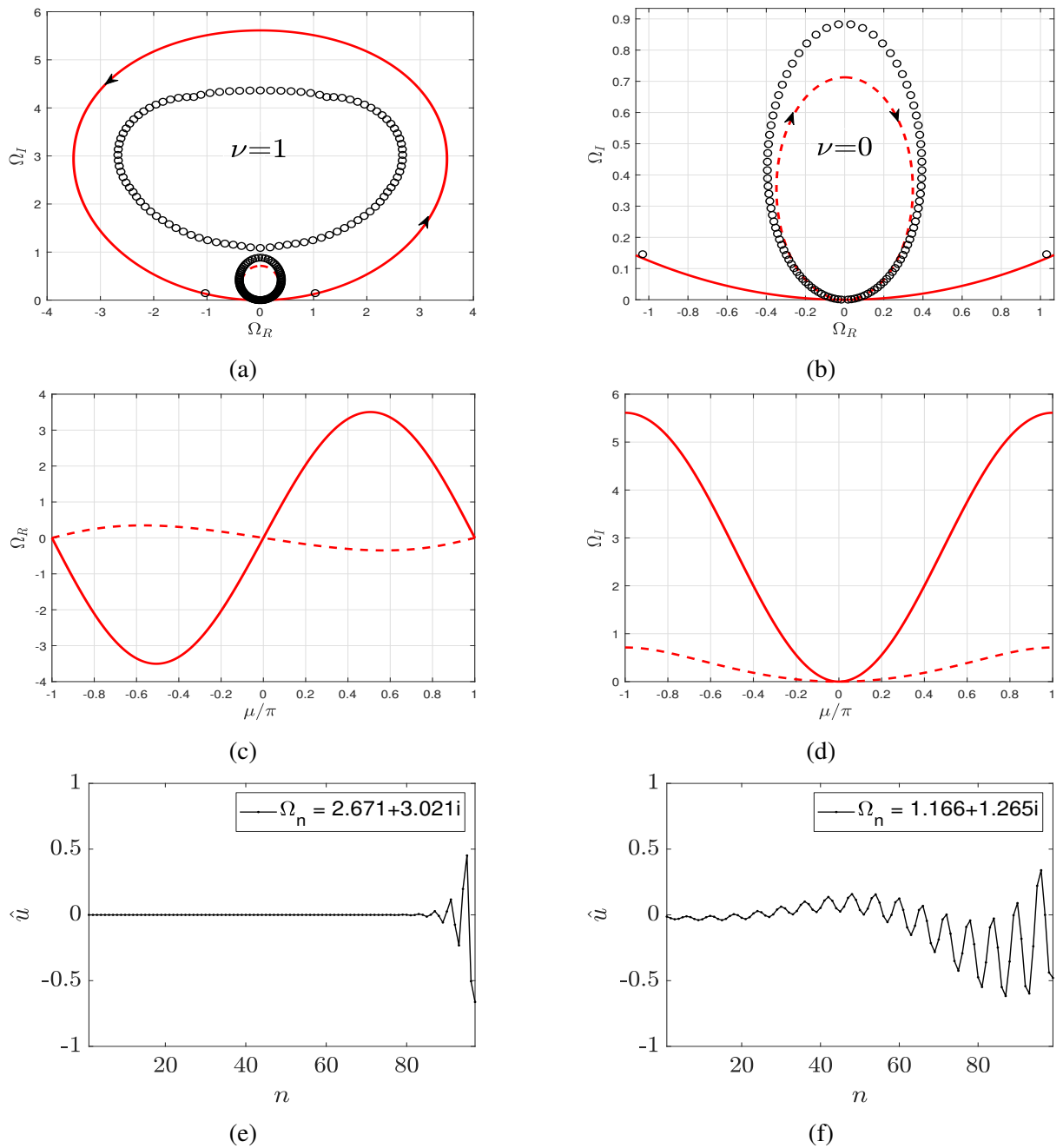


Figure 2.5 – Dispersion and skin modes of a single band NH system with derivative local feedback ( $\gamma_d = -1$  and  $a = 0$ ) on an undamped system ( $b = 0$ ). In (a), the projection of the dispersion on the complex plane is depicted, with the non-zero winding numbers of each enclosed region and black bubbles indicating eigenfrequencies of a finite system with  $N = 97$  masses, whereas in (b), the projection is zoomed. The real part of the frequency against the wavenumber is shown in (c), whereas (d) depicts the imaginary part. In (e) and (f), selected normalized eigenmodes are illustrated.

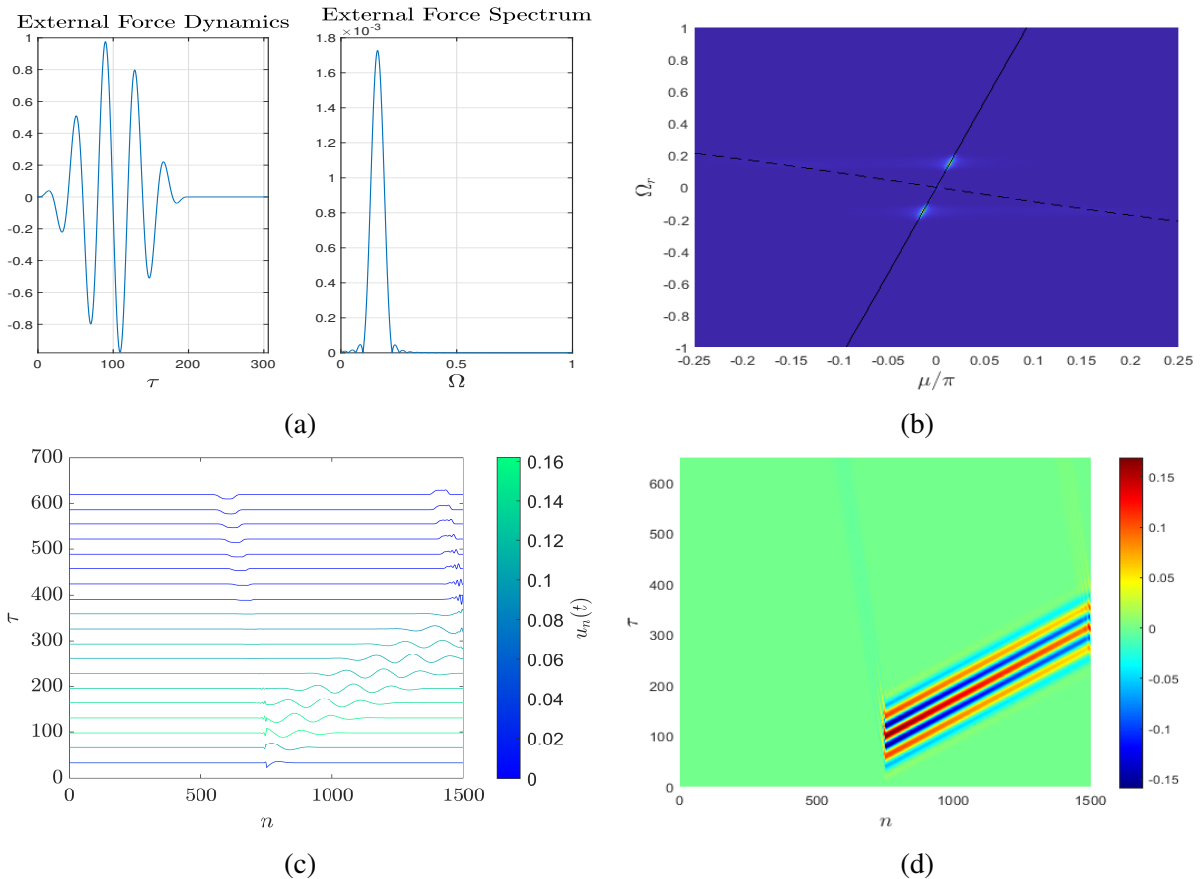


Figure 2.6 – Transient response of a single band NH system with derivative local feedback ( $\gamma_d = -1$  and  $a = 0$ ) on an undamped system ( $b = 0$ ). The tone-burst external excitation  $w(t)$  is shown in (a) on both time and frequency domain (computed via the fast *Fourier* transform (FFT) algorithm); it is applied at  $j = \frac{N-1}{2}$  in a structure with  $N = 1499$  masses. The 2DFFT-on both space and time- of the transient response shown in waterfall plots in (c) and normalized in (d), where  $\tau = t/\omega_n$ , is depicted in (b) superposed on the real part of the dispersion diagram.

The aforementioned computational approaches to dispersion and time-transient responses can easily be extended to non-local feedback, as done in the Matlab scripts freely available on the LVA Github folder, which may be used to generate the simulations on Fig. 2.9 and Fig. 2.10.

### 2.1.2 Band-gaped systems with non-local feedback

In this subsection, let's consider a much broader class of NH lumped-parameter systems with proportional feedback: unit cells composed of  $l$  masses and non-local feedback where the relative displacement measured  $a$  masses behind is applied to each mass.

The dispersion relation of this system may be obtained by a numerical inverse method (Hussein *et al.*, 2006), i.e., imposing real wavenumber and computing  $\Omega(\mu)$ . To do

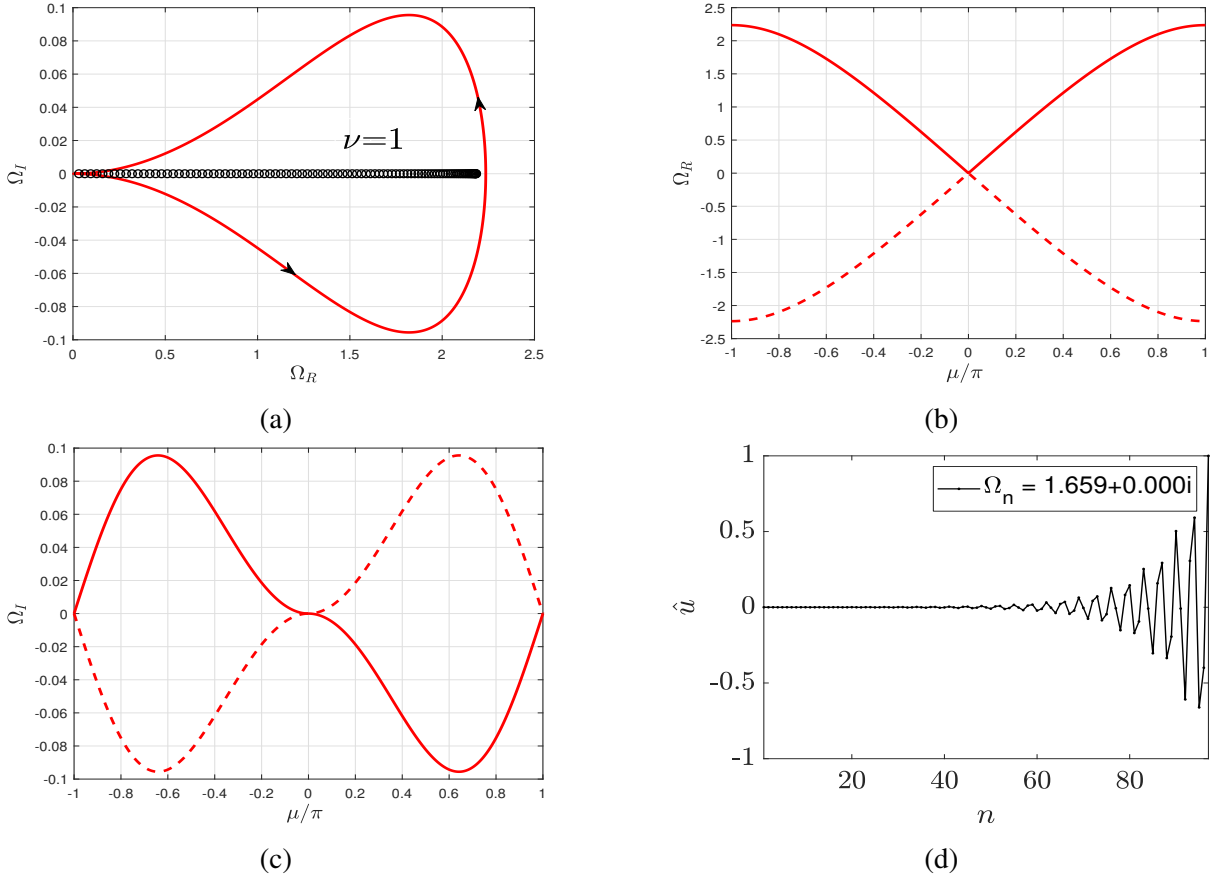


Figure 2.7 – Dispersion and skin modes of a single band NH system with double derivative local feedback ( $\gamma_{dd} = 0.01$  and  $a = 0$ ) on an undamped system ( $b = 0$ ). In (a), the projection of the dispersion on the complex plane is depicted, with the non-zero winding numbers of each enclosed region and black bubbles indicating eigenfrequencies of a finite system with  $N = 97$  masses. (The real part of the frequency against the wavenumber is shown in (b), whereas (c) depicts the imaginary part. In (d), a selected normalized eigenmode is illustrated.

so, consider the equations of motion of a unit cell with  $l$  masses.

$$\left\{ \begin{array}{l} m_1 \ddot{q}_1^j = k(q_2^j - q_1^j) + b(\dot{q}_2^j - \dot{q}_1^j) - k(q_1^j - q_l^{j-1}) - b(\dot{q}_1^j - \dot{q}_l^{j-1}) + f_1, \\ \vdots \\ m_l \ddot{q}_l^j = k(q_{m+1}^j - q_l^j) + b(\dot{q}_{m+1}^j - \dot{q}_l^j) - k(q_m^j - q_{m-1}^j) + b(\dot{q}_m^j - \dot{q}_{m-1}^j) f_n, \\ \vdots \\ m_l \ddot{q}_l^j = k(q_1^{j+1} - q_l^j) + b(\dot{q}_1^{j+1} - \dot{q}_l^j) - k(q_l^j - q_{l-1}^j) + b(\dot{q}_l^j - \dot{q}_{l-1}^j) + f_l, \end{array} \right. \quad (2.12)$$

where  $\hat{q}_m^j$  is the degree of freedom of the  $m$ -th mass of the  $j$ -th unit cell, and  $k$  refers to the spring connecting masses  $m_m$  and  $m_{m-1}$  with  $m = 1, 2, \dots, l$ . Imposing the harmonic solution

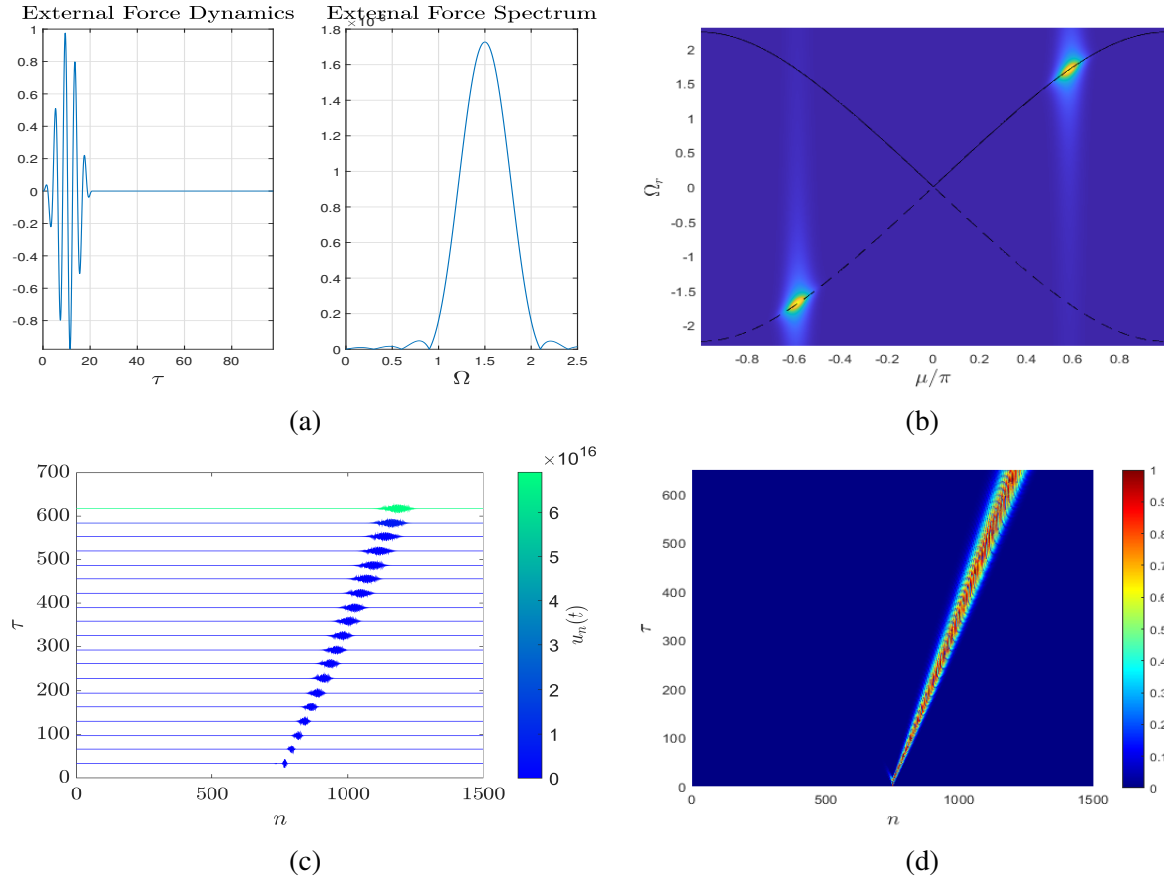


Figure 2.8 – Transient response of a single band NH system with double derivative local feedback ( $\gamma_{dd} = 0.01$  and  $a = 0$ ) on an undamped system ( $b = 0$ ). The tone-burst external excitation  $w(t)$  is shown in (a) on both time and frequency domain (computed via the fast *Fourier* transform (FFT) algorithm); it is applied at  $j = \frac{N-1}{2}$  in a structure with  $N = 1499$  masses. The 2DFFT-on both space and time-of the transient response shown in waterfall plots in (c) and normalized in (d), where  $\tau = t/\omega_n$ , is depicted in (b) superposed on the real part of the dispersion diagram.

$q_m^j(t) = \hat{q}_m^j e^{i\omega t}$  and rearranging

$$\left\{ \begin{array}{l} (2k + 2bi\omega - m_1\omega^2)\hat{q}_1^j - (k + bi\omega)(\hat{q}_2^j + \hat{q}_l^{j-1}) = \hat{f}_1, \\ \vdots \\ (2k + 2bi\omega - m_m\omega^2)\hat{q}_m^j - (k + bi\omega)(\hat{q}_{m+1}^j + \hat{q}_{m-1}^j) = \hat{f}_m, \\ \vdots \\ (2k + 2bi\omega - m_l\omega^2)\hat{q}_l^j - (k + bi\omega)(\hat{q}_1^{j+1} + \hat{q}_{l-1}^j) = \hat{f}_l. \end{array} \right. \quad (2.13)$$

Note that in Eq. (2.13), there are degrees of freedom from different cells  $\hat{q}_l^{j-1}$  and  $\hat{q}_l^{j+1}$ ; *Bloch-Floquet's* Theorem states that in periodic systems the response depends purely on the degrees of freedom of one cell. Thus, one may rewrite the equations in terms of the inner-cell displacements only (Hussein *et al.*, 2014), by the relations  $\hat{q}_l^{j-1} = \hat{q}_l^j e^{i\mu}$  and  $\hat{q}_l^{j+1} = \hat{q}_l^j e^{-i\mu}$ .

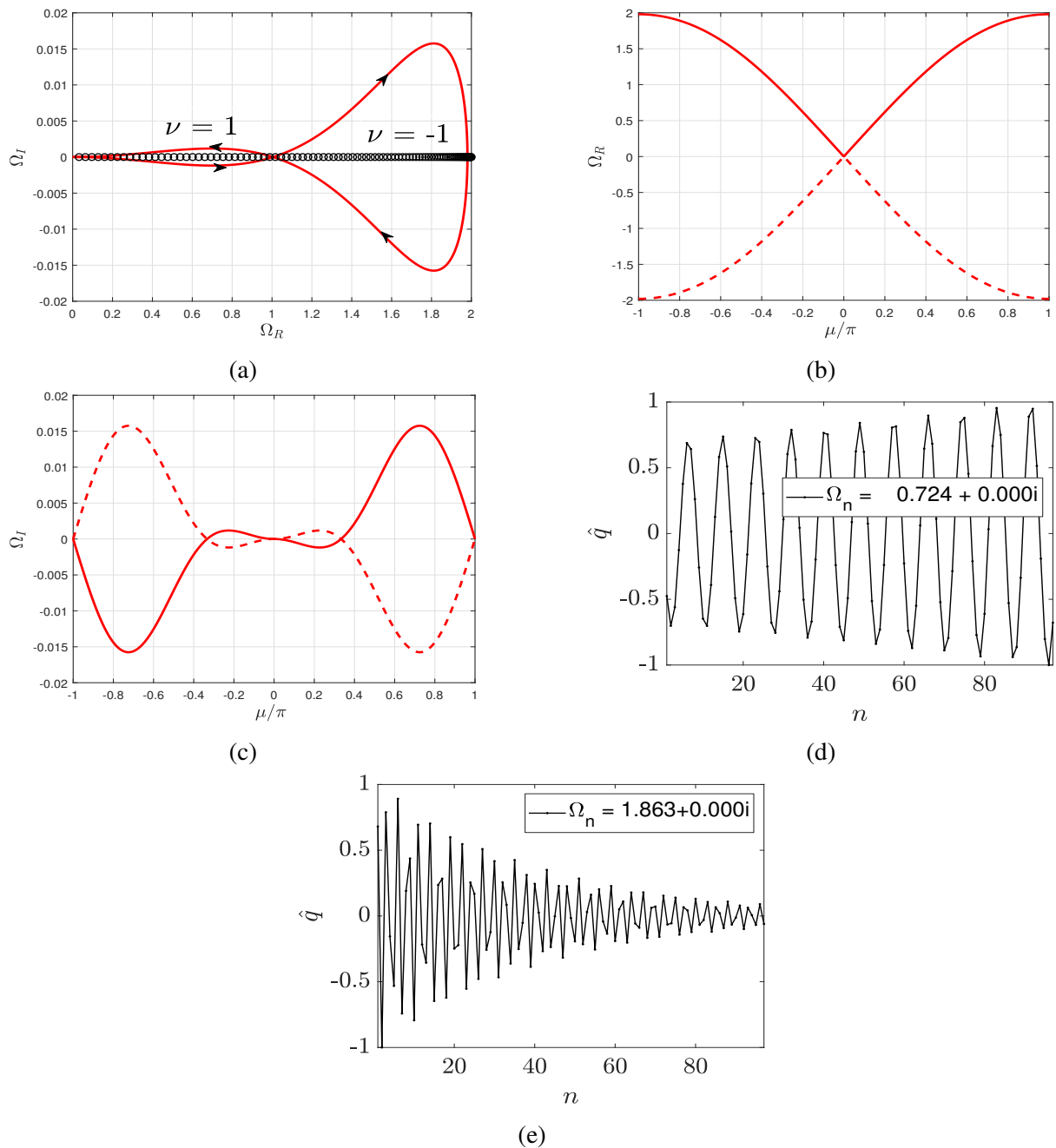


Figure 2.9 – Dispersion and skin modes of a single band NH system with double derivative non-local feedback ( $\gamma_{dd} = 0.01$  and  $a = 1$ ) on an undamped system ( $b = 0$ ). In (a), the projection of the dispersion on the complex plane is depicted, with the non-zero winding numbers of each enclosed region and black bubbles indicating eigenfrequencies of a finite system with  $N = 97$  masses. (The real part of the frequency against the wavenumber is shown in (b), whereas (c) depicts the imaginary part. In (d) and (e) selected normalized eigenmodes are illustrated.

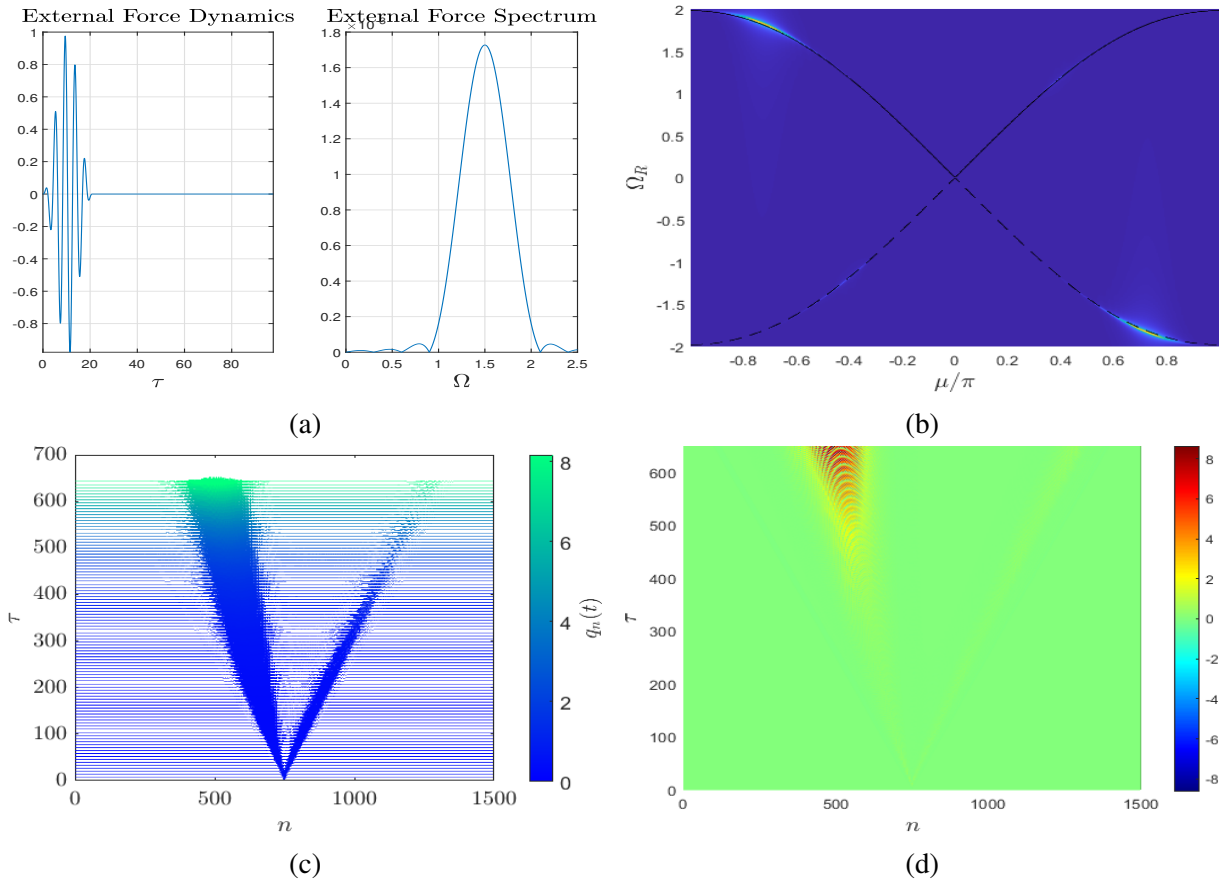


Figure 2.10 – Transient response of a single band NH system with double derivative non-local feedback ( $\gamma_{dd} = 0.01$ ,  $a = 1$ ,  $k = 1N/m$ ,  $m = 1kg$ ) on an undamped system ( $b = 0$ ). The tone-burst external excitation  $w(t)$  is shown in (a) on both time and frequency domain (computed via the fast *Fourier* transform (FFT) algorithm); it is applied at  $j = \frac{N-1}{2}$  in a structure with  $N = 1499$  masses. The 2DFFT-on both space and time- of the transient response shown in waterfall plots in (c) and normalized in (d), where  $\tau = t/\omega_n$ , is depicted in (b) superposed on the real part of the dispersion diagram.

Also, considering the generally non-local feedback interactions, three cases are possible: if  $a = 0$ ,

$$\left\{ \begin{array}{l} \hat{f}_1 = g_p(\hat{q}_1^j - \hat{q}_l^{j-1}), \\ \vdots \\ \hat{f}_m = g_p(\hat{q}_m^j - \hat{q}_{m-1}^j), \\ \vdots \\ \hat{f}_l = g_p(\hat{q}_l^j - \hat{q}_{l-1}^j), \end{array} \right. \quad (2.14)$$

, if  $0 < a < l$ ,

$$\left\{ \begin{array}{l} \hat{f}_1 = g_p(\hat{q}_{l-a+1}^{j-1} - \hat{q}_{l-a}^{j-1}), \\ \hat{f}_2 = g_p(\hat{q}_{l-a+2}^{j-1} - \hat{q}_{l-a+1}^{j-1}), \\ \vdots \\ \hat{f}_{a+1} = g_p(\hat{q}_1^j - \hat{q}_l^{j-1}), \\ \hat{f}_{a+2} = g_p(\hat{q}_2^j - \hat{q}_1^j), \\ \vdots \\ \hat{f}_l = g_p(\hat{q}_{l-a}^j - \hat{q}_{l-a-1}^j), \end{array} \right. \quad (2.15)$$

, or if  $l \leq a$ ,

$$\left\{ \begin{array}{l} \hat{f}_1 = g_p(\hat{q}_{l-a+1}^{j-1} - \hat{q}_{l-a}^{j-1}), \\ \hat{f}_2 = g_p(\hat{q}_{l-a+2}^{j-1} - \hat{q}_{l-a+1}^{j-1}), \\ \vdots \\ \hat{f}_{a+1} = g_p(\hat{q}_1^j - \hat{q}_l^{j+1}), \\ \hat{f}_{a+2} = g_p(\hat{q}_2^j - \hat{q}_1^j), \\ \vdots \\ \hat{f}_l = g_p(\hat{q}_{l-a}^j - \hat{q}_{l-a-1}^j). \end{array} \right. \quad (2.16)$$

The resultant matrix equation is

$$[-\omega^2 \mathbf{M}_j + \mathbf{K}(\mu)_j + i\omega \mathbf{R}(\mu)_j] \hat{\mathbf{q}}^j = \mathbf{G}_j(\mu)_j \hat{\mathbf{u}}^j, \quad (2.17)$$

where  $\mathbf{M}_j, \mathbf{K}(\mu)_j, \mathbf{R}(\mu)_j \in \mathbb{C}^{2 \times 2}$  are the mass, stiffness, and damping matrices, while  $\mathbf{G}_j(\mu)_j \in \mathbb{C}^{l \times l}$  is the feedback gain matrix of the  $j$ -th cell. Generally,  $\mathbf{K}(\mu)_j$  and  $\mathbf{G}(\mu)_j$  depend on the wave number and the  $j$ -th unit cell, which can be seen as a subsystem. Furthermore, the vector  $\hat{\mathbf{q}}^j$  whose matrix representation is  $\left[ \hat{q}_1(\omega) \ \dots \ \hat{q}_l(\omega) \right]_j^T$  contains the degrees of freedom of the unit cell. It needs to differ from zero for non-trivial solutions.

An algorithm can be written to calculate the matrices and solve the problem, resulting in solutions  $\Omega(\mu) = \omega(\mu)/\omega_n$ , whose graphical representation constitutes the dispersion diagram. It is sufficient to calculate the values of  $\omega$  for  $-l\pi \leq \mu \leq l\pi$ , constituting the first  $l$  Brillouin zones.

The reader may find a general script named ‘‘ProportionalLumped\_Dispersion’’ on the LVA Github folder, freely available through the link provided in Chapter 1, to compute the

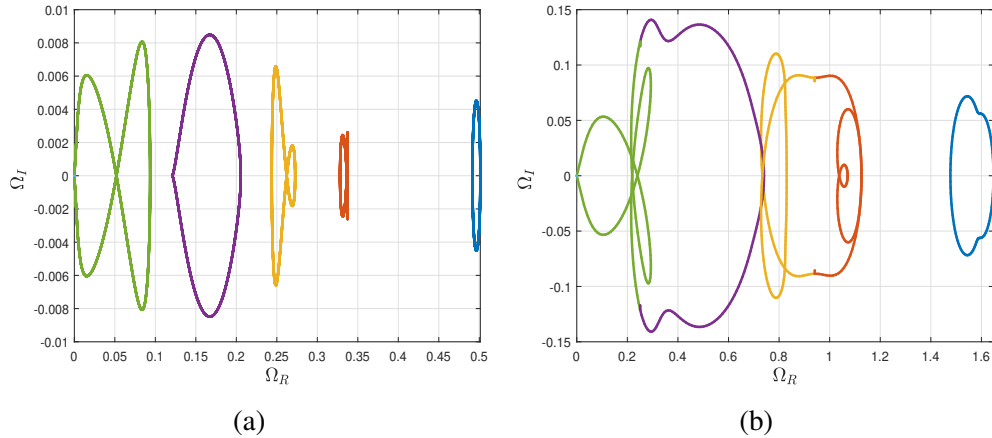


Figure 2.11 – Dispersion projection on the complex plane for  $l = 5$  and  $a = 6$  with proportional gain (a)  $\gamma_p = -0.1$ , and (b)  $\gamma_p = -0.5$ . Each band is depicted with a different color.

dispersion for system in Eq. (2.12), under the subfolder named “LumpedSys”. As an example, Fig. 2.11 shows the projection on the complex plane of the diagram for  $l = 5$  and  $a = 6$ . In this case, there are at most five different bands, forming closed loops with differently complicated topologies; as the control gain increases, from (a) to (b), only one band gap remains open, as the lower frequency bands merge.

Consider, particularly, the case of a dimer-type uni cell with  $l = 2$  and  $a = b = 0$ , simplifying the system to

$$\begin{cases} (2k - m_1\omega^2)\hat{u}_1^j - k\hat{u}_2^j - k\hat{u}_2^{j-1} = F_{a1}, \\ (2k - m_2\omega^2)\hat{u}_2^j - k\hat{u}_1^j - k\hat{u}_1^{j+1} = F_{a2}, \end{cases}$$

which, in matrix form is represented by the matrices

$$\mathbf{M}_j = \begin{bmatrix} m_1 & 0 \\ 0 & m_2 \end{bmatrix}, \quad (2.18)$$

$$\mathbf{K}(\mu)_j = \mathbf{K}(\mu)_j^* = \begin{bmatrix} 2k & -k(1 + e^{i\mu}) \\ -k(1 + e^{-i\mu}) & 2k \end{bmatrix}, \quad (2.19)$$

$$\mathbf{G}(\mu)_j = \begin{bmatrix} -k_c & k_c e^{i\mu} \\ k_c & -k_c \end{bmatrix}, \quad (2.20)$$

The matrix in Eq. (2.19) is Hermitian as  $\mathbf{K}(\mu)_j = \mathbf{K}(\mu)_j^H$ ; however, the feedback gain matrix for the system, in Eq. (2.20), is not Hermitian. The eigenvalue problem

$$\mathbf{A}(\mu)_j \hat{\mathbf{u}}^j = \omega^2 \hat{\mathbf{q}}^j, \quad (2.21)$$

becomes evident where  $\mathbf{A}(\mu)_j = \mathbf{M}_j^{-1}[\mathbf{K}(\mu)_j + \mathbf{G}_p(\mu)_j]$ ; in the case of non-Hermitian systems, the frequencies  $\omega$  solution of the problem are generally complex, which is associated with an attenuation or amplification factor of the dynamic response of the system, as explained before.

In the example case, these solutions are the roots of the two eigenvalues for each value of  $\mu$ . Imposing positive values for  $\text{Re}(\omega)$  yields two unique and well-defined solutions corresponding to frequencies in the first and second pass bands. Since the matrices are generally  $\in \mathbb{C}^{l \times l}$  for a system with  $l$  masses in the unit cell, the result will be  $l$  eigenvalues corresponding to at most  $l$  different passbands. It can be foreshadowed, therefore, that the dispersion diagrams of distributed-parameter systems, which have infinite degrees of freedom in the unit cell, have infinite pass-bands; since a countable infinite number of bands does not fit in a bounded domain, it is also expected that the frequency range will be extended to infinite and then, the semi-infinite stop band of lumped-parameter systems will disappear. In fact, the next subsections illustrate this case.

The dispersion relation computed this way corresponds to a metamaterial or periodic system, whereas practical interest usually lies in analyzing real structures composed of a finite number of unit cells of this material. It was shown in (Hussein *et al.*, 2006) that the condition for guaranteed equivalence between the results obtained from the analysis of infinite periodic systems and their respective finite structures, in the Hermitian case, is to use at least three unit cells. The solution to the eigenvalue problem of Eq. (2.21) is the free-vibration response; its eigenvalues correspond to the natural vibration frequencies, and its eigenvectors to the respective modes of vibration. The natural frequency  $\omega = 0$  can only be included in the free-free boundary conditions since it corresponds to a non-vibratory solution and is a natural frequency of the unit cell itself (Faulkner; Hong, 1985).

Considering the forced-response problem of  $M$  unit cells, each with  $l$  masses, by making the association  $q_m^j = q_n$ , with  $1 \leq n \leq Ml = N$ , the system of Eq. (A.3) is again easily derived and excited by an input  $\hat{\mathbf{f}}(\omega) = [\hat{f}_1(\omega) \ \hat{f}_2(\omega) \ \cdots \ \hat{f}_N(\omega)] \in \mathbb{C}^N$ , the forced response problem is represented by

$$\mathbf{D}(\omega) \hat{\mathbf{u}}(\omega) = \hat{\mathbf{F}}(\omega),$$

where  $\mathbf{D}(\omega) = \mathbf{K}_j(\mu) + \mathbf{G}_j(\mu) + i\omega\mathbf{R}_j(\mu) - \omega^2\mathbf{M} \in \mathbb{R}^{NxN}$  is the dynamic stiffness matrix. From the perspective of dynamical systems, the same problem can be seen as

$$\hat{\mathbf{u}}(\omega) = \mathbf{H}(\omega)\hat{\mathbf{F}}(\omega),$$

with  $\mathbf{H}(\omega) = \mathbf{D}(\omega)^{-1}$  being the transfer matrix in the frequency domain. If the system is Hermitian,  $\mathbf{D}(\omega)$  and  $\mathbf{H}(\omega)$  are symmetric matrices.

Calling  $\mathbf{H}(\omega)_{i,j}$  the element of row  $i$  and column  $j$  of  $\mathbf{H}(\omega)$ , this element represents the influence of the  $j$ th component of  $\hat{\mathbf{F}}(\omega)$  on the  $i$ th component of  $\hat{\mathbf{q}}(\omega)$ . If the matrix is symmetric,  $\mathbf{H}(\omega)_{i,j} = \mathbf{H}(\omega)_{j,i}$  and the system can be called reciprocal, which means that the response to an excitation at one point  $j$  measured at another point  $i$  is equal to the response measured at  $j$  to an excitation at point  $i$ . However, for the systems built in this Chapter,  $\mathbf{H}(\omega)$  is not symmetric, and the system is characterized as non-reciprocal.

As shown in Fig. 2.12, there are two passbands separated by a band gap; the first band is drawn in red, while the second one is in blue. On the band gap, the wavenumber assumes a purely imaginary part, which is associated with (spatial) attenuation modes called evanescent waves and is not usually computed in  $\Omega(\mu)$  methods. The dashed black lines highlight the passbands for a passive system, i.e., with  $g_p = g_d = g_{dd} = 0$ . As expected, the imaginary part of  $\Omega$  is zero for the passive system. Comparing the real part of the dispersion diagram, the passbands of the passive system show a slight deviation from the active system bands, and this deviation is greater near the edges of the *Brillouin* zones. For the second passband, in higher frequencies, this deviation is more pronounced and present throughout the *Brillouin* zones. Furthermore, the results are shown for a free-free array of masses, rather than fixed at both ends, to show that different choices of OBC do not change the topology, as noted in the Appendix of (Rosa, 2022).

One important aspect of these results is that the second passband's topology must be analyzed in the second *Brillouin* zone: due to the periodic nature of the dispersion relation, numerical methods tend to compute each band for the entire range of wavenumber and, if one "folds" the dispersion to the FBZ, as usually done for *Hermitian* metamaterials and phononic crystals, one will incur in wrong results. A discussion on the differences between the so-called folded and unfolded versions of the dispersion diagram can be found in the Appendix of (Braghini et al., 2021).

The winding number could also be calculated analytically and interpreted by the eigenmodes associated with the natural frequencies of the structure, besides simple geometric

visualization (Gong *et al.*, 2018; Braghini *et al.*, 2021). Similarly, as done with the previous results, Fig. 2.12 also shows the natural frequencies of a finite structure, in this case with ten unit cells, in black dots on the complex plane. There is a localized normal mode outside the circles and, therefore, considered trivial regarding the topological surface mode ( $\nu = 0$ ), showed to be localized on the left in (f) for both the active structure in blue and the passive structure in orange; if this was a skin mode, it would not appear in the passive structure. One can call this mode a defect mode of the structure, which appears due to the breaking of symmetry in the dimer's unit cell (Hussein *et al.*, 2015).

Fig. 2.13 shows, as done before, that the unidirectional wave propagation can be predicted by the dispersion relation by exciting the finite system's two passbands. Additionally, the figure compares the active with the passive (topologically trivial) systems, to emphasize the topological nature of the observed non-reciprocity. The 2D *Fourier* transform of the transient response in Fig. 2.3 (b) is made, again, by taking the response until the first reflection in the boundaries and agreeing with the dispersion relation. A spatial sample frequency of  $1/2$  must be chosen in this case, since the distance between each mass is half the unitary distance between the unit cells. The result in (h) confirms the previously explained necessity to display the unfolded dispersion diagrams, for  $l$  Brillouin zones, rather than just the FBZ.

## 2.2 Lumped-parameter models for distributed-parameter systems

In this section, PDE models for the proposed metamaterials are derived based on first-principle physical modeling. Then, the resultant forced linear wave equations corresponding to distributed-parameter systems are discretized to provide the results of this section, similar to the results of the last section. The PDEs governing these systems, under PBCs and applying spectral discretization methods, produce dispersion relations with infinitely many pass bands, an intuitive result bearing in mind the results of the last section 2.1.2. On the other hand, by applying OBCs on a bounded domain and discretizing the space with a FEM approach, the resultant lumped-parameter model is shown to have non-reciprocal responses similar to the results in the previous section.

### 2.2.1 Linear acoustic system with mass flow source

In this section, consider the distributed-parameter unit cell of Fig. 2.14, which is a cylindrical geometry of cross-sectional diameter  $d$ , divided into three segments to account for a

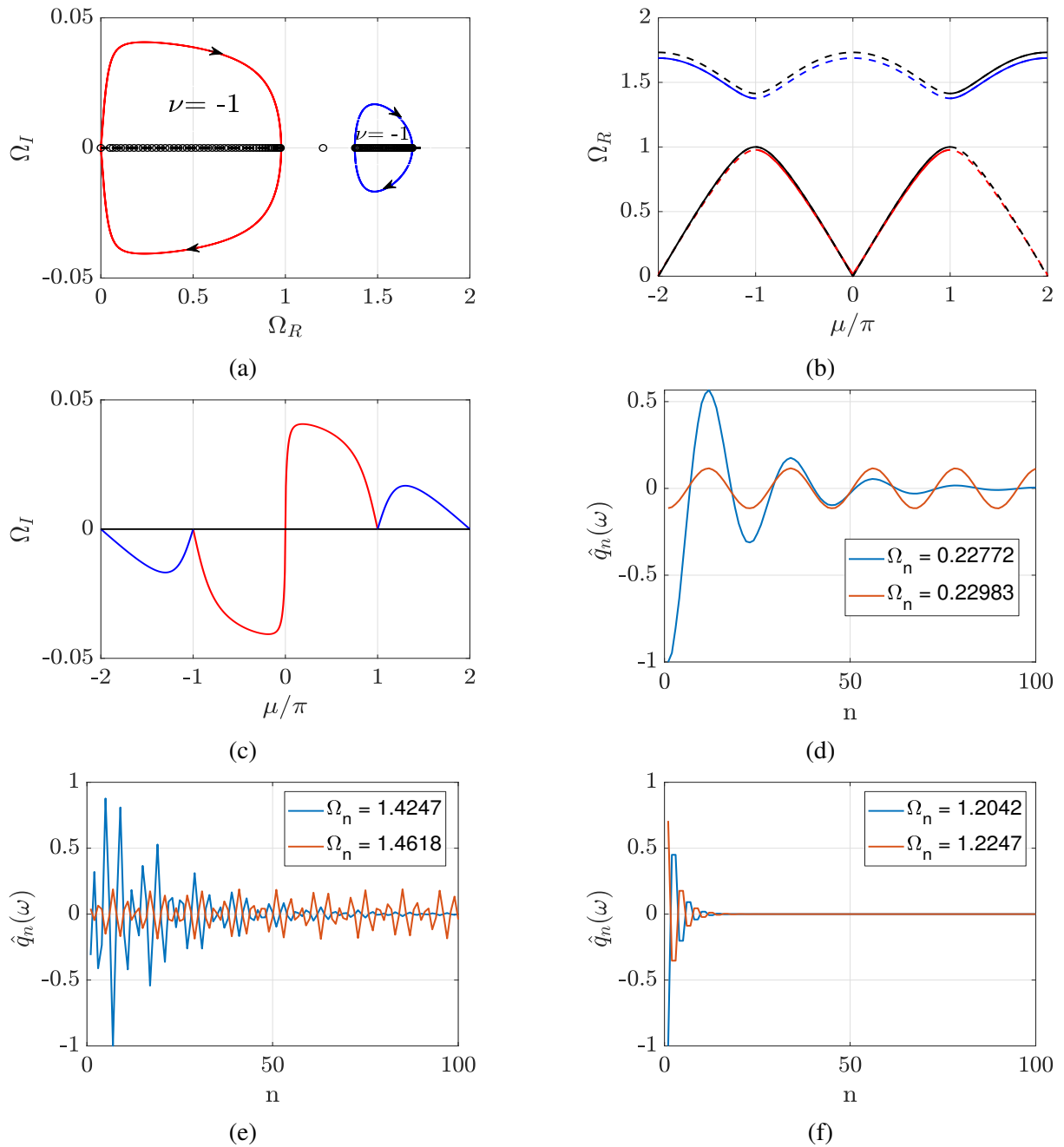


Figure 2.12 – Dispersion and skin modes of a dimer ( $l = 2$ ) NH system with proportional local feedback ( $\gamma_p = -1$  and  $a = 0$ ) on an undamped system ( $b = 0$ ). In (a), the projection of the dispersion on the complex plane is depicted, with the non-zero winding numbers of each enclosed region and black bubbles indicating eigenfrequencies of a finite system with  $N = 97$  masses. (The real part of the frequency against the wavenumber is shown in (b), whereas (c) depicts the imaginary part. In (d), (e), and (f) selected normalized eigenmodes are illustrated: modes in blue are skin modes of the NH system, the trivial modes of the Hermitian system are depicted in orange, and (f) depicts a defect edge mode corresponding to the frequency outside the closed loops of the complex plane ( $\nu = 0$ ).

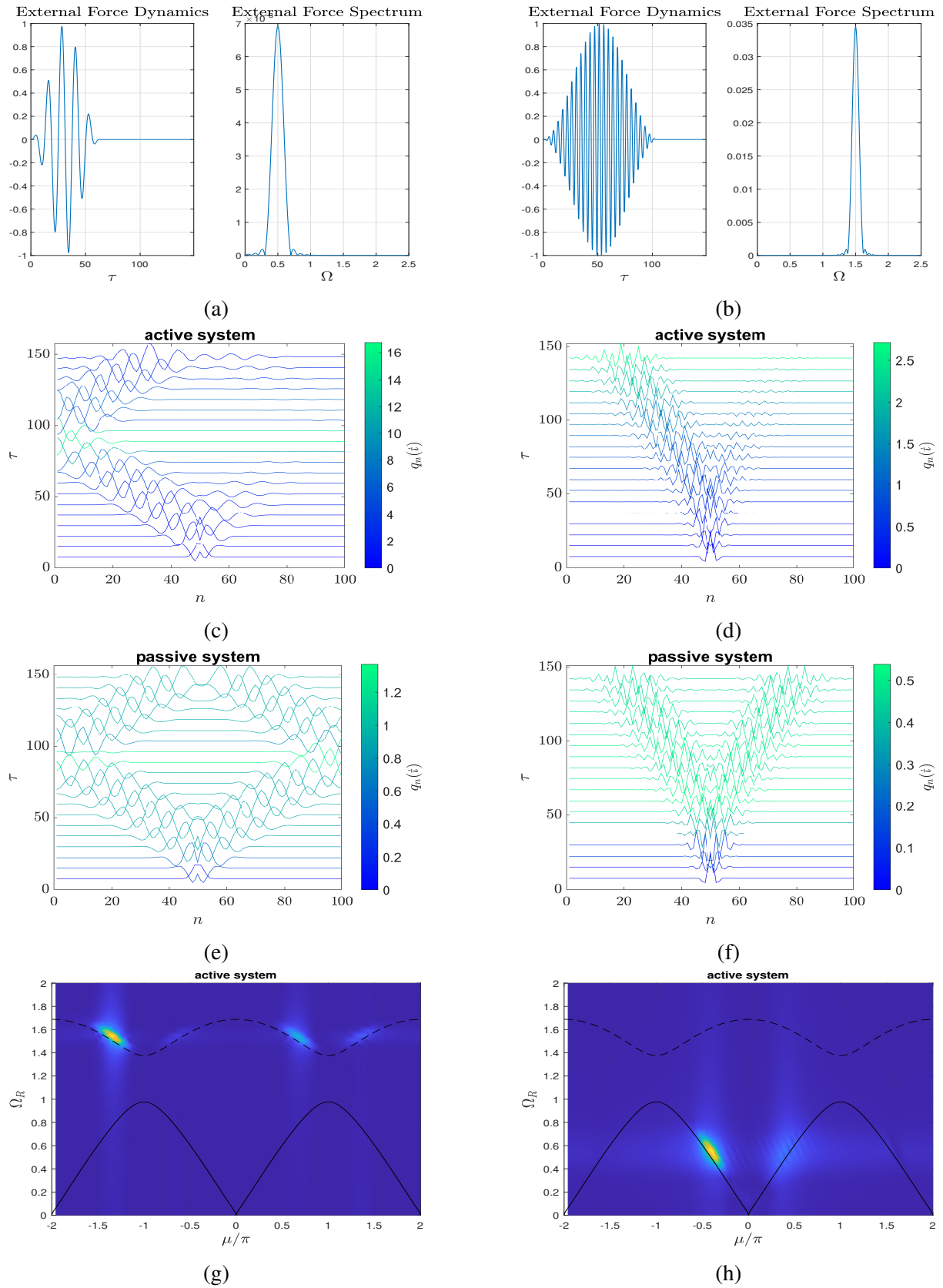


Figure 2.13 – Transient response of a dimmer ( $l = 2$ ) NH system with proportional local feedback ( $\gamma_p = 0.1$  and  $a = 0$ ) on an undamped system ( $b = 0$ ). The two tone-burst external excitation  $w(t)$  shown in (a) and (b) on both time and frequency domain are applied at  $j = \frac{N-1}{2}$  in a structure with  $N = 1499$  masses and their corresponding responses are aligned below them. The 2DFFT-on both space and time- of the transient responses shown in waterfall plots in (c) and (d) are depicted in (g) and (h) superposed on the real part of the dispersion diagram. Additionally, the corresponding passive system responses are depicted in (e) and (f).

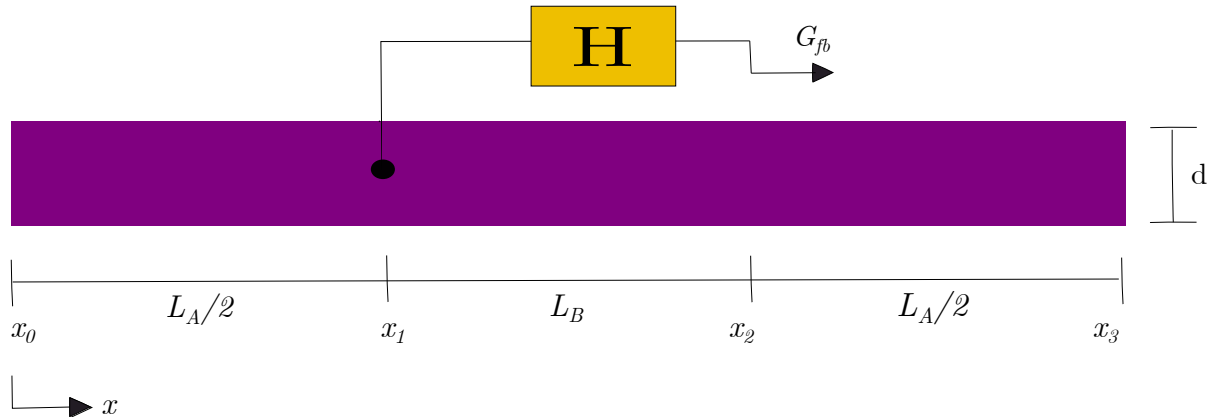


Figure 2.14 – Acoustic unit cell with local feedback. The cell has a length of  $L_A + L_B$  and a uniform circular cross-section area with diameter  $d$ . The measure is taken at  $x_1$ , and the feedback actuation is concentrated at  $x_2$ .

measure point,  $x_1$ , and an application point,  $x_2$ , where point sensors and actuator close a local feedback loop. For non-local feedback, the measured signal is taken in  $x_1$   $a$  cells behind.

The acoustic wave traveling through a quiescent fluid can be assumed as an adiabatic process; the air is modeled as a perfect and inviscid gas, and only small disturbances propagate. Moreover, for frequencies lesser than  $0.586 \frac{c}{d}$ , where  $c$  is the sound velocity in the air, only plane waves may be considered (Kinsler *et al.*, 2000).

Next, a forced linear wave equation is derived as in (Braghini *et al.*, 2022), which models the dynamics of the active acoustic metamaterial. This equation is used to derive the numerical models of the following sections.

The acoustic wave traveling through a quiescent fluid can be assumed as an adiabatic process. The state equation of a perfect gas in such conditions can be stated as follows (Moran *et al.*, 2010):

$$P(\mathbf{x}, t) = P_0 \left( \frac{\rho(\mathbf{x}, t)}{\rho_0} \right)^{C_p}, \quad (2.22)$$

where the scalar fields  $P, \rho : D \subset \mathbb{R}^3 \times [0, T] \rightarrow \mathbb{R}$  representing general time-varying pressure and mass density,  $P_0, \rho_0 \in \mathbb{R}$  the pressure and density of the fluid in its mean state and  $C_p \in \mathbb{R}_{>0}$  being the heat capacity ratio. The dependency on space and time variables may be omitted in the equations henceforth for the sake of clarity. With the assumption of small acoustic disturbances, one can expand Eq. (2.22) in the *Taylor* series and neglect the derivatives of second order and higher. Thus, recalling also that any thermodynamic variable can be written as a function of two other independent thermodynamic variables, one gets the expression for the pressure as an

affine function of density for densities close enough to  $\rho_0$

$$P(\rho, \eta) = P_0 + \left. \frac{\partial P(\rho, \eta)}{\partial \rho} \right|_{\rho=\rho_0} (\rho - \rho_0). \quad (2.23)$$

Defining the Bulk modulus  $B$  as

$$B(\rho, \eta) = \rho_0 \left( \frac{\partial P}{\partial \rho} \right)_\eta, \quad (2.24)$$

where  $(\cdot)_\eta$  indicates that entropy  $\eta$  remains constant while taking the partial derivative. Omitting also the dependency on thermodynamic variables, define pressure and density disturbances  $p$  and  $\rho'$ , respectively as

$$p = P - P_0, \quad (2.25)$$

$$\rho' = \rho - \rho_0. \quad (2.26)$$

Now, assuming the additional hypothesis of inviscid fluid flow, one can conclude that the entropy transport equation is

$$\frac{D\eta}{Dt} = 0, \quad (2.27)$$

meaning that the material time derivative (Gurtin, 1982) of entropy equals zero on the system. Thus, the only variable is  $\rho$ ,  $B(\rho, \eta) = B(\rho)$ , and Eq. (2.23) can be rewritten as the following linear relation between acoustic variables

$$p = \frac{B(\rho_0)}{\rho_0} \rho'. \quad (2.28)$$

For continuity, consider an infinitesimal volume  $dV = dxdydz$ . The volume is fixed in space, and the fluid flows through it. The rate of mass flowing along each direction with velocity field  $\mathbf{u} : D \subset \mathbb{R}^3 \times [0, T] \rightarrow \mathbb{R}^3$  such that  $\mathbf{u}(\mathbf{x}, t) = (u_x(\mathbf{x}, t), u_y(\mathbf{x}, t), u_z(\mathbf{x}, t))$  is given by three scalar equations:

$$\rho u_x dydz - \left( \rho u_x dydz + \frac{\partial(\rho u_x)}{\partial x} dxdydz \right) = -\frac{\partial(\rho u_x)}{\partial x} dV, \quad (2.29)$$

$$\rho u_y dydz - \left( \rho u_y dydz + \frac{\partial(\rho u_y)}{\partial y} dxdydz \right) = -\frac{\partial(\rho u_y)}{\partial y} dV, \quad (2.30)$$

$$\rho u_z dydz - \left( \rho u_z dydz + \frac{\partial(\rho u_z)}{\partial z} dxdydz \right) = -\frac{\partial(\rho u_z)}{\partial z} dV. \quad (2.31)$$

Combining these equations, the flux of mass through the boundaries of the volume is

$$F = - \left( \frac{\partial(\rho u_x)}{\partial x} + \frac{\partial(\rho u_y)}{\partial y} + \frac{\partial(\rho u_z)}{\partial z} \right) = -\text{div}(\rho \mathbf{u}). \quad (2.32)$$

Considering a source injecting mass with a rate per unit of volume  $Q : D \subset \mathbb{R}^3 \times [0, T] \rightarrow \mathbb{R}$ , the principle of balance of mass results in the transport equation of mass:

$$\frac{\partial \rho}{\partial t} = Q - \operatorname{div}(\rho \mathbf{u}), \quad (2.33)$$

which can be rewritten using the identity  $\operatorname{div}(\rho \mathbf{u}) = \nabla \rho \cdot \mathbf{u} + \rho \operatorname{div}(\mathbf{u})$  and expanding the variables in terms of the acoustic disturbances as

$$\frac{\partial(\rho_0 + \rho')}{\partial t} = Q - \nabla(\rho_0 + \rho') \cdot (\mathbf{u}_0 + \mathbf{u}') + (\rho_0 + \rho') \operatorname{div}(\mathbf{u}_0 + \mathbf{u}'), \quad (2.34)$$

having in mind that, since the fluid movement is a consequence of pressure disturbances,  $\mathbf{u}$  can also be written as  $\mathbf{u}(\mathbf{x}, t) = \mathbf{u}_0 + \mathbf{u}'(\mathbf{x}, t)$ .  $\mathbf{u}_0 = 0$ , since the fluid is quiescent, and using again the hypothesis of small disturbances one gets

$$\frac{\partial \rho'}{\partial t} + \rho_0 \operatorname{div}(\mathbf{u}') = Q, \quad (2.35)$$

which can be rewritten, with the relation between pressure and density given by Eq. (2.28), as

$$\frac{\rho_0}{B(\rho_0)} \frac{\partial p}{\partial t} + \rho_0 \operatorname{div}(\mathbf{u}) = Q. \quad (2.36)$$

The difference of force caused by the pressure on each opposite side of the element in each direction is given by three scalar equations:

$$P dydz - \left( P + \frac{\partial P}{\partial x} dx \right) dydz = -\frac{\partial P}{\partial x} dV, \quad (2.37)$$

$$P dx dz - \left( P + \frac{\partial P}{\partial y} dy \right) dx dz = -\frac{\partial P}{\partial y} dV, \quad (2.38)$$

$$P dx dy - \left( P + \frac{\partial P}{\partial z} dz \right) dx dy = -\frac{\partial P}{\partial z} dV. \quad (2.39)$$

Combining these equations results in

$$d\mathbf{f} = -\nabla P, \quad (2.40)$$

where  $\mathbf{f}$  is the force per unit of volume. The resultant force acting on the element  $dV$  with mass  $dm = \rho dV$  is

$$d\mathbf{f} dV = \mathbf{a} dm = \mathbf{a} \rho dV = \rho \left( \frac{\partial \mathbf{u}}{\partial t} + (\nabla \mathbf{u}) \bullet \mathbf{u} \right) dV. \quad (2.41)$$

From Eqs.( 2.40) and (2.41), it follows that:

$$-\nabla p = \rho \left( \frac{\partial \mathbf{u}}{\partial t} + (\nabla \mathbf{u}) \bullet \mathbf{u} \right). \quad (2.42)$$

Finally, expanding all the acoustic variables as small acoustic disturbances in a quiescent fluid, one gets the linearized *Euler* equation:

$$-\nabla p = \rho_0 \frac{\partial \mathbf{u}}{\partial t}. \quad (2.43)$$

The time derivative of Eq. (2.36), multiplied by  $A$  is

$$\frac{\rho_0 A}{B(\rho_0)} \frac{\partial^2 p}{\partial t^2} + \operatorname{div} \left( A \rho_0 \frac{\partial \mathbf{u}}{\partial t} \right) = A \frac{\partial Q}{\partial t}. \quad (2.44)$$

Applying the divergent operator to Eq. (2.43) multiplied by  $A$  one gets the following equation

$$-\operatorname{div}(A \nabla p) = \operatorname{div} \left( A \rho_0 \frac{\partial \mathbf{u}}{\partial t} \right). \quad (2.45)$$

Substituting the result in Eq. (2.44), one finally derive the linear wave equation with a source of mass as follows:

$$A \frac{1}{c^2} \frac{\partial^2 p}{\partial t^2} - \operatorname{div}(A \nabla p) = A \frac{\partial Q}{\partial t}, \quad (2.46)$$

where  $c = \sqrt{B(\rho_0)/\rho_0}$  is the speed of sound in the fluid. In particular, for 1-D systems,

$$\frac{\partial}{\partial x} \left( A \frac{\partial p}{\partial x} \right) - \frac{A}{c^2} \frac{\partial^2 p}{\partial t^2} = -A \frac{\partial Q}{\partial t}. \quad (2.47)$$

Multiplying the previous equation by  $c^2$  and taking the concentrated source of mass of (Fig. 2.14),  $Q(x, t) = \bar{Q}(t, \delta(x - x_2))$  yields

$$\frac{\partial^2 p}{\partial t^2} = c^2 \frac{\partial^2 p}{\partial x^2} + \frac{4B}{\pi d^2} \frac{dG}{dt} \delta(x - x_2) \quad | \quad x \in \Omega = (x_0, x_3), \quad (2.48)$$

in the unit cell, which is expanded to the whole structure of  $n_c$  cells as:

$$\frac{\partial^2 p}{\partial t^2} = c^2 \frac{\partial^2 p}{\partial x^2} + \frac{4B}{\pi d^2} \sum_{n=1}^{n_c} \frac{dG_n}{dt} \delta(x - x_n) \quad : \quad x \in \Omega = (0, n_c x_3), \quad (2.49)$$

with  $x_n = x_2 + (n-1)L_c$ , the *Dirac* delta  $\delta$  indicating that it is concentrated in  $x_n$ . The speed of sound is approximatedly constant for the small disturbances considered here  $c = \sqrt{B(\rho_0)/\rho_0}$  and  $\bar{Q} = \frac{\rho_0 G}{A(x_2)}$  is the relation between the excitation model used in PWE,  $\bar{Q}(t)$  (see on the Appendix Eq. (A.3)) and volume velocity  $G(t)$ , used in the other numerical methods. The solutions  $p : \bar{\Omega} \times [0, T] \rightarrow \mathbb{R}$  depend on the appropriate boundary and initial conditions.

Both SEM and PWE methods may be used to compute the dispersion relation of such systems. The SEM matrix  $\mathbf{K}_j$  of Eq. (A.19) (see Appendix A) for a homogeneous one-dimensional linear acoustic duct is given by Eq.(2.50) for each frequency (Rosa *et al.*, 2017).

$L_j$  represents the length of the element and  $\kappa(\omega) = \frac{\omega}{c}$  the local wavenumber related to the constant phase velocity  $c$  of acoustic waves traveling through a homogenous duct or the  $j$ -th homogeneous segment of the unit cell

$$\mathbf{K}_j(\omega) = \frac{A}{\rho c i (1 - e^{-2ik(\omega)})} \begin{bmatrix} e^{-2i\kappa(\omega)L_j} + 1 & -2e^{-i\kappa(\omega)L_j} \\ -2e^{-i\kappa(\omega)L_j} & e^{-2i\kappa(\omega)L_j} + 1 \end{bmatrix}. \quad (2.50)$$

With the addition of the active force to the dynamic stiffness matrix of the unit cell  $\mathbf{K}(\omega)$ , as done in Eq. (A.22),  $\omega(\kappa)$  can be computed. The transfer matrix method is commonly used for this aim, as described below for an active system.

SEM results in a transcendental matrix equation in the frequency domain, for the entries of  $\mathbf{K}(\omega)$  are harmonic functions of frequency, which have eigenvalues in a specific form. The direct method can be solved by finding a solution  $\kappa(\omega)$  that encompasses both propagative and dissipative modes (band gaps) for given real frequencies. First, it is necessary to condense Eq. (A.22), removing the inner-cell DOFs and obtaining  $\mathbf{K}_c$ ,

$$\begin{bmatrix} \hat{f}_0 \\ \hat{f}_3 \end{bmatrix} = \mathbf{K}_c(\omega) \begin{bmatrix} \hat{q}_0 \\ \hat{q}_3 \end{bmatrix}.$$

Assuming  $\hat{f}_1 = \hat{f}_2 = 0$  (absence of internal forces), Eq. (A.22) can be rearranged as follows:

$$\begin{cases} \hat{f}_0 = \mathbf{K}_1(1,1)\hat{q}_0 + \mathbf{K}_1(1,2)\hat{q}_1, & (I) \\ 0 = \mathbf{K}_1(2,1)\hat{q}_0 + \mathbf{D}_1\hat{q}_1 + \mathbf{K}_2(1,2)\hat{q}_2, & (II) \\ 0 = \mathbf{C}\hat{q}_1 + \mathbf{D}_2\hat{q}_2 + \mathbf{K}_3(1,2)\hat{q}_3, & (III) \\ \hat{f}_3 = \mathbf{K}_3(2,1)\hat{q}_2 + \mathbf{K}_3(2,2)\hat{q}_3. & (IV) \end{cases}$$

Isolating  $\hat{q}_1$  in (II):

$$\hat{q}_1 = -\frac{\mathbf{K}_1(2,1)}{\mathbf{D}_1}\hat{q}_0 - \frac{\mathbf{K}_2(2,1)}{\mathbf{D}_1}\hat{q}_2, \quad (2.51)$$

and isolating  $\hat{q}_2$  in (III):

$$\hat{q}_2 = -\frac{\mathbf{C}}{\mathbf{D}_2}\hat{q}_1 - \frac{\mathbf{K}_3(1,2)}{\mathbf{D}_2}\hat{q}_3. \quad (2.52)$$

One can substitute Eq. (2.52) into Eq. (2.51) and define

$$\mathbf{D}_3 = 1 - \frac{\mathbf{K}_2(1,2)\mathbf{C}}{\mathbf{D}_1\mathbf{D}_2},$$

to conclude that

$$\hat{q}_1 = -\frac{\mathbf{K}_1(2, 1)}{\mathbf{D}_1\mathbf{D}_3}\hat{q}_0 + \frac{\mathbf{K}_2(1, 2)\mathbf{K}_3(1, 2)}{\mathbf{D}_1\mathbf{D}_2\mathbf{D}_1}\hat{q}_3.$$

On the other hand, substituting Eq. (2.51) into Eq. (2.52), the result is

$$\hat{q}_2 = \frac{\mathbf{K}_1(2, 1)\mathbf{C}}{\mathbf{D}_1\mathbf{D}_2\mathbf{D}_3}\hat{q}_0 - \frac{\mathbf{K}_3(1, 2)}{\mathbf{D}_2\mathbf{D}_3}\hat{q}_3.$$

Finally, substituting into (I) and (IV), one has:

$$\hat{f}_0 = \left[ \mathbf{K}_1(1, 1) - \frac{\mathbf{K}_1(1, 2)\mathbf{K}_1(2, 1)}{\mathbf{D}_1\mathbf{D}_3} \right] \hat{q}_0 + \frac{\mathbf{K}_1(1, 2)\mathbf{K}_2(1, 2)\mathbf{K}_3(1, 2)}{\mathbf{D}_1\mathbf{D}_2\mathbf{D}_1}\hat{q}_3,$$

and

$$\hat{f}_3 = \frac{\mathbf{K}_3(2, 1)\mathbf{K}_1(2, 1)\mathbf{C}_2}{\mathbf{D}_1\mathbf{D}_2\mathbf{D}_3}\hat{q}_0 - \left[ \mathbf{K}_3(2, 2) - \frac{\mathbf{K}_3(2, 1)\mathbf{K}_3(1, 2)}{\mathbf{D}_2\mathbf{D}_3} \right] \hat{q}_3.$$

In matrix form (Eq. (2.53)), these equations show us the condensed matrix as a function of the matrices generated by the SEM of each of the three homogeneous segments of the unit cell

$$\mathbf{K}_c(\omega) = \begin{bmatrix} \mathbf{K}_1(1, 1) - \frac{\mathbf{K}_1(1, 2)\mathbf{K}_1(2, 1)}{\mathbf{D}_1\mathbf{D}_3} & \frac{\mathbf{K}_1(1, 2)\mathbf{K}_2(1, 2)\mathbf{K}_3(1, 2)}{\mathbf{D}_1\mathbf{D}_2\mathbf{D}_3} \\ \frac{\mathbf{K}_1(2, 1)\mathbf{C}_2\mathbf{K}_3(2, 1)}{\mathbf{D}_1\mathbf{D}_2\mathbf{D}_3} & \mathbf{K}_3(2, 2) - \frac{\mathbf{K}_3(2, 1)\mathbf{K}_3(1, 2)}{\mathbf{D}_2\mathbf{D}_3} \end{bmatrix}. \quad (2.53)$$

Generally, the transfer matrix relates displacement and force from one edge of the unit cell to the other and thus depends on the condensed dynamic stiffness matrix. Take the following definition, where  $\hat{q}_{0j+1} = \hat{q}_{3j}$  and  $\hat{f}_{0j+1} = -\hat{f}_{3j}$  (Hussein *et al.*, 2014),

$$\begin{bmatrix} \hat{q}_0 \\ \hat{f}_0 \end{bmatrix}_{j+1} = \mathbf{T}(\omega) \begin{bmatrix} \hat{q}_0 \\ \hat{f}_0 \end{bmatrix}_j.$$

This matrix is written as a function of the entries of  $\mathbf{K}_c(\omega)$  as follows (Hussein *et al.*, 2014)

$$\mathbf{T}(\omega) = \begin{bmatrix} -Z\mathbf{K}_c(1, 1) & Z \\ \mathbf{K}_c(2, 2)Z\mathbf{K}_c(1, 1) - \mathbf{K}_c(2, 1) & -\mathbf{K}_c(2, 2)Z \end{bmatrix} : Z = \mathbf{K}_c(1, 2)^{-1}. \quad (2.54)$$

Invoking *Bloch's Theorem*, once again, the following relation between the state vectors  $\mathbf{y} = \begin{bmatrix} \hat{q}_0 \\ \hat{f}_0 \end{bmatrix}^T$  is obtained.

$$\mathbf{y}_{j+1} = \lambda \mathbf{y}_j \quad | \quad \lambda = e^{i\mu} \in \mathbb{C} \quad \text{is called the Floquet multiplier.}$$

Combining this result with the definition of the transfer matrix, one arrive at the eigenvalue problem

$$\mathbf{T}(\omega)\mathbf{y}_j = \lambda \mathbf{y}_j. \quad (2.55)$$

The eigenvalues can be easily calculated by solving the associated characteristic equation and are  $\lambda_1 = e^{i\kappa L_c}$  and  $\lambda_2 = e^{-i\kappa L_c}$ , i.e., the two *Floquet* multipliers, were  $\mu = \kappa L$  (Hussein *et al.*, 2006). These eigenvalues are associated with the global (or effective) wavenumber  $\kappa$ , which governs wave propagation and dispersion in the material under analysis.

Solving the eigenvalue problem, one obtain the complex  $\lambda$ , so that

$$i\mu = \ln(|\lambda|) + i \arg(\lambda),$$

and therefore

$$\mu = \arg(\lambda) - i \ln(|\lambda|).$$

For any vector norm  $p$ , by the property of absolute homogeneity (Meyer, 2023)  $\| \mathbf{y}_{j+1} \|_p = |\lambda| \| \mathbf{y}_j \|_p$ . Thus, this result can be physically interpreted as follows: the real part of  $\mu$  is the phase shift between  $\mathbf{y}_{j+1}$  and  $\mathbf{y}_j$ , two adjacent unit cells and therefore repeats periodically, whereas the imaginary part of  $\mu$  is the negative logarithmic decrement of the displacement magnitudes between adjacent unit cells (Hussein *et al.*, 2006).

Conversely, the inverse method proposed here is based on finding the zeros of the characteristic equation of  $\mathbf{T}(\omega)$  expressed as

$$\det(\mathbf{T}(\omega) - e^{i\kappa L_c} \mathbf{I}_2) = 0, \quad (2.56)$$

where  $\mathbf{I}_2$  is the second order identity matrix. By expressing the entries of the transfer matrix as a function of  $\omega$  instead of  $\kappa$  and imposing real values of  $\kappa$ , one obtain an inverse method  $\omega(\kappa)$  used to generate most of the dispersions displayed in this subsection. The solution is complex and can be obtained by varying  $\kappa$  from  $[-l\pi, l\pi]$  to obtain the first  $l$  passbands. Nevertheless, the characteristic equation is transcendental and has infinite zeros, so an initial condition within a passband must be imposed for the numerical calculation. An alternative formulation for the inverse method via the transfer matrix using the SEM is proposed by repeating this procedure for initial conditions within different passbands. The algorithmic implementation of this method may be found in the LVA GitHub folder for both the acoustic duct of this subsection and the piezoelectric rod of the next subsection; it provided the dispersion curves simulated in Fig. 2.15, Fig. 2.16 (a) and (b), Fig. 2.18, Fig. 2.19, and Fig. 2.20.

Other methods to obtain the transfer matrix exceed the scope of this work but are worth mentioning. These include wave propagation approaches (Hussein *et al.*, 2006), direct via matrix exponential (Goto *et al.*, 2019), the SS-Riccati method (Assis *et al.*, 2019), and Wave

Finite Element (Mace; Manconi, 2007; Mencik, 2014). In this work, only the PWE method described in the Appendix and the FEM approach is extended to active systems and considered to compare results in Fig. 2.20.

For time-domain simulations, a FEM model is the standard approach. One way to derive the FEM discretization is the weak form obtained by the inner product of Eq. (2.49) with an admissible solution  $p^*$  (Atalla; Sgard, 2015) and considering, for example, the boundary conditions  $\frac{\partial p(0,t)}{\partial x} = \frac{\partial p(n_c L_3,t)}{\partial x} = 0$ , with  $f(x,t) = -\frac{4B}{\pi d^2} \frac{dG(t)}{dt} \sum_{n=1}^{n_c} \delta(x - x_n)$ , with  $x_2 - (n - 1)L_c$ .

Adding a simple viscous damping model, the equation becomes

$$\rho \frac{\partial^2 p}{\partial t^2}(x,t) = B \frac{\partial^2 p}{\partial x^2}(x,t) - \eta \frac{\partial p}{\partial t}(x,t) + f(x,t) \quad | \quad x \in \Omega = (0, n_c x_3). \quad (2.57)$$

Now, deriving the weak form,

$$\begin{aligned} W(p, p^*) &= \int_D p^*(s,t) \left( \rho \frac{\partial^2 p(s,t)}{\partial t^2} - B \frac{\partial^2 p(s,t)}{\partial s^2} + \eta \frac{\partial p}{\partial t}(s,t) + \rho f(s,t) \right) ds = 0, \\ W(p, p^*) &= \int_D \rho p^*(s,t) \frac{\partial^2 p(s,t)}{\partial t^2} + B \frac{\partial p^*(s,t)}{\partial s} \frac{\partial p(s,t)}{\partial s} + \eta p^*(s,t) \frac{\partial p}{\partial t}(s,t) + \rho p^*(s,t) f(s,t) ds + \dots \\ &\quad \dots - B \left( p^*(L,t) \frac{\partial p(L,t)}{\partial s} - p^*(0,t) \frac{\partial p(0,t)}{\partial s} \right) \\ W(p, p^*) &= \sum_{j=1}^{n_e} \int_{D_j} \rho p^*(s,t) \frac{\partial^2 p(s,t)}{\partial t^2} + B \frac{\partial p^*(s,t)}{\partial s} \frac{\partial p(s,t)}{\partial s} + \eta p^*(s,t) \frac{\partial p}{\partial t}(s,t) + \rho p^*(s,t) f(s,t) ds, \end{aligned}$$

where integration by parts and the natural boundary conditions were used. By the projection of the solution in a finite-dimensional space, as in the Appendix A, one has

$$\begin{aligned} p(x,t) &\approx \begin{bmatrix} 1 - \frac{x}{L_e} & \frac{x}{L_e} \end{bmatrix} \begin{bmatrix} p(x_e,t) \\ p(x_{e+1},t) \end{bmatrix} = \boldsymbol{\phi}^T \mathbf{p}_e(t), \\ \frac{\partial p(x,t)}{\partial x} &\approx \begin{bmatrix} -\frac{1}{L_e} & \frac{1}{L_e} \end{bmatrix} \begin{bmatrix} p(x_e,t) \\ p(x_{e+1},t) \end{bmatrix} = \frac{d\boldsymbol{\phi}(x)}{dx} \mathbf{p}_e(t), \quad \forall x \in D_e, \end{aligned}$$

implying, back to the weak integral form,

$$\begin{aligned} W(p, p^*) &\approx \sum_{e=0}^{n_e} \int_{D_e} \rho (\boldsymbol{\phi}(s)^T \mathbf{p}_e^*(t))^T \boldsymbol{\phi}(s)^T \ddot{\mathbf{p}}_e(t) + B \left( \frac{d\boldsymbol{\phi}(s)}{ds} \mathbf{p}_e^*(t) \right)^T \frac{d\boldsymbol{\phi}(s)}{ds} \mathbf{p}_e(t) + \dots \\ &\quad \dots + \eta (\boldsymbol{\phi}(x)^T \mathbf{p}_e^*(t))^T \boldsymbol{\phi}(s)^T \frac{d\mathbf{p}_e}{dt}(t) + \rho (\boldsymbol{\phi}(x)^T \mathbf{p}_e^*(t))^T f(s,t) ds = \\ &\quad \sum_{e=0}^{n_e} \rho \mathbf{p}_e^*(t)^T \int_{D_e} \boldsymbol{\phi}(s) \boldsymbol{\phi}(s)^T ds \ddot{\mathbf{p}}_e(t) + B \mathbf{p}_e^*(t)^T \int_{D_e} \frac{d\boldsymbol{\phi}(s)}{ds} \frac{d\boldsymbol{\phi}(s)}{ds} ds \mathbf{p}_e(t) + \dots \\ &\quad \dots + \eta \mathbf{p}_e^*(t)^T \int_{D_e} \boldsymbol{\phi}(s) \boldsymbol{\phi}(s)^T ds \frac{d\mathbf{p}_e}{dt}(t) + \rho \mathbf{p}_e^*(t)^T \int_{D_e} \boldsymbol{\phi}(s) f(s,t) ds, \end{aligned}$$

which equals

$$\begin{aligned} & \sum_{e=0}^{n_e} \mathbf{p}_e^*(t)^T \left( \rho \int_{D_e} \begin{bmatrix} (1 - \frac{s}{L_e})^2 & (1 - \frac{s}{L_e}) \frac{s}{L_e} \\ (1 - \frac{s}{L_e}) \frac{s}{L_e} & \frac{s^2}{L_e^2} \end{bmatrix} ds \ddot{\mathbf{p}}_e(t) + B \int_{D_e} \frac{1}{L_e^2} \begin{bmatrix} 1 & -1 \\ -1 & 1 \end{bmatrix} ds \mathbf{p}_e(t) + \dots \\ & \dots + \eta \int_{D_e} \begin{bmatrix} (1 - \frac{s}{L_e})^2 & (1 - \frac{s}{L_e}) \frac{s}{L_e} \\ (1 - \frac{s}{L_e}) \frac{s}{L_e} & \frac{s^2}{L_e^2} \end{bmatrix} ds \frac{d\mathbf{p}_e}{dt}(t) + \rho \int_{D_e} \phi(s) f(s, t) ds \right). \end{aligned}$$

Finally

$$\begin{aligned} W(p, p^*) \approx & \sum_{e=0}^{n_e} \mathbf{p}_e^*(t)^T \left( \rho L_e \begin{bmatrix} 2/6 & 1/6 \\ 1/6 & 2/6 \end{bmatrix} \ddot{\mathbf{p}}_e(t) + \eta L_e \begin{bmatrix} 2/6 & 1/6 \\ 1/6 & 2/6 \end{bmatrix} \frac{d\mathbf{p}_e}{dt}(t) + \dots \quad (2.58) \\ & \dots + B \frac{1}{L_e} \begin{bmatrix} 1 & -1 \\ -1 & 1 \end{bmatrix} \mathbf{p}_e(t) + \rho \int_{D_e} \phi(s) f(s, t) ds \right). \end{aligned}$$

The next step is assembling the system's DOFs to write the equation in terms of  $\mathbf{p}(t) = [p_1(t) \ p_2(t) \ \dots \ p_{n_e}(t)]^T \in \mathbb{R}^{n_e \times 1}$ . Take the matrix  $\mathbf{T}_e \in \mathbb{R}^{2 \times n_e}$  associated to the linear transformation from  $\mathbb{R}^{2 \times 1}$  to  $\mathbb{R}^{n_e \times 1}$ , defined by

$$\mathbf{T}_{e,ij} = \begin{cases} 1 & \text{if } i = 1 \text{ and } j = e \text{ or } i = 2 \text{ and } j = e + 1, \\ 0 & \text{otherwise.} \end{cases}$$

Substituting  $\mathbf{p}_e(t) = \mathbf{T}_e \mathbf{p}(t)$  and  $\mathbf{p}_e^*(t) = \mathbf{T}_e \mathbf{p}^*(t)$  in Eq. (2.58), one has

$$\begin{aligned} W(p, p^*) \approx & \sum_{e=0}^{n_e} \mathbf{p}^*(t)^T \left( \frac{\rho L_e}{6} \mathbf{T}_e^T \begin{bmatrix} 2 & 1 \\ 1 & 2 \end{bmatrix} \mathbf{T}_e \ddot{\mathbf{p}}(t) + \frac{\eta L_e}{6} \mathbf{T}_e^T \begin{bmatrix} 2 & 1 \\ 1 & 2 \end{bmatrix} \mathbf{T}_e \frac{d\mathbf{p}}{dt}(t) + \dots \quad (2.59) \\ & \dots + \frac{B}{L_e} \mathbf{T}_e^T \begin{bmatrix} 1 & -1 \\ -1 & 1 \end{bmatrix} \mathbf{T}_e \mathbf{p}(t) + \rho \mathbf{T}_e^T \int_{D_e} \phi(s) f(s, t) ds \right), \end{aligned}$$

with the last term

$$\begin{aligned} \int_{D_e} \phi(s) f(s, t) ds &= -\frac{4B}{\pi d^2} \int_{x_{e-1}}^{x_e} \phi(s) \sum_{n=1}^{n_c} \frac{dG_n(t)}{dt} \delta(s - x_n) ds = \\ &= -\frac{4B}{\pi d^2} \sum_{n=1}^{n_c} \phi(x_n) \frac{dG(t)}{dt} (\Delta(x_n - x_{e-1}) - \Delta(x_n - x_e)), \end{aligned}$$

where  $\Delta$  is the *Heaviside's* step and  $x_n$  is assumed to be one of the nodes of the FEM mesh; note that  $\Delta(x_n - x_{e-1}) - \Delta(x_n - x_e) = 1$  if  $x_n \in D_e = (x_{e-1}, x_e)$  and 0 otherwise.

Since  $W(p, p^*) = 0 \ \forall p^*$  in the trial function space, it is possible to write

$$\begin{aligned} \sum_{e=0}^{n_e} \frac{\rho L_e}{6} \mathbf{T}_e^T \begin{bmatrix} 2 & 1 \\ 1 & 2 \end{bmatrix} \mathbf{T}_e \ddot{\mathbf{p}}(t) + \frac{\eta L_e}{6} \mathbf{T}_e^T \begin{bmatrix} 2 & 1 \\ 1 & 2 \end{bmatrix} \mathbf{T}_e \frac{d\mathbf{p}}{dt}(t) + \frac{B}{L_e} \mathbf{T}_e^T \begin{bmatrix} 1 & -1 \\ -1 & 1 \end{bmatrix} \mathbf{T}_e \mathbf{p}(t) = \\ \frac{4B\rho}{\pi d^2} \sum_{n=1}^{n_c} \frac{dG}{dt} \mathbf{T}_e^T \phi(x_n) (\Delta(x_n - x_{e-1}) - \Delta(x_n - x_e)), \quad (2.60) \end{aligned}$$

defining  $\mathbf{M}_e = \frac{\rho L_e}{6} \begin{bmatrix} 2 & 1 \\ 1 & 2 \end{bmatrix}$ ,  $\mathbf{R}_e = \frac{\eta L_e}{6} \begin{bmatrix} 2 & 1 \\ 1 & 2 \end{bmatrix}$  and  $\mathbf{K}_e = \frac{B}{L_e} \begin{bmatrix} 1 & -1 \\ -1 & 1 \end{bmatrix}$  in Eq. (2.60) leads to

$$\sum_{j=0}^{n_e} \mathbf{T}_e^T \mathbf{M}_e \mathbf{T}_e \ddot{\mathbf{p}}(t) + \mathbf{T}_e^T \mathbf{R}_e \mathbf{T}_e \dot{\mathbf{p}}(t) + \mathbf{T}_e^T \mathbf{K}_e \mathbf{T}_e \mathbf{p}(t) = \frac{4B\rho}{\pi d^2} \sum_{n=1}^{n_c} \mathbf{T}_e^T \frac{dG}{dt} \phi(x_n) (\Delta(x_n - x_j) - \Delta(x_n - x_{j+1})),$$

where  $\mathbf{M} = \sum_{j=0}^{n_e} \mathbf{T}_e^T \mathbf{M}_e \mathbf{T}_e$ ,  $\mathbf{R} = \sum_{j=0}^{n_e} \mathbf{T}_e^T \mathbf{R}_e \mathbf{T}_e$  and  $\mathbf{K} = \sum_{j=0}^{n_e} \mathbf{T}_e^T \mathbf{K}_e \mathbf{T}_e$  are the mass, damping, and stiffness matrices, which are sparse and symmetric; thus the finite-dimensional equation of motion is derived with  $\mathbf{q}(t) = \mathbf{p}(t)$  and in this particular case of *Rayleigh* viscous damping,  $\mathbf{R} = \frac{\eta}{\rho} \mathbf{M}$ .

Consider a simple feedback law of a proportional-integral-derivative type, defined for applied volume velocity on the  $n$ -th cell  $G_{fb}^n : [0, T] \rightarrow \mathbb{R}$  with respect to the concentrated measured pressure  $p_s^{n-a} : [0, T] \rightarrow \mathbb{R}$  of the corresponding sensor located  $a \in \mathbb{Z}$  cells distant. Thus, the feedback law is defined, with gains  $\gamma_D, \gamma_P, \gamma_{DD} \in \mathbb{R}$  as follows

$$G_{fb}^n(t) = \gamma_D p_s^{n-a}(t) + \gamma_P \int_0^t p_s^{n-a}(t) dt + \gamma_{DD} \frac{dp_s^{n-a}(t)}{dt} \quad \forall n \in \mathbb{Z} \mid a < n \leq n_c. \quad (2.61)$$

But on Eq. (A.3), the applied feedback effort is given in volume acceleration (Atalla; Sgard, 2015), so one need to define the feedback effort signal  $u : [0, T] \rightarrow \mathbb{R}^{n_c}$  such that  $\mathbf{u}(t) = -\frac{B}{A} \frac{d\mathbf{G}_v}{dt}$ , being  $\mathbf{G}_v$  a vector with all the concentrated efforts on actuators along the structure. Then,  $\mathbf{u}_a(t) = \mathbf{U}\mathbf{u}(t)$  is the image vector of  $u$  at any instant of time transformed to  $\mathbb{R}^{n_d}$  by completing the non-actuated DOFs with zeros, using the following matrix coordinates for  $\mathbf{U}$

$$U_{ij} = \begin{cases} 1 & \text{if } i = n_2 + (j + a - 1)n_e \quad \forall j \in \mathbb{Z} \mid 1 \leq j \leq n_c - a; \\ 0 & \text{otherwise,} \end{cases} \quad (2.62)$$

where  $n_e$  is the number of finite elements per unit cell. Thus, the feedback law in Eq. (2.61) in matrix form and units of volume acceleration is

$$\mathbf{u}_a(t) = \mathbf{\Gamma}_D \dot{\mathbf{q}}(t) + \mathbf{\Gamma}_P \mathbf{q}(t) + \mathbf{\Gamma}_{DD} \ddot{\mathbf{q}}(t), \quad (2.63)$$

with the matrices  $\mathbf{\Gamma}$  defined with a generalized feedback gain  $\gamma \in \mathbb{R}$  as coordinates in the following manner-  $n_2$  is the DOF where the actuator signal is applied,  $x_2$  on Fig. 2.14. Then

$$\Gamma_{i,j} = \begin{cases} -\frac{B}{A} \gamma & \text{if } i = (k + a)n_2 \text{ and } j = kn_1, \forall k \in \mathbb{Z} \mid 1 \leq k \leq n_c - a; \\ 0 & \text{otherwise.} \end{cases} \quad (2.64)$$

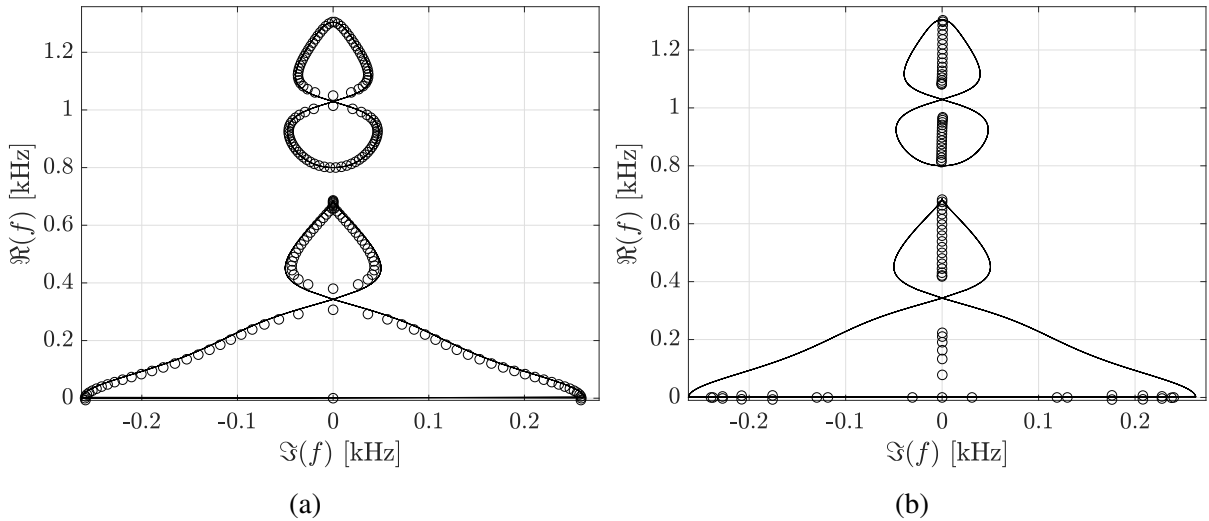


Figure 2.15 – Bulk-boundary correspondence for local proportional feedback. Complex frequency plane of the system with the feedback defined in Eq. (2.61) for local ( $r = 0$ ) and proportional action ( $\gamma_D = \gamma_{DD} = 0$ ), with gain  $\gamma_P = 0.015$ . Dispersion relations (solid curves) and eigenmodes of the structure (circles) are compared under (a) PBC and (b) OBC.

Substitution of the above law on Eq. (A.3) leads to

$$\bar{\mathbf{M}}\ddot{\mathbf{q}}(t) + \bar{\mathbf{R}}\dot{\mathbf{q}}(t) + \bar{\mathbf{K}}\mathbf{q}(t) = \mathbf{w}_a(t), \quad (2.65)$$

which can be numerically integrated to give the solution  $\mathbf{q}(t)$ . On the other hand, the polynomial eigenvalue problem associated with Eq. (2.65) with  $\mathbf{w}_a = \mathbf{0}$ ,

$$(-\omega^2\bar{\mathbf{M}} + i\omega\bar{\mathbf{R}} + \bar{\mathbf{K}})\hat{\mathbf{q}}(\omega) = 0, \quad (2.66)$$

gives the free-vibration modes. The latter was done to compute the stable transient response to a tone-burst excitation of central frequency  $250\text{Hz}$  and 15 cycles in Fig. 2.16 whereas the former was used to compute the poles of the system displayed as bubbles on the complex plane in Fig. 2.15. Furthermore, from Eq. (2.65), the forced response in the frequency domain related to an applied force in the  $n$ -th DOF is trivially obtained as the solution of

$$(-\omega^2\bar{\mathbf{M}} + i\omega\bar{\mathbf{R}} + \bar{\mathbf{K}})\hat{\mathbf{q}}(\omega) = \hat{\mathbf{w}}_a(\omega), \quad (2.67)$$

where  $\hat{w}_a(\omega)_i = 1$  if  $i = n$  and  $\hat{w}_a(\omega)_i = 0$  otherwise, giving the simulations of Fig. 2.17.

## 2.2.2 Piezoelectric material under longitudinal vibration

Consider that the one-dimensional material based on the unit cell displayed in Fig. 2.21 is made of rod piezos (PZT). Let the  $x$ -axis be the longitudinal direction of the cell

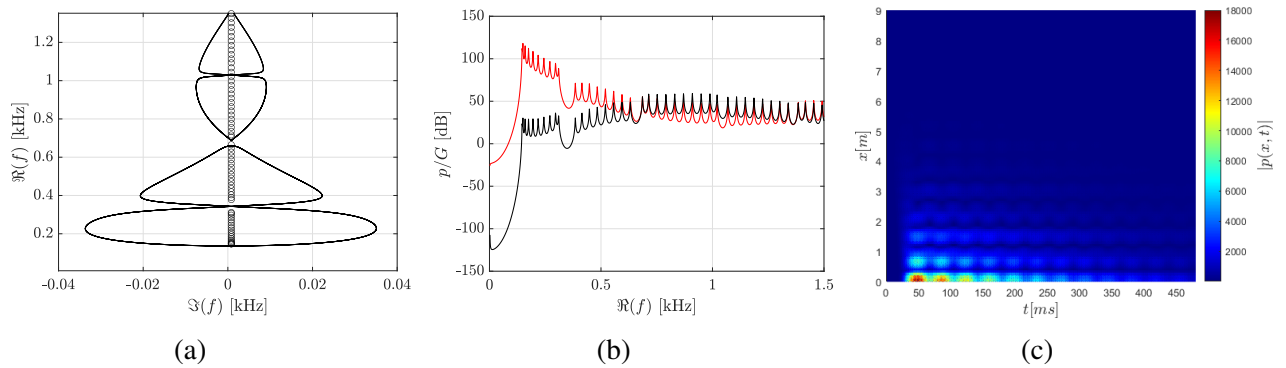


Figure 2.16 – Stable duct under proportional feedback gain. (a) Bulk-boundary correspondence on the dispersion relation for the structure under OBCs. (b) FRF of both ends of the duct, the left end in red and the right end in black, for external volume velocity applied to the central DOF of the duct’s mesh. (c) Transient response to a tone-burst excitation highlighting non-reciprocal wave propagation resulting from the NHSE.

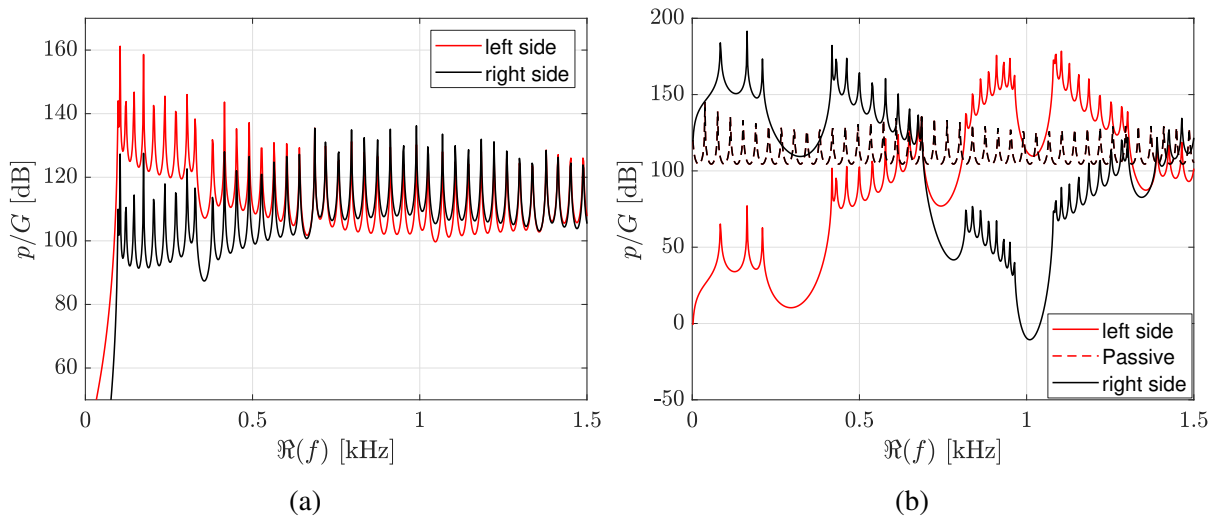


Figure 2.17 – FRF of the non-reciprocal periodic duct with excitation at the central DOF. FRF for proportional feedback under OBC, fixed viscous damping with  $\eta = 12.5$ , 18 cells, and (a)  $\gamma_P = -0.0015$  (b)  $\gamma_P = 0.015$ . The FRF of the passive counterpart ( $\gamma_P = 0$ ) is also included in (b). to highlight the frequency-dependent energy concentration.

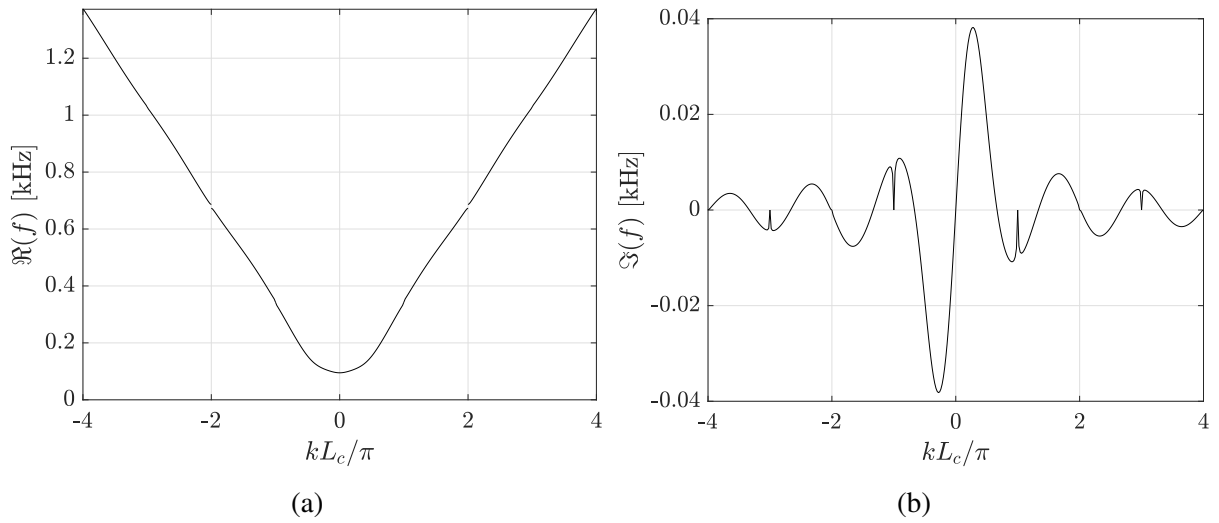


Figure 2.18 – Dispersion diagram  $\omega(\kappa)$  of a non-reciprocal duct with non-local proportional feedback. First four pass-bands of the dispersion relation for non-local undamped proportional feedback with  $\eta = 0$ ,  $\gamma_P = -0.0015$  and  $a = 2$  (a) real frequency against wavenumber and (b) imaginary frequency against wavenumber.

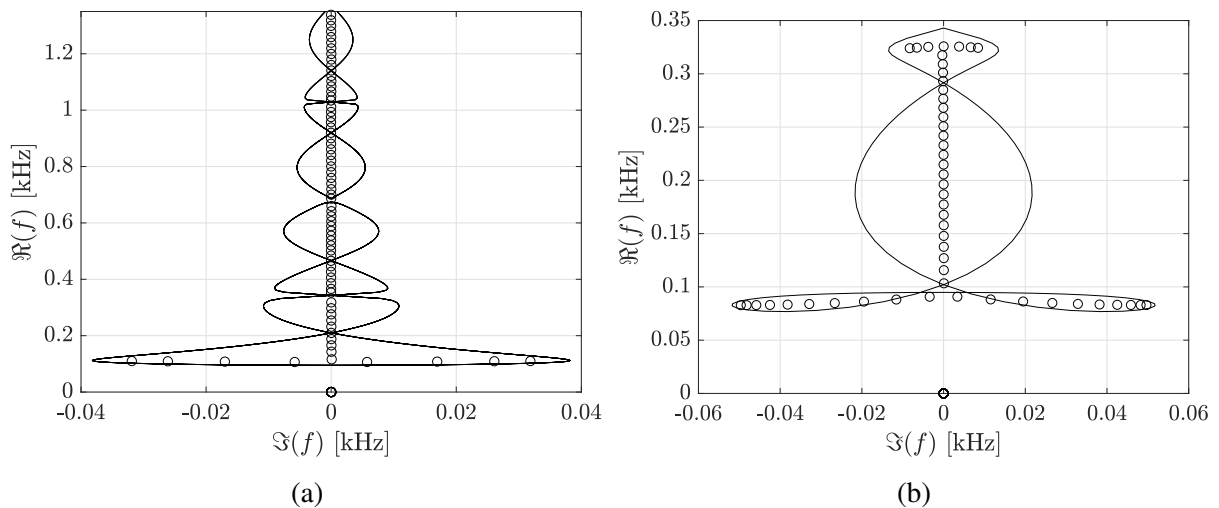


Figure 2.19 – Bulk-boundary correspondance of non-local proportional feedback. The dispersion diagrams were computed using  $\eta = 0$  and  $\gamma_P = -0.0015$ , whereas the vibration modes assume 18 cells and open-open acoustic duct. The non-locality feedback was defined by (a)  $a = 1$  and (b)  $a = 2$ .

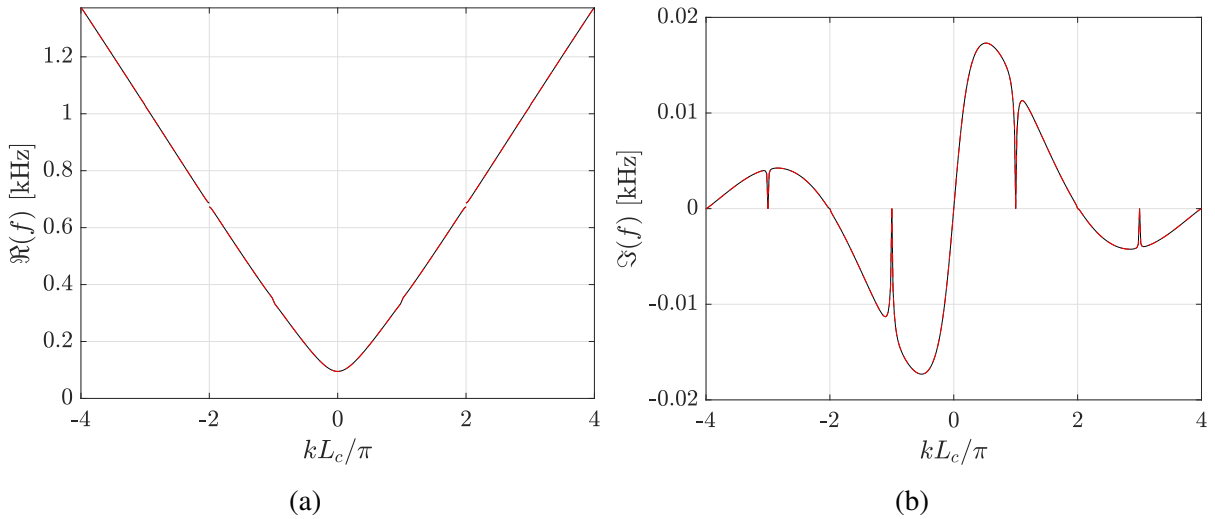


Figure 2.20 – Compared dispersion diagrams using PWE and SEM methods. The dispersions were computed using PWE (dashed red lines) and SEM (solid black lines) applied to the unit cell of Fig. 2.14 with  $\eta = 0$ ,  $\gamma_P = 0.015$ , and  $a = 0$ .

and, in addition, let the PZT material (ceramics) be plated with electrodes at the end cross-sections;  $\sigma$  and  $\varepsilon$  denote, respectively, the normal stress and normal strain, while  $E$  and  $D$  denote, respectively, the scalar electric field and the electric displacement in the same direction; let's assume that  $\sigma$ ,  $E$ , and  $D$  do not vary within the cross-section. Additionally, consider the reasonable hypothesis that the electric field and electric displacement are uniform inside the PZT material (Won *et al.*, 1992) and that the material properties are constant.

As shown in (Braghini *et al.*, 2021; Won *et al.*, 1992), under the previous hypothesis, the following equations may be derived for a homogeneous piece of PZT material with cross-sectional area  $A$ :

$$\sigma(x, t) = Y^E \varepsilon(x, t) - eE(t) \quad (2.68)$$

$$D(x, t) = e\varepsilon(x, t) + \alpha^\varepsilon E(t) \quad (2.69)$$

$$N(x, t) = Y^D \frac{\partial u(x, t)}{\partial x} A - \frac{e}{\alpha} Q(t) \quad (2.70)$$

$$Q(t) = \frac{eA}{L} \begin{bmatrix} -1 & 1 \end{bmatrix} \begin{bmatrix} u(0) \\ u(L) \end{bmatrix} - \frac{\alpha A}{L} V(t), \quad (2.71)$$

with  $Y^E$  denoting the *Young's* modulus measured at constant electric field,  $Y^D = \left( Y^E + \frac{e^2}{\alpha^\varepsilon} \right)$  the *Young's* modulus measured at constant electric displacement,  $\alpha^\varepsilon$  denoting the relative permittivity of the medium measured at constant strain, and  $e$  the piezoelectric constant. Recalling

that  $N(x, t) = \sigma(x, t)A$  – the axial internal effort distribution along –,  $\varepsilon(x, t) = \frac{\partial u(x, t)}{\partial x}$  – the strain –, and  $Q(x, t) = D(x, t)A$  – the electric charge distribution.

The subscript  $( )_e$  in scalars and vectors and the superscript  $( )^e$  in matrices refer to each finite element,  $( )_s$  refers to the PZT sensor variable, and  $( )_a$  refers to the PZT actuator variables.

The above equations can be shown to give rise to the following wave equation (Li; Guo, 2016):

$$\frac{\partial}{\partial x} \left[ Y^D A \frac{\partial u(x, t)}{\partial x} \right] = \rho A \ddot{u}(x, t). \quad (2.72)$$

By Eq. (2.69), the definition of the voltage difference between two boundaries of a homogeneous material spaced by  $L$ , and assuming also that  $D$  is uniform in  $x$ ,

$$V(t) = - \int_0^L E dx = \frac{e}{\alpha^\varepsilon} [u(L, t) - u(0, t)] - \frac{L}{\alpha^\varepsilon A} Q(t), \quad (2.73)$$

which can be rewritten to give the expression of  $Q$  – the electric charge – as follows:

$$Q(t) = \frac{eA}{L} \begin{bmatrix} -1 & 1 \end{bmatrix} \begin{bmatrix} u(0, t) \\ u(L, t) \end{bmatrix} - \frac{\alpha^\varepsilon A}{L} V(t). \quad (2.74)$$

Transforming Eq. (2.73) from time to frequency domain, one obtains

$$\hat{V}(\omega) = \frac{e}{\alpha} [\hat{u}(L, \omega) - \hat{u}(0, \omega)] - \frac{\hat{Q}(\omega)L}{\alpha A}. \quad (2.75)$$

Also, substituting Eq. (2.71) in Eq. (2.70) results in

$$\hat{N}(x, \omega) = \left( Y^E + \frac{e^2}{\alpha^\varepsilon} \right) A \frac{d\hat{u}(x, \omega)}{dx} - \frac{e}{\alpha^\varepsilon} \hat{Q}(\omega). \quad (2.76)$$

Now, consider an electric open boundary condition for the sensor segment of the cell. This assumption implies  $\hat{Q}(\omega) = 0$  and, hence, from Eq. (2.75),

$$\hat{V}_s(\omega) = \frac{e}{\alpha^\varepsilon} [\hat{u}_s(L, \omega) - \hat{u}_s(0, \omega)], \quad (2.77)$$

from Eq. (2.71),

$$\frac{d\hat{\varphi}_s(x, \omega)}{dx} = \frac{e}{\alpha^\varepsilon} \frac{d\hat{u}(x, \omega)}{dx},$$

and from Eq. (2.76),

$$\hat{N}_s(x, \omega) = \left( Y^E + \frac{e^2}{\alpha^\varepsilon} \right) A \frac{d\hat{u}(x, \omega)}{dx}. \quad (2.78)$$

Additionally, it can be shown from Eq. (2.72) that the dispersion relation for the uniform PZT rod is

$$k = \omega \sqrt{\frac{\rho}{Y^D}}.$$

Imposing a wave solution of the form

$$\hat{u}(x, \omega) = p e^{ik(\omega)x} + r e^{-ik(\omega)x}, \quad (2.79)$$

where  $p_s, r_s, p_a, r_a \in \mathbb{C}$  are propagated and reflected wave amplitudes in the sensor and actuator domains, with the subindices indicating its location, one can derive

$$\frac{d\hat{u}(x, \omega)}{dx} = ik(\omega) (p e^{ik(\omega)x} - r e^{-ik(\omega)x}).$$

The oscillatory terms mean waves propagating to the right and to the left. Applying this solution in the sensor domain  $x \in [0, L_s]$ , Eq. (2.78) can be rewritten as

$$\hat{N}_s(x, \omega) = \xi(\omega) (p_s e^{ik(\omega)x} - r_s e^{-ik(\omega)x}) \quad : \quad \xi(\omega) = Y^D A ik(\omega). \quad (2.80)$$

Hereafter, frequency dependency may be omitted for the sake of simplicity. Writing Eq. (2.79) in matrix form for the sensor domain,

$$\begin{bmatrix} \hat{u}_s(0) \\ \hat{u}_s(L) \end{bmatrix} = \begin{bmatrix} 1 & 1 \\ e^{ikL_s} & e^{-ikL_s} \end{bmatrix} \begin{bmatrix} p_s \\ r_s \end{bmatrix},$$

from which comes

$$\begin{bmatrix} p_s \\ r_s \end{bmatrix} = \frac{1}{e^{-ikL_s} - e^{ikL_s}} \begin{bmatrix} e^{-ikL_s} & -1 \\ -e^{ikL_s} & 1 \end{bmatrix} \begin{bmatrix} \hat{u}_s(0) \\ \hat{u}_s(L) \end{bmatrix}. \quad (2.81)$$

Additionally, from Eq. (2.80),

$$\begin{bmatrix} \hat{N}_s(0) \\ \hat{N}_s(L) \end{bmatrix} = \xi \begin{bmatrix} 1 & -1 \\ e^{ikL_s} & e^{-ikL_s} \end{bmatrix} \begin{bmatrix} p_s \\ r_s \end{bmatrix},$$

and Eq. (2.81) yields

$$\begin{bmatrix} \hat{N}_s(0) \\ \hat{N}_s(L) \end{bmatrix} = \frac{\xi}{e^{-ikL_s} - e^{ikL_s}} \begin{bmatrix} e^{-ikL_s} + e^{ikL_s} & -2 \\ 2 & -e^{-ikL_s} - e^{ikL_s} \end{bmatrix} \begin{bmatrix} \hat{u}_s(0) \\ \hat{u}_s(L) \end{bmatrix}.$$

Substituting the internal reactions by external loads  $\hat{f}(0) = -\hat{N}(0)$  and  $\hat{f}(L) = \hat{N}(L)$ ,

$$\begin{bmatrix} \hat{f}_s(0) \\ \hat{f}_s(L) \end{bmatrix} = \frac{\xi}{e^{-ikL_s} - e^{ikL_s}} \begin{bmatrix} -e^{-ikL_s} - e^{ikL_s} & 2 \\ 2 & -e^{-ikL_s} - e^{ikL_s} \end{bmatrix} \begin{bmatrix} \hat{u}_s(0) \\ \hat{u}_s(L) \end{bmatrix},$$

which can finally be written, highlighting the dynamic stiffness matrix  $\mathbf{K}_p^s$ , as

$$\begin{bmatrix} \hat{f}_s(0) \\ \hat{f}_s(L) \end{bmatrix} = \mathbf{K}_p^s \begin{bmatrix} \hat{u}_s(0) \\ \hat{u}_s(L) \end{bmatrix}, \quad (2.82)$$

where

$$\mathbf{K}_p^s = \frac{-i\xi}{\text{sen}(kL_s)} \begin{bmatrix} \cos(kL_s) & -1 \\ -1 & \cos(kL_s) \end{bmatrix}.$$

On the other hand, in the actuator the electric boundary condition is an applied feedback gain of the form  $\hat{V}_a(\omega) = K_g [\hat{u}_s(L, \omega) - \hat{u}_s(0, \omega)]$ , one can verify from Eq. (2.75) that

$$\hat{Q}_a(\omega) = \frac{eA}{L_a} [\hat{u}_a(L, \omega) - \hat{u}_a(0, \omega)] - K_g \frac{\alpha^\varepsilon A}{L_a} [\hat{u}_s(L, \omega) - \hat{u}_s(0, \omega)],$$

and, from Eq. (2.71),

$$\frac{d\hat{\varphi}_a(x, \omega)}{dx} = \frac{e}{\alpha^\varepsilon} \frac{d\hat{u}(x, \omega)}{dx} + \frac{1}{L_a} K_g [\hat{u}_s(L, \omega) - \hat{u}_s(0, \omega)] - \frac{e}{\alpha^\varepsilon L_a} [\hat{u}_a(L, \omega) - \hat{u}_a(0, \omega)].$$

Also, from Eq. (2.76),

$$\hat{N}_a(x, \omega) = \left( Y^E + \frac{e^2}{\alpha} \right) A \frac{d\hat{u}(x, \omega)}{dx} + \frac{eA}{L_a} K_g [\hat{u}_s(L, \omega) - \hat{u}_s(0, \omega)] - \frac{e^2 A}{\alpha^\varepsilon L_a} [\hat{u}_a(L, \omega) - \hat{u}_a(0, \omega)].$$

Again, considering the wave solution, this equation can be rewritten as

$$\hat{N}_a(x, \omega) = \xi (p_a e^{i\kappa(\omega)x} - r_a e^{-i\kappa(\omega)x}) + \frac{eA}{L_a} K_g [\hat{u}_s(L, \omega) - \hat{u}_s(0, \omega)] - \frac{e^2 A}{\alpha^\varepsilon L_a} [\hat{u}_a(L, \omega) - \hat{u}_a(0, \omega)], \quad (2.83)$$

yielding

$$\begin{bmatrix} \hat{N}_a(0) \\ \hat{N}_a(L) \end{bmatrix} = \xi \begin{bmatrix} 1 & -1 \\ e^{ikL_a} & e^{-ikL_a} \end{bmatrix} \begin{bmatrix} p_a \\ r_a \end{bmatrix} - \frac{e^2 A}{\alpha^\varepsilon L_a} \begin{bmatrix} -1 & 1 \\ -1 & 1 \end{bmatrix} \begin{bmatrix} \hat{u}_a(0) \\ \hat{u}_a(L) \end{bmatrix} + \frac{eAK_g}{L_a} \begin{bmatrix} -1 & 1 \\ -1 & 1 \end{bmatrix} \begin{bmatrix} \hat{u}_s(0) \\ \hat{u}_s(L) \end{bmatrix},$$

which becomes, by substituting similar wave amplitudes as in Eq. (2.81) similarly as done in the sensor,

$$\begin{bmatrix} \hat{f}_a(0) \\ \hat{f}_a(L) \end{bmatrix} = (\mathbf{K}_p^a + \mathbf{K}_a) \begin{bmatrix} \hat{u}_a(0) \\ \hat{u}_a(L) \end{bmatrix} + \mathbf{\Gamma}_c \begin{bmatrix} \hat{u}_s(0) \\ \hat{u}_s(L) \end{bmatrix}, \quad (2.84)$$

where

$$\mathbf{K}_p^a = \frac{-i\xi}{\text{sen}(kL_a)} \begin{bmatrix} \cos(kL_a) & -1 \\ -1 & \cos(kL_a) \end{bmatrix}, \quad \mathbf{K}_a = \frac{e^2 A}{\alpha^\varepsilon L_a} \begin{bmatrix} -1 & 1 \\ 1 & -1 \end{bmatrix}.$$

Note that the short-circuited PZT material has the frequency-dependent dynamic stiffness matrix  $\mathbf{K}_{sc}(\omega) = \mathbf{K}_p^a(\omega) + \mathbf{K}_a$ , which is the passive contribution to the dynamic stiffness relation of interest.  $\mathbf{\Gamma}_c$  is the feedback interaction contribution. If the feedback gain  $K_g = 0$ ,  $\mathbf{\Gamma}_c$  becomes the null matrix, and the  $\hat{V} = 0$ , equivalent to a short-circuit boundary condition.

Note that, referring to Fig. 2.21  $\hat{u}_s(0) = \hat{u}(x_0)$ ,  $\hat{u}_s(L) = \hat{u}(x_1) = \hat{u}_a(0)$ , and  $\hat{u}_a(L) = \hat{u}(x_2)$ ,  $\hat{f}_s(0) = \hat{f}(x_0)$ ,  $\hat{f}_s(L) = \hat{f}_a(0)$ , and  $\hat{f}_a(L) = \hat{f}(x_2)$ . Concatenating the dynamic stiffness matrix from the sensor – Eq. (2.82) – and the actuator segments – Eq. (2.84) –, one can derive the dynamic stiffness matrix of the unit cell,  $\mathbf{D}(\omega)$  as in Eq. (A.20),

$$\begin{bmatrix} \hat{\mathbf{f}}(x_0) \\ \hat{\mathbf{f}}(x_1) \\ \hat{\mathbf{f}}(x_2) \end{bmatrix} = \begin{bmatrix} \mathbf{K}_p^s(1,1) & \mathbf{K}_p^s(1,2) & 0 \\ \mathbf{K}_p^s(2,1) + \mathbf{\Gamma}_c(1,1) & \mathbf{K}_p^s(2,2) + \mathbf{\Gamma}_c(1,2) + \mathbf{K}_{sc}(1,1) & \mathbf{K}_{sc}(1,2) \\ \mathbf{\Gamma}_c(2,1) & \mathbf{K}_{sc}(2,1) + \mathbf{\Gamma}_c(2,2) & \mathbf{K}_{sc}(2,1) \end{bmatrix} \begin{bmatrix} \hat{\mathbf{u}}(x_0) \\ \hat{\mathbf{u}}(x_1) \\ \hat{\mathbf{u}}(x_2) \end{bmatrix}.$$

where  $\hat{\mathbf{u}}$  is the vector with the degrees of freedom of the unit cell, while  $\hat{\mathbf{f}}$  is the vector with the corresponding external forces. Thus,  $\mathbf{D}(\omega)$  may be condensed and converted in the transfer matrix using Eq. (2.54). Finally, the problem in Eq. (2.56) may be solved to get the dispersion relations in Fig. 2.22, Fig. 2.23, Fig. 2.25, and Fig. 2.26.

Assembling the cells into a finite metastructure, one may obtain the spectral global equation, where the degrees of freedom and forces of the whole structure are on the global vectors  $\hat{\mathbf{u}}_g$  and  $\hat{\mathbf{f}}_g$ ; this may be used to compute frequency responses shown in Fig. 2.24.

For the FEM formulation of this problem, the projection of the solution in a finite-dimensional space, as in Eq. (A.1) (vide Appendix A), implies that the linear function approximates displacements:

$$u(x, t) \approx \begin{bmatrix} 1 - \frac{x}{L_e} & \frac{x}{L_e} \end{bmatrix} \begin{bmatrix} u(x_j, t) \\ u(x_{j+1}, t) \end{bmatrix} = \boldsymbol{\phi}(x)^T \mathbf{u}_j(t), \quad \forall x \in D_j.$$

Thus, the strain is

$$\varepsilon(x, t) \approx \begin{bmatrix} -\frac{1}{L_e} & \frac{1}{L_e} \end{bmatrix} \begin{bmatrix} u(x_j, t) \\ u(x_{j+1}, t) \end{bmatrix} = \frac{d\boldsymbol{\phi}(x)^T}{dx} \mathbf{u}_j(t), \quad \forall x \in D_j.$$

With this approximation and the variational principle of least action, i.e., finding the equations of motion as the stationary points of the functional

$$S \left( u, \frac{\partial u}{\partial t} \right) = \int_{t_1}^{t_2} K \left( \frac{\partial u}{\partial t} \right) - P(u) + W dt,$$

where  $K, P$ , and  $W$  are kinetic energy, potential energy (elastic, mutual, and dielectric), and

external work applied in the system, respectively, i.e.,

$$\begin{aligned}
K &= A \int_0^L \frac{1}{2} \rho \left( \frac{\partial u}{\partial t} \right)^2 dx \approx \sum_{i=1}^{N_e} A \rho_e \frac{1}{2} \int_0^{L_e} (\boldsymbol{\phi}(x)^T \dot{\mathbf{u}}_j(t))^T \boldsymbol{\phi}(x)^T \dot{\mathbf{u}}_j(t) dx = \\
&\frac{1}{2} \sum_{i=1}^{N_e} A \rho_e \begin{bmatrix} \dot{u}(x_j, t) & \dot{u}(x_{j+1}, t) \end{bmatrix} \int_0^{L_e} \begin{bmatrix} (1 - \frac{x}{L_e})^2 & (1 - \frac{x}{L_e}) \frac{x}{L_e} \\ (1 - \frac{x}{L_e}) \frac{x}{L_e} & \frac{x^2}{L_e^2} \end{bmatrix} dx \begin{bmatrix} \dot{u}(x_j, t) \\ \dot{u}(x_{j+1}, t) \end{bmatrix} = \\
&\sum_{i=1}^{N_e} \frac{m}{L_e} \begin{bmatrix} \dot{u}(x_j, t) & \dot{u}(x_{j+1}, t) \end{bmatrix} \begin{bmatrix} 2L_e/6 & L_e/6 \\ L_e/6 & 2L_e/6 \end{bmatrix} \begin{bmatrix} \dot{u}(x_j, t) \\ \dot{u}(x_{j+1}, t) \end{bmatrix} = \\
&\sum_{i=1}^{N_e} \begin{bmatrix} \dot{u}(x_j, t) & \dot{u}(x_{j+1}, t) \end{bmatrix} \frac{m}{6} \begin{bmatrix} 2 & 1 \\ 1 & 2 \end{bmatrix} \begin{bmatrix} \dot{u}(x_j, t) \\ \dot{u}(x_{j+1}, t) \end{bmatrix}, \\
P &= A \int_0^L \frac{1}{2} \left( Y + \frac{e^2}{\alpha} \right) \varepsilon(x, t)^2 - \frac{e}{\alpha} \varepsilon(x, t) D(t) + \frac{1}{2\alpha} D(t)^2 dx \approx \\
&A \sum_{j=1}^{N_e} \int_0^{L_e} \frac{1}{2} \left( Y + \frac{e^2}{\alpha} \right) \left( \frac{d\boldsymbol{\phi}(x)}{dx} \mathbf{u}_j(t) \right)^T \frac{d\boldsymbol{\phi}(x)}{dx} \mathbf{u}_j(t) + \dots \\
&\dots - \frac{eA}{\alpha} \frac{d\boldsymbol{\phi}(x)}{dx} \mathbf{u}_j(t) D(t) + \frac{A}{2\alpha} D(t)^2 dx = \\
&A \sum_{j=1}^{N_e} \frac{1}{2} \left( Y + \frac{e^2}{\alpha} \right) \mathbf{u}_j(t)^T \int_0^{L_e} \frac{d\boldsymbol{\phi}(x)}{dx} \frac{d\boldsymbol{\phi}(x)}{dx} dx \mathbf{u}_j(t) + \dots \\
&\dots - \frac{eA}{\alpha} \frac{d\boldsymbol{\phi}(x)}{dx} \int_0^{L_e} dx \mathbf{u}_j(t) D(t) + \frac{A}{2\alpha} D(t)^2 \int_0^{L_e} dx = \\
&A \sum_{j=1}^{N_e} \frac{1}{2L_e} \left( Y + \frac{e^2}{\alpha} \right) \mathbf{u}_j(t)^T \begin{bmatrix} 1 & -1 \\ -1 & 1 \end{bmatrix} \mathbf{u}_j(t) + \dots \\
&\dots - \frac{e}{\alpha} \begin{bmatrix} -1 & 1 \end{bmatrix} \begin{bmatrix} u(x_j, t) \\ u(x_{j+1}, t) \end{bmatrix} Q_j(t) + \frac{L_e}{2\alpha A} Q_j(t)^2, \\
W &= \sum_{j=1}^{N_e} N(x_j) u(x_j, t) + N(x_{j+1}, t) u(x_{j+1}, t) + V(t) Q(t). \tag{2.85}
\end{aligned}$$

The Principle of Least Action consists in finding the stationary points of  $S$ , i.e., the functions  $\{u(x_j, t), \dot{u}(x_j, t)\}_{j=1}^{N_e}$  for which deviations from the approximated  $S$  equals zero in the first order. This is equivalent to considering small deviations  $\{\delta u(x_j, t), \delta \dot{u}(x_j, t)\}_{j=1}^{N_e}$ , constrained to be zero at the integration limits (see, for example, chapter 19 of (Feynman *et al.*, 1965)).

The resultant equation is

$$\delta S(\delta u, \delta \dot{u}) = \delta \int_{t_1}^{t_2} K(\delta \dot{u}) - P(u) + W dt = 0.$$

One can then derive the following equation (Won *et al.*, 1992):

$$\frac{mL_e}{6} \begin{bmatrix} 2 & 1 \\ 1 & 2 \end{bmatrix} \begin{bmatrix} \ddot{u}(0) \\ \ddot{u}(L) \end{bmatrix}_e + \left( Y + \frac{e^2}{\alpha} \right) \frac{A}{L_e} \begin{bmatrix} 1 & -1 \\ -1 & 1 \end{bmatrix} \begin{bmatrix} u(0) \\ u(L) \end{bmatrix}_e - \frac{e}{\alpha} \begin{bmatrix} -1 \\ 1 \end{bmatrix} Q = \begin{bmatrix} f(0) \\ f(L) \end{bmatrix}_e, \quad (2.86)$$

and with substitution of Eq. (2.74),

$$\frac{mL_e}{6} \begin{bmatrix} 2 & 1 \\ 1 & 2 \end{bmatrix} \begin{bmatrix} \ddot{u}(0) \\ \ddot{u}(L) \end{bmatrix}_e + \left( Y + \frac{e^2}{\alpha} \right) \frac{A}{L_e} \begin{bmatrix} 1 & -1 \\ -1 & 1 \end{bmatrix} \begin{bmatrix} u(0) \\ u(L) \end{bmatrix}_e - \frac{e^2 A}{\alpha L_a} \begin{bmatrix} 1 & -1 \\ -1 & 1 \end{bmatrix} \begin{bmatrix} u(0) \\ u(L) \end{bmatrix}_a = \begin{bmatrix} f(0) \\ f(L) \end{bmatrix}_e - \frac{A}{\alpha L_a} \begin{bmatrix} -1 \\ 1 \end{bmatrix} V. \quad (2.87)$$

Let's define the well-known FEM mass matrix  $\mathbf{M}^e$ , and the PZT stiffness matrix  $\mathbf{K}_p^e$  as

$$\mathbf{M}^e = \frac{mL_e}{6} \begin{bmatrix} 2 & 1 \\ 1 & 2 \end{bmatrix}, \quad \mathbf{K}_p^e = \left( Y + \frac{e^2}{\alpha} \right) \frac{A}{L_e} \begin{bmatrix} 1 & -1 \\ -1 & 1 \end{bmatrix}.$$

Now, consider an electric open boundary condition for the sensor part of the PZT material, where  $Q$  is zero. Then, from Eq. (2.86), the equation becomes

$$\mathbf{M}^e \begin{bmatrix} \ddot{u}(0) \\ \ddot{u}(L) \end{bmatrix}_e + \mathbf{K}_p^e \begin{bmatrix} u(0) \\ u(L) \end{bmatrix}_e = \begin{bmatrix} f(0) \\ f(L) \end{bmatrix}_e. \quad (2.88)$$

While, for the actuator segment of the PZT rod, the applied voltage is defined as a function of the sensor displacement as

$$V = K_g [u(L) - u(0)]_s = K_g \begin{bmatrix} -1 & 1 \end{bmatrix} \begin{bmatrix} u(0) \\ u(L) \end{bmatrix}_s. \quad (2.89)$$

Finally, substitution in (2.87) leads to

$$\begin{aligned} \frac{mL_e}{6} \begin{bmatrix} 2 & 1 \\ 1 & 2 \end{bmatrix} \begin{bmatrix} \ddot{u}(0) \\ \ddot{u}(L) \end{bmatrix}_e + \left( Y + \frac{e^2}{\alpha} \right) \frac{A}{L_e} \begin{bmatrix} 1 & -1 \\ -1 & 1 \end{bmatrix} \begin{bmatrix} u(0) \\ u(L) \end{bmatrix}_e - \frac{e^2 A}{\alpha L_a} \begin{bmatrix} 1 & -1 \\ -1 & 1 \end{bmatrix} \begin{bmatrix} u(0) \\ u(L) \end{bmatrix}_a = \\ = \begin{bmatrix} f(0) \\ f(L) \end{bmatrix}_e - K_g \frac{A}{\alpha L_a} \begin{bmatrix} 1 & -1 \\ -1 & 1 \end{bmatrix} \begin{bmatrix} u(0) \\ u(L) \end{bmatrix}_s. \end{aligned}$$

where the feedback matrix  $\Gamma_c$  equals

$$\Gamma_c = K_g \frac{A}{\alpha L_a} \begin{bmatrix} 1 & -1 \\ -1 & 1 \end{bmatrix}.$$

Thus one can rewrite

$$\mathbf{M}^e \begin{bmatrix} \ddot{u}(0) \\ \ddot{u}(L) \end{bmatrix}_e + \mathbf{K}_p^e \begin{bmatrix} u(0) \\ u(L) \end{bmatrix}_e + \mathbf{K}_a \begin{bmatrix} u(0) \\ u(L) \end{bmatrix}_a + \mathbf{\Gamma}_c \begin{bmatrix} u(0) \\ u(L) \end{bmatrix}_s = \begin{bmatrix} f(0) \\ f(L) \end{bmatrix}_e. \quad (2.90)$$

Finally, by again assembling Eq. (2.90) and Eq. (2.88) for the whole structure, one obtains the general form of Eq. (A.3) in the Appendix, which is used to generate time response simulations of the PZT metastructure in Fig. 2.22,.

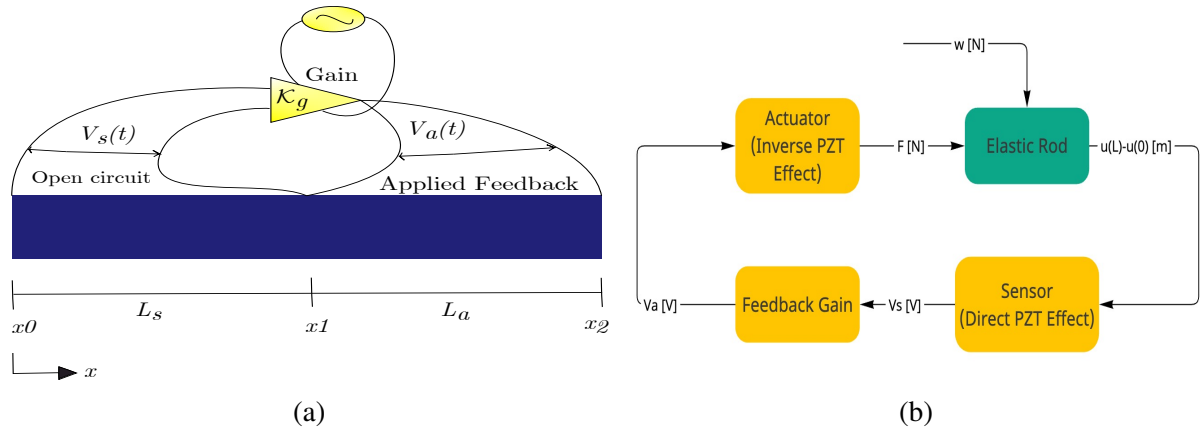


Figure 2.21 – PZT unit cell made of local feedback. The scheme in (a) shows an amplifier  $\kappa_g$  providing a feedback gain generated as a voltage at the actuator terminals ( $L_a$ ), which is proportional to the voltage at the sensor terminals ( $L_s$ ) using the PZT effects. (b) Block diagram of the system.

The FEM formulation developed in this Chapter is a powerful tool that may also be used to compute the dispersion relation. To do so, one needs to build Eq. (2.65) for the unit cell DOFs only,  $\mathbf{q}_j \in \mathbb{R}^{n_i+2 \times 1}$ , with  $f(t) = 0$  and the matrices  $\mathbf{M}_j, \mathbf{K}_j, \mathbf{R}_j \in \mathbb{R}^{n_i+2 \times n_i+2}$ , where  $n_i$  is the number of internal DOFs of the unit cell. Then, condensing one of the boundary's DOFs (Hussein *et al.*, 2014) by making a similarity transformation with  $\mathbf{V}$ ,  $\mathbf{q}_j(t) = \mathbf{V}\bar{\mathbf{q}}(t)$ , where the internal DOFs are in  $\mathbf{q}_i(t) \in \mathbb{R}^{n_i \times 1}$  and  $\bar{\mathbf{q}}(t) = [q_0(t) \quad \mathbf{q}_i(t)]^T$ :

$$\mathbf{V}^H \mathbf{M}_j \mathbf{V} \ddot{\bar{\mathbf{q}}}(t) + \mathbf{V}^H \mathbf{R}_j \mathbf{V} \dot{\bar{\mathbf{q}}}(t) + \mathbf{V}^H \mathbf{K}_j \mathbf{V} \bar{\mathbf{q}}(t) = 0, \quad \mathbf{V} = \begin{bmatrix} 1 & \mathbf{0}_{1 \times n_i} \\ \mathbf{0}_{n_i \times 1} & \mathbf{I}_{n_i} \\ e^{-i\kappa L_c} & \mathbf{0}_{1 \times n_i} \end{bmatrix}. \quad (2.91)$$

Transforming Eq. (2.91) to the frequency domain and solving the corresponding polynomial eigenvalue problem:

$$(-\bar{\mathbf{M}}_j \omega^2 + \bar{\mathbf{R}}_j i\omega + \bar{\mathbf{K}}_j) \hat{\bar{\mathbf{q}}}(\omega) = 0, \quad (2.92)$$

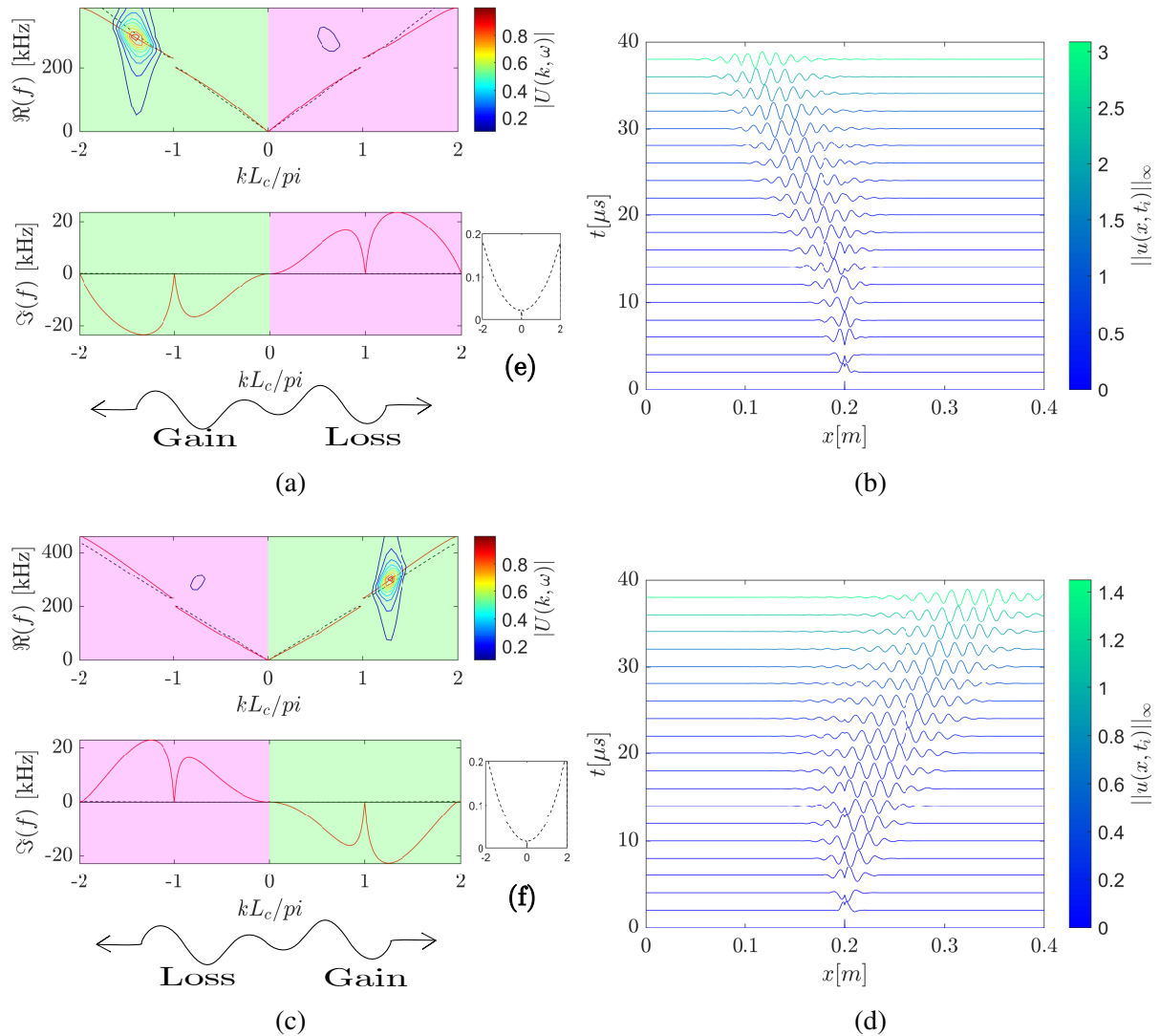


Figure 2.22 – Non-reciprocal amplification and attenuation of waves in structures with local feedback interactions ( $a = 0$ ). (a) and (c) Propagation modes of the dispersion relation for  $\kappa_g = 1.5$  and  $\kappa_g = -2$ , respectively. The First and second PBs are shown in solid red lines, superimposed to results for the equivalent passive lattice (making  $\kappa_g = 0$ ) displayed in dashed black lines. Attenuation and amplification zones are identified, respectively, by shaded magenta and green areas. (b) and (d) Transient responses to sine-burst with center frequency 300kHz illustrating the non-reciprocal wave propagation for  $\kappa_g = 1.5$  and  $\kappa_g = -2$ , respectively. Non-reciprocal wave propagation is further confirmed by their dispersion estimation through the 2D *Fourier* transform displayed as contours in (a) and (c), which are normalized by their maximum value. (e) and (f) Zoom on the imaginary dispersion diagrams to show the small and reciprocal results for damped passive lattices.

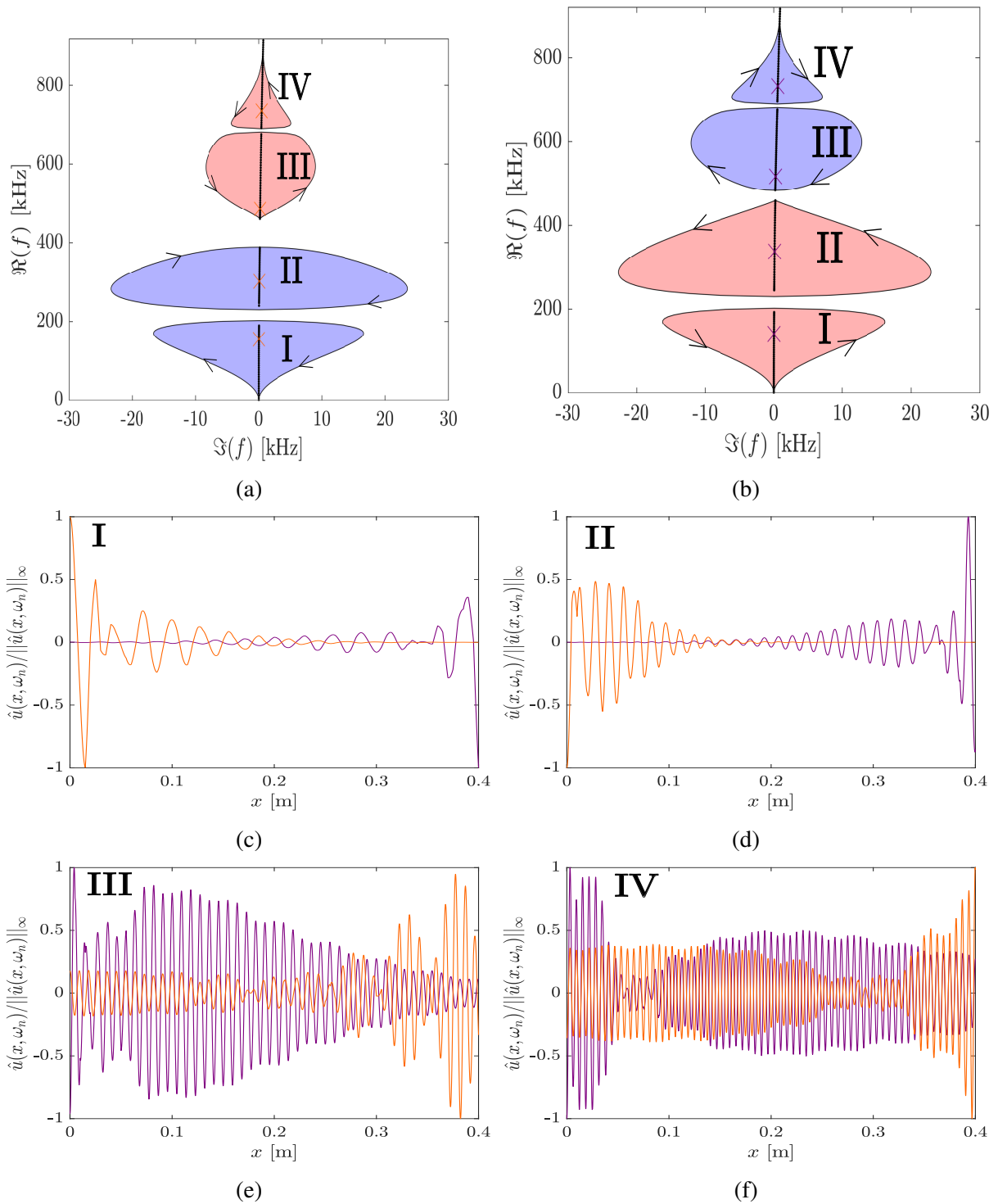


Figure 2.23 – Dispersion topology and NH skin effect with local feedback interactions ( $a = 0$ ). (a) The complex frequency plane was obtained as a projection of the dispersion relation from the first four PBs with  $\kappa_g = 1.5$ . Shaded blue and red areas represent regions with winding numbers  $\nu = -1$  and  $\nu = 1$ , respectively. (b) The same is done for negative feedback  $\kappa_g = -2$ . Eigenfrequencies of a finite structure are displayed as black dots in (a). Selected eigenmodes were shown for (c) 1PB, (d) 2PB, (e) 3PB, and (f) 4PB. Solid purple lines are used for negative feedback, whereas orange ones are used for positive feedback. The same colors mark the selected eigenfrequencies on (a) and (b).

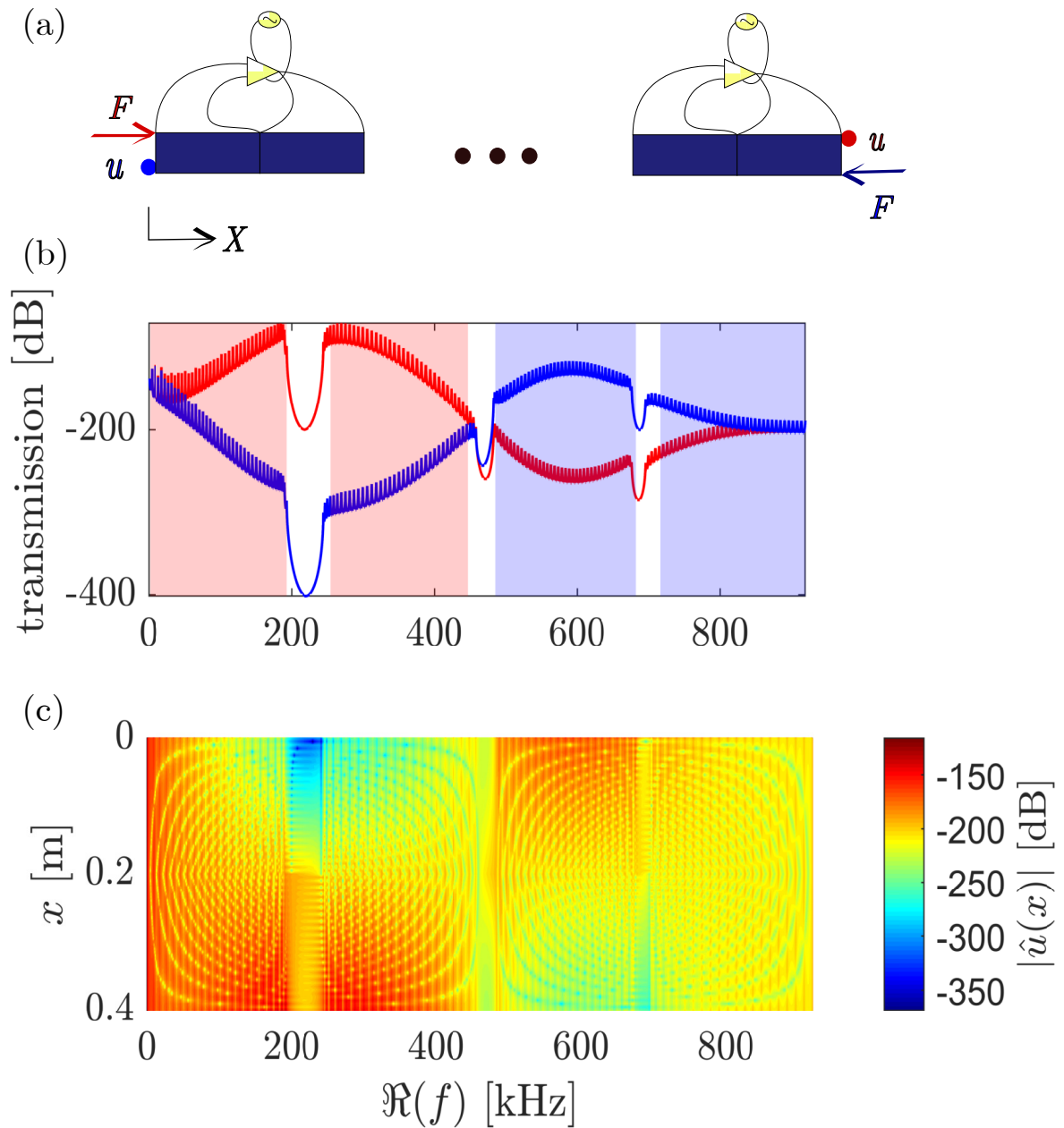


Figure 2.24 – Frequency responses of the structure in terms of displacement exhibiting energy concentration and non-reciprocal behavior - local feedback interactions. (a) The scheme of the transmission simulation is depicted in (b). (b) Results of displacement spectrum estimated at the right extremity  $|\hat{u}(L_c)|$  with left extremity excitation (red lines) and at the left extremity  $|\hat{u}(0)|$  with right extremity excitation (blue lines). (c) Two-dimensional plot of the harmonic response  $|\hat{u}(x)|$  - in dB - with excitation at the middle of the structure ( $x = 0.2\text{m}$ ).

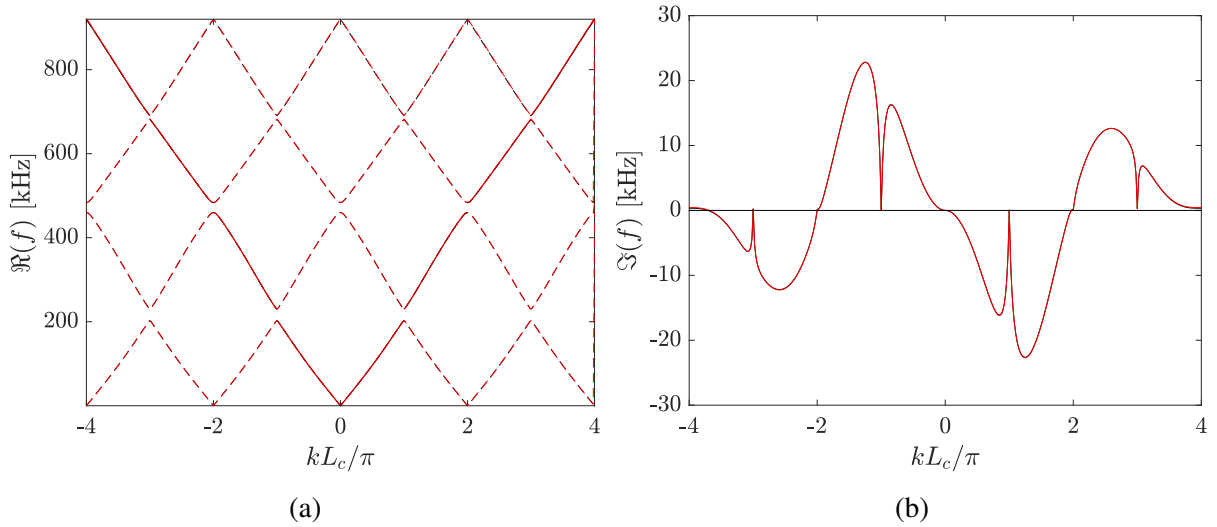


Figure 2.25 – Unfolded dispersion diagrams comparing SEM and FEM using  $\kappa_g = -2$  and  $a = 0$ . Red lines represent the FEM approximation, and black lines the SEM results.

where  $\bar{\mathbf{M}}_j = \mathbf{V}^H \mathbf{M}_j \mathbf{V}$ ,  $\bar{\mathbf{R}}_j = \mathbf{V}^H \mathbf{R}_j \mathbf{V}$ , and  $\bar{\mathbf{K}}_j = \mathbf{V}^H \mathbf{K}_j \mathbf{V}$ , for every  $\kappa$  in the desired range gives the solution  $\omega(\kappa)$ , i.e., the dispersion relation.

Aiming at comparing these mathematical models, i.e., SEM semi-analytical formulation and FEM approximation of a finite structure, simulations of the dispersion relations using both methods were performed (Braghini *et al.*, 2021). The numerical results are displayed in Fig. 2.25 for local and in Fig. 2.26 for non-local feedback interaction. Solid black lines represent SEM solutions, while solid red lines represent FEM approximate solutions. To realize asymptotically stable structural models, it is convenient to insert some source of damping. *Rayleigh's* viscous damping model was chosen for the FEM models, while in SEM models, an imaginary part of the *Young's* modulus proportional to the loss factor  $\eta$  was used as structural damping. Based on the work of (Hall, 2006), a calibration function was used so that both damping models give equivalent results.

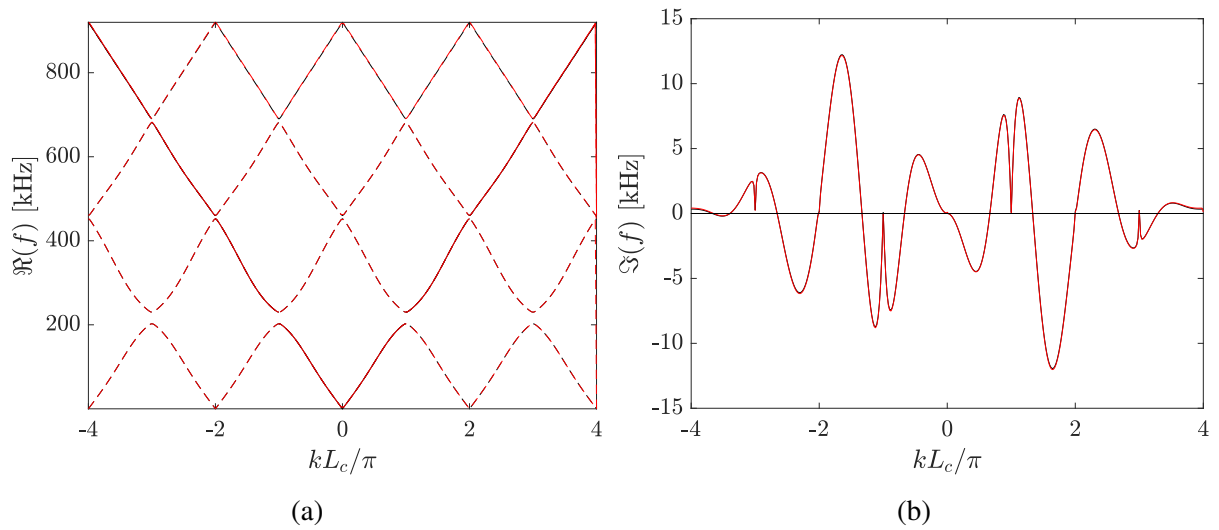


Figure 2.26 – Unfolded dispersion diagrams comparing SEM and FEM using  $\kappa_g = -0.7$  and  $a = 1$ . Red lines represent the FEM approximation, and black lines the SEM results.

### **3 STABILITY AND PERFORMANCE OF NON-RECIPROCAL NH METASTRUCTURES**

*“Measure what is measurable, and make measurable what is not.”*

*(Galileo Galilei)*

In this Chapter, a measure for non-reciprocity is defined and shown to be upper-bounded by the usual linear system norms. It can be demonstrated that maximizing these norms is equivalent to maximizing non-reciprocity; thus, any of these can be used to design the optimal solution, although some seem to be more suitable for this task.

In addition to the topological and dynamical analysis of Chapter 2, this Chapter covers the interest in optimizing performance and proving the stability of metastructures during the design process. Although only lumped-parameter systems are analyzed, by the end of the Chapter, the methodology is used together with the previous analysis to develop a general protocol for optimizing the NHSE in systems with feedback.

### 3.1 A metric for the NHSE

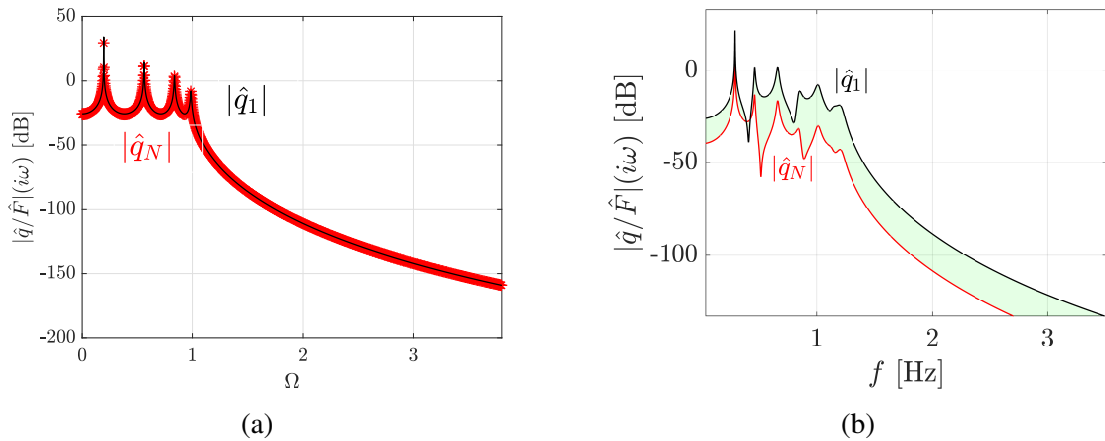


Figure 3.1 – Geometrical interpretation of performance measure  $S$ . The Frequency Response of the considered passive structure (no feedback) is displayed in (a), whereas the green area in (b) illustrates the non-zero metric  $S$  for a system with feedback;  $q_1$  is the displacement on the first mass and  $q_N$  on the  $N$ -th mass of the chain 2.2 considering a symmetric array and excitation on the central mass.

**Definition 1** (SISO system  $\Sigma$ ). Consider the following state-space representation of 2.1:

$$\dot{\mathbf{x}}(t) = \mathbf{A}\mathbf{x}(t) + \mathbf{B}w(t) \quad (3.1)$$

$$z(t) = \mathbf{C}\mathbf{x}(t) \quad (3.2)$$

, where  $\mathbf{x}(t) = \begin{bmatrix} \mathbf{q}(t) \\ \dot{\mathbf{q}}(t) \end{bmatrix} \in \mathbb{R}^{2N \times 1}$ , and  $\mathbf{A} = \begin{bmatrix} \mathbf{0}_N & \mathbf{I}_N \\ -\mathbf{M}^{-1}\mathbf{K}_g & -\mathbf{M}^{-1}\mathbf{R}_g \end{bmatrix} \in \mathbb{R}^{2N \times 2N}$ . Additionally, consider a disturbance  $w(t) \in \mathbb{R}$  in the central mass, and the output  $z(t) \in \mathbb{R}$  as the relative displacement between the first and last masses. Thus,  $\mathbf{B} = [0 \ \dots \ 1 \ \dots \ 0]^T$ , and  $\mathbf{C} = [-1 \ 0 \ \dots \ 0 \ 1]$  defines a single-input-single-output system  $\Sigma$ .

As a first attempt to systematically measure the NHSE, the frequency response of the flexible structure is used rather than the time response. The NHSE causes the forced harmonic response of the structure to exhibit non-reciprocity in terms of energy localization, as previously observed in (Braghini *et al.*, 2021) and shown in Chapter 2. For this reason, a metric  $S$  is proposed, defined in Eq. (3.3).

**Definition 2** (System norms). *Given a SISO LTI system like the one defined above and its transfer function  $H(s)$ , the following norms are defined as:*

- $\|\Sigma\|_1 = \int_{-\infty}^{\infty} |H(j\omega)| d\omega$ ;
- $\|\Sigma\|_2 = \left( \frac{1}{2\pi} \int_{-\infty}^{\infty} \text{trace}(H(j\omega)^* H(j\omega)) d\omega \right)^{1/2}$ ;
- $\|\Sigma\|_{\infty} = \sup_{\omega \in \mathbb{R}} \sigma_{\max}(H(j\omega))$ ;

**Definition 3** (Non-reciprocity metric  $S$ ). *Consider the Fourier transforms of the displacements of the first and last masses,  $\hat{q}_1, \hat{q}_N$ , respectively, due to an impulsive excitation on the central mass. The Non-reciprocity metric  $S$  is defined as*

$$S = \int_{-\omega_0}^{\omega_0} \left| |\hat{q}_N| - |\hat{q}_1| \right| d\omega. \quad (3.3)$$

The metric corresponds to the absolute value of the area between the curves  $|\hat{q}_1(j\omega)|$  and  $|\hat{q}_N(j\omega)|$ , the magnitude of their *Bode* plots. From now on, consider  $N = 7$ , as for the results depicted in Fig. 3.1.

A mathematical relation between this metric and some usual performance metrics of linear dynamical systems is stated in the following.

**Theorem 4.** *Consider the measure  $S$  of Definition 2 and the system  $\Sigma$  of definition 1. If  $\Sigma$  is causal and asymptotically stable, then for a given  $\omega_0 \in \mathbb{R}$ ,*

$$S \leq \sqrt{4\pi\omega_0} \|\Sigma\|_2. \quad (3.4)$$

*Proof.* Take the output  $z$  of system  $\Sigma$  as defined in definition 1. Then, its *Fourier* transform  $\hat{z} : j\mathbb{R} \rightarrow \mathbb{C}$  denoted  $\hat{z} = \mathcal{F}(z)$ , maps  $j\omega \mapsto \int_{-\infty}^{\infty} e^{-j\omega t} z(t) dt$ .

If  $z$  is the impulsive response, i.e., the zero-state response due to *Dirac's* delta  $w(t) = \delta(t)$ , it is well-known that  $\hat{z} = H(i\omega)$  as defined in 2. Assuming, additionally, that the system is causal and stable, the impulsive response must be absolutely integrable, which implies, by *Parseval's* Theorem, that  $\int_{-\infty}^{\infty} |H(j\omega)| d\omega < \infty$ ; thus it is also integrable.

From the *Cauchy-Schwartz* inequality(see, for example, Theorem 3.5 of (Walter, 1987), given  $\hat{g}(j\omega) = 1$  for  $\omega \in [-\omega_0, \omega_0]$  and  $\hat{g}(j\omega) = 0$  otherwise,

$$\int_{-\infty}^{\infty} |\hat{z}(j\omega)| |\hat{g}(j\omega)| d\omega \leq \left( \int_{-\infty}^{\infty} |\hat{z}(j\omega)| d\omega \right)^{1/2} \left( \int_{-\infty}^{\infty} |\hat{g}(j\omega)| d\omega \right)^{1/2}, \quad (3.5)$$

implying

$$\int_{-\omega_0}^{\omega_0} |\hat{z}(j\omega)| d\omega \leq \left( \int_{-\infty}^{\infty} |\hat{z}(j\omega)| d\omega \right)^{1/2} \sqrt{2\omega_0}. \quad (3.6)$$

Recalling the definition of the  $H_2$  norm and the output of  $\Sigma$

$$\int_{-\omega_0}^{\omega_0} |\hat{q}_N(j\omega) - \hat{q}_1(j\omega)| d\omega \leq \|\Sigma\|_2 \sqrt{4\pi\omega_0}. \quad (3.7)$$

Now, substituting  $a = \hat{q}_N$  and  $b = \hat{q}_1$  in Lemma 6 and using S from Eq. (3.3) yields

$$S \leq \int_{-\omega_0}^{\omega_0} |\hat{q}_N(j\omega) - \hat{q}_1(j\omega)| d\omega, \quad (3.8)$$

leading to Eq. (3.4)

□

The following two Lemmas are used to prove the next Theorems.

**Lemma 5.** *For any  $x, y \in \mathbb{C}$ , the following inequality between absolute values holds:*

$$||x| - |y|| \leq |x - y|. \quad (3.9)$$

*Proof.* On the one hand,

$$(|x| - |y|)^2 = |x|^2 - 2|x||y| + |y|^2 \leq |x|^2 - 2 \operatorname{Re}(\langle x|y \rangle) + |y|^2, \quad (3.10)$$

since the real part of the inner product  $\operatorname{Re}(\langle x|y \rangle) = |x||y|\cos(\theta) \leq |x||y|$ , where  $\theta$  is the difference between the arguments of  $x$  and  $y$ .

On the other hand, the sesquilinear property of the inner product:

$$|x + y|^2 = \langle x + y|x + y \rangle = \langle x|x \rangle + 2 \operatorname{Re}(\langle x|y \rangle) + \langle y|y \rangle,$$

implies that, by replacing  $y$  with  $-y$  and recalling the property  $\langle x|-y \rangle = -\langle x|y \rangle$ ,

$$|x - y|^2 = \langle x - y|x - y \rangle = \langle x|x \rangle - 2 \operatorname{Re}(\langle x|y \rangle) + \langle y|y \rangle \quad (3.11)$$

Combining 3.10 and 3.11, yields

$$(|x| - |y|)^2 \leq |x - y|^2.$$

Finally, by taking the square root on both sides,

$$||x| - |y|| \leq |x - y|$$

□

**Lemma 6.** *Given two functions  $a, b \in L_1(j\omega)$ , the following inequality between  $L_1$  norms holds:  $|||a||_{L_1} - ||b||_{L_1}| \leq ||a - b||_{L_1}$ .*

*Proof.* From Lemma 5, one have, for every  $\omega \in \mathbb{R}$ ,

$$||a(j\omega)| - |b(j\omega)|| \leq |a(j\omega) - b(j\omega)|.$$

Integrating both sides over  $\omega \in (-\infty, \infty)$  yields

$$\int_{-\infty}^{\infty} ||a(j\omega)| - |b(j\omega)|| d\omega \leq \int_{-\infty}^{\infty} |a(j\omega) - b(j\omega)| d\omega. \quad (3.12)$$

Recall that from the triangle inequality for integration,

$$\left| \int_{-\infty}^{\infty} |a(j\omega)| - |b(j\omega)| d\omega \right| \leq \int_{-\infty}^{\infty} ||a(j\omega)| - |b(j\omega)|| d\omega. \quad (3.13)$$

Combining 3.12 and 3.13 yields

$$\left| \int_{-\infty}^{\infty} |a(j\omega)| - |b(j\omega)| d\omega \right| \leq \int_{-\infty}^{\infty} |a(j\omega) - b(j\omega)| d\omega,$$

which, by definition, might be written as

$$|||a||_{L_1} - ||b||_{L_1}| \leq ||a - b||_{L_1}. \quad (3.14)$$

□

**Theorem 7.** *Consider the measure  $S$  of Eq. (3.3) and the system  $\Sigma$  of Eq. (3.1). If  $\Sigma$  is causal and asymptotically stable, then for a given  $\omega_0 \in \mathbb{R}$*

$$S \leq 2\omega_0 ||\Sigma||_{\infty}. \quad (3.15)$$

*Proof.* From Lemma. 5,

$$\sup_{\omega \in \mathbb{R}} \left| |\hat{q}_N(j\omega)| - |\hat{q}_1(j\omega)| \right| \leq \sup_{\omega \in \mathbb{R}} |\hat{q}_N(j\omega) - \hat{q}_1(j\omega)|. \quad (3.16)$$

Furthermore

$$\int_{-\omega_0}^{\omega_0} \left| |\hat{q}_N(j\omega)| - |\hat{q}_1(j\omega)| \right| d\omega \leq \sup_{\omega \in \mathbb{R}} \left| |\hat{q}_N(j\omega)| - |\hat{q}_1(j\omega)| \right| 2\omega_0. \quad (3.17)$$

Thus, substituting the definitions of the  $H_\infty$  norm and  $S$  leads to Eq. (3.15)  $\square$

**Theorem 8.** Consider the measure  $S$  of Definition 2 and the system  $\Sigma$  of Definition 1. If  $\Sigma$  is causal and asymptotically stable, then for a given  $\omega_0 \in \mathbb{R}$ ,

$$S \leq \|\Sigma\|_1 \quad (3.18)$$

*Proof.* The proof comes from the direct application of Lemma. 6 and the definition of  $L_1$  norm for  $\Sigma$ .  $\square$

### 3.2 Results

Fig. 3.1a shows the magnitude of the Bode plots of the passive structure (open-loop system) with  $b = 0.01$  for external force  $\hat{f}$  applied on the middle (4-th mass) and measures on the left end ( $\hat{q}_1$ ) and on the right end ( $\hat{q}_7$ ). As expected from the symmetry of the structure, both responses are equal and thus  $S = 0$ . The following subsections show that the system becomes non-reciprocal by applying the feedback, which translates into asymmetric results. As shown in previous works (Braghini *et al.*, 2021), as the distance between the two measured signals becomes more accentuated (higher values of  $S$ ), the NHSE is expected to be more visible on the time-domain response.

The closed-loop dynamic system is said to be stable if and only if all of its poles have strictly negative real parts. In other words, the maximum real part of the poles,  $\text{Re}(\lambda)_{max}$  must be negative. In practice, however, small uncertainties in the system parameters may lead to variations on the poles. Thus, for robustness purposes, it is desirable that the poles stay as far as possible from the imaginary axis; as simulations show, this happens only for gains  $g \in I = (g_0, g_1)$ . For these values, tables 3.1, 3.2, 3.3 show the maximum value of the metric  $S$  that can be achieved with each feedback strategy; these values are achieved with feedback gains  $g_S \in I$ .

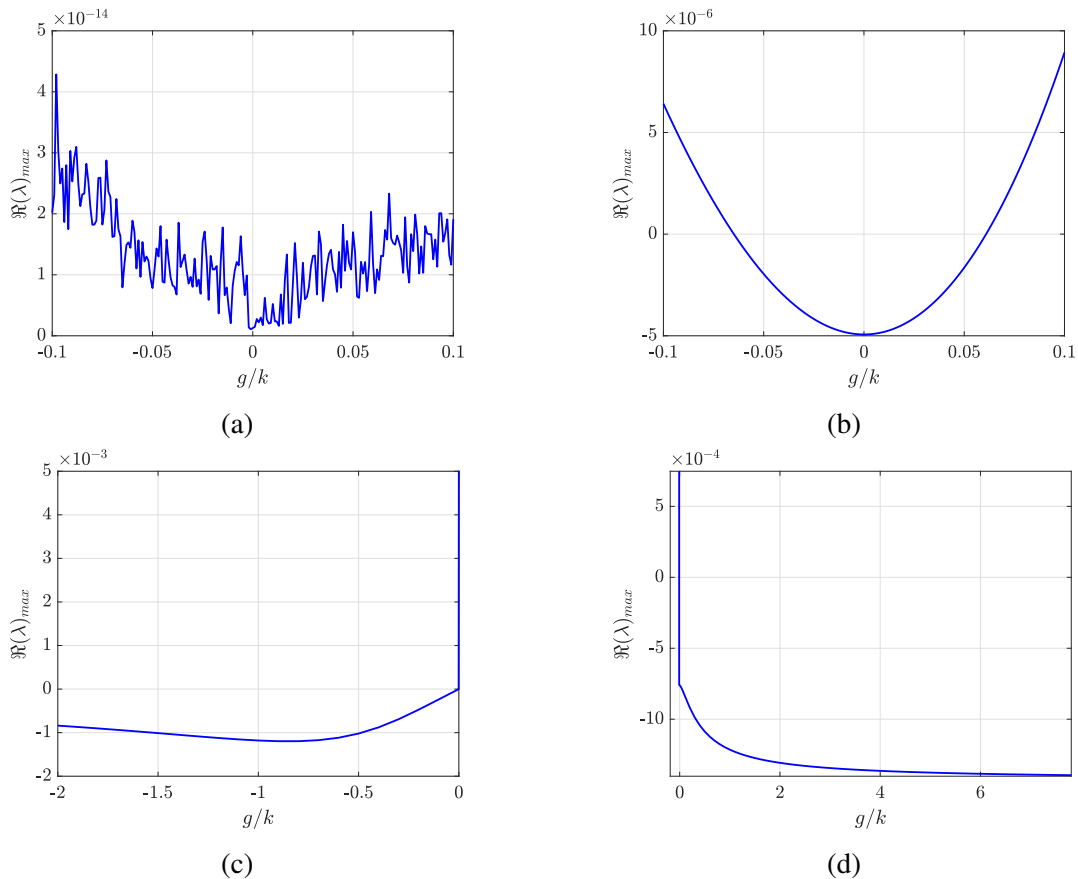


Figure 3.2 – Stability margins for damped and undamped systems, with feedback or not. The maximum real part of the eigenvalues is displayed against feedback gain for undamped systems in (a), with proportional feedback for  $b = 0.01$  in (b), for undamped derivative feedback in (c), and damped double derivative feedback with  $b = 0.01$  in (d).

Fig. 3.2 highlights the fact that, without any damping, proportional feedback leads to unstable structures for any feedback gain, whereas the inclusion of damping makes  $I \neq \emptyset$ . However, under derivative feedback, even the undamped systems are stable for any negative feedback gain. Conversely, using double derivative feedback, damped systems are stable for any positive feedback gain.

### 3.2.1 Proportional Feedback.

Table 3.1 shows that the interval  $I$  increases slightly with increases in damping, whereas  $S$  decreases. This result implies that, even though the addition of enough viscous damping stabilizes the system, it kills the non-reciprocal effect. Moreover,  $S$  assumes higher values on the instability limits, which can be noted by the  $\text{Re}(\lambda)_{max}$  values. These results can be better visualized in the plots of Fig. 3.3, varying the damping factor as in the table. Furthermore,

Fig. 3.8 (a) emphasizes the non-reciprocal behavior in the frequency response, (d) shows how  $I$  increases as damping is added to the structure, and (g) illustrates that the system norms exhibit similar behavior as  $S$  with varying values of feedback gain  $\gamma$ . Moreover, in accordance with 3.2, the undamped structure ( $b = 0$ ) has all eigenvalues on the imaginary axis, and thus  $I_{b=0} = \emptyset$ .

Next, Fig. 3.4 shows the root locus of the closed-loop system, i.e., how the poles of the closed-loop system evolve with varying feedback gain values for the fixed damping value  $b = 0.01$ . The results show that for both positive and negative feedback, there is a small range of values for which all the eigenvalues remain on the left half-plane, guaranteeing asymptotic stability.

By varying damping, the distance from  $\text{Re}(\lambda)_{max}$  varies as in Fig. 3.8 (g), reaching maximum values for  $g \in (-30, -20)$ ; it can also be seen how  $I$  increases with  $b$ .

Table 3.1 – Proportional feedback from  $-10$  to  $10$  with precision  $10^{-4}$

b	$\gamma_0$	$\gamma_1$	$\max S$	$\gamma_S$	$\text{Re}(\lambda)_{max} (g = g_S)$
0	$\#$	$\#$	$\#$	$\#$	$\#$
0.01	-3.246	5.38	13.91	-3.245	-0.0001
0.05	-3.308	5.58	12.01	-3.307	-0.0001
0.08	-3.314	5.60	10.42	-3.313	-0.0001
0.1	-3.317	5.60	11.00	-3.316	-0.0001
0.12	-3.319	5.61	9.78	-3.317	-0.0001
0.15	-3.321	5.61	9.61	-3.320	-0.0001
0.2	-3.324	5.62	9.07	-3.322	-0.0001
0.3	-3.332	5.63	8.26	-3.331	-0.0001
0.4	-3.341	5.64	7.88	-3.339	-0.0001
0.5	-3.352	5.65	7.72	-3.350	-0.0002
0.6	-3.366	5.66	7.14	-3.365	-0.0001
0.7	-3.381	5.67	6.80	-3.379	-0.0001
0.8	-3.398	5.69	6.80	-3.396	-0.0002
0.9	-3.417	5.71	6.40	-3.415	-0.0002
1	-3.438	5.73	7.00	-3.437	-0.0001
1.5	-3.554	5.86	5.47	-3.553	-0.0003
2	-3.672	6.03	5.23	-3.670	-0.0001

### 3.2.2 Derivative Feedback

Table 3.2 shows, in accordance with Fig. 3.2, that derivative feedback results in an asymptotically stable metastructure for any negative feedback gain. Furthermore, even the undamped system is asymptotically stable in this case.

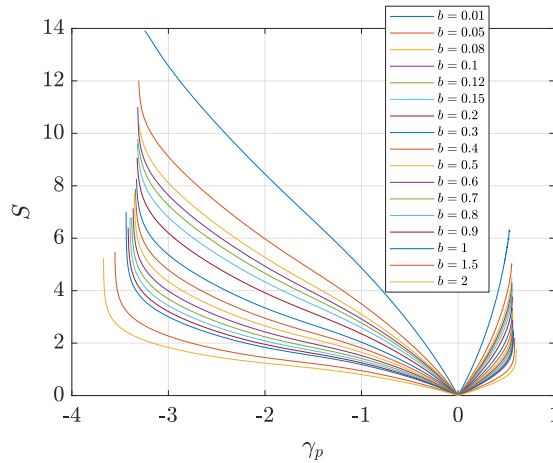


Figure 3.3 – Performance against proportional feedback gain depending on damping. The damping factor  $b$  varies as in Table 3.1.

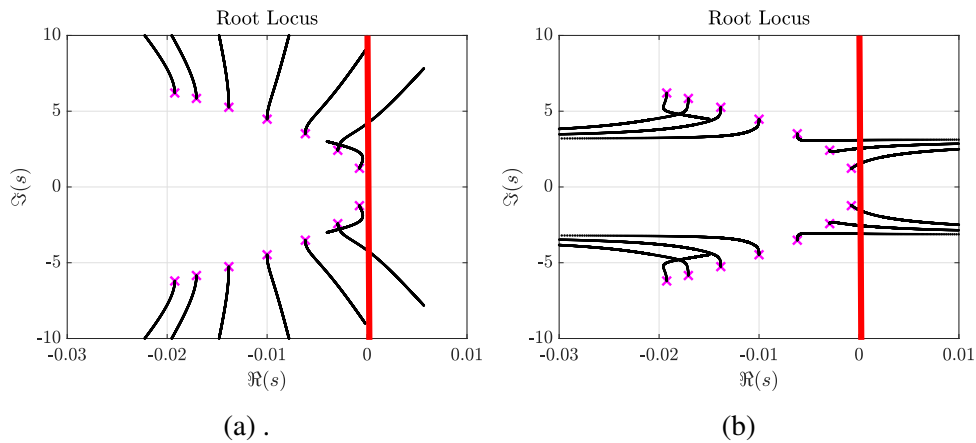


Figure 3.4 – Root locus plot for the structure with  $b = 0.01$  and proportional feedback. Results are shown for  $g < 0$  in (a) and  $g > 0$  in (b). Magenta  $x$  denotes the poles of the open loop structure, and the red line highlights the stability limit, intersecting the open left and right half-planes.

$S$  almost don't vary with the damping factor and, on Fig. 3.8 (b), the performance of the structure as a function of the feedback gain shows a very different behavior compared to the proportional feedback case; now both  $S$  and the system norms have a maximum value in  $I$ , although assuming considerably lower values. The value of  $S$  approaches a limit of  $\approx 0.10$  as  $g$  increases negatively. Even for such a small value, considerable non-reciprocal effects can still be observed on the metastructure's frequency responses, as shown in Fig. 3.5.

Regarding the stability,  $\text{Re}(\lambda)_{max}$  is considerably further away from the imaginary axis than the proportional feedback case. Fig. 3.6 shows the root locus of the closed loop structure with negative feedback. The eigenvalues remain on the left half-plane; the opposite occurs with positive feedback. Furthermore, Fig. 3.2 (c) shows that there is also a maximum distance from the imaginary axis for values of  $\gamma_d$  pretty close to the one which maximizes  $S$  and

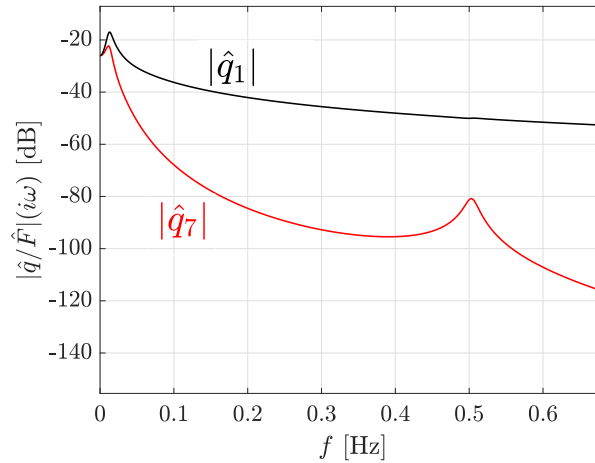


Figure 3.5 – Frequency response of the structure with derivative feedback and  $\gamma_d = -10$ .

also approaches a limiting negative value  $\approx -0.001$ . Increasing  $b$  also increases considerably the value of  $\text{Re}(\lambda)_{max}$  as shown in Fig. 3.8 (e), although table 3.2 and Fig. 3.8 (h) depicts how non-reciprocity decreases with damping.

Table 3.2 – Derivative feedback varying  $\gamma_d$  from  $-10$  to  $10$  with precision  $10^{-2}$ .

$b$	$\gamma_0$	$\gamma_1$	max S	$\gamma_S$	$\text{Re}(\lambda)_{max} (g_d = g_S)$
0	-10	0.00	0.34	-1.09	-0.16
0.01	-10	0.00	0.34	-1.09	-0.16
0.05	-10	0.01	0.34	-1.09	-0.16
0.08	-10	0.02	0.34	-1.09	-0.16
0.1	-10	0.02	0.34	-1.09	-0.16
0.12	-10	0.02	0.34	-1.09	-0.16
0.15	-10	0.03	0.34	-1.09	-0.16
0.2	-10	0.04	0.34	-1.08	-0.17
0.3	-10	0.06	0.34	-1.08	-0.17
0.4	-10	0.08	0.33	-1.08	-0.17
0.5	-10	0.10	0.33	-1.08	-0.18
0.6	-10	0.12	0.33	-1.08	-0.18
0.7	-10	0.14	0.33	-1.08	-0.18
0.8	-10	0.16	0.33	-1.08	-0.19
0.9	-10	0.18	0.33	-1.08	-0.19
1	-10	0.20	0.33	-1.08	-0.19
1.5	-10	0.30	0.32	-1.10	-0.21
2	-10	0.40	0.31	-1.13	-0.22

### 3.2.3 Double Derivative feedback

Table 3.2 shows that the double derivative feedback results in an asymptotically stable metastructure for any positive feedback gain.

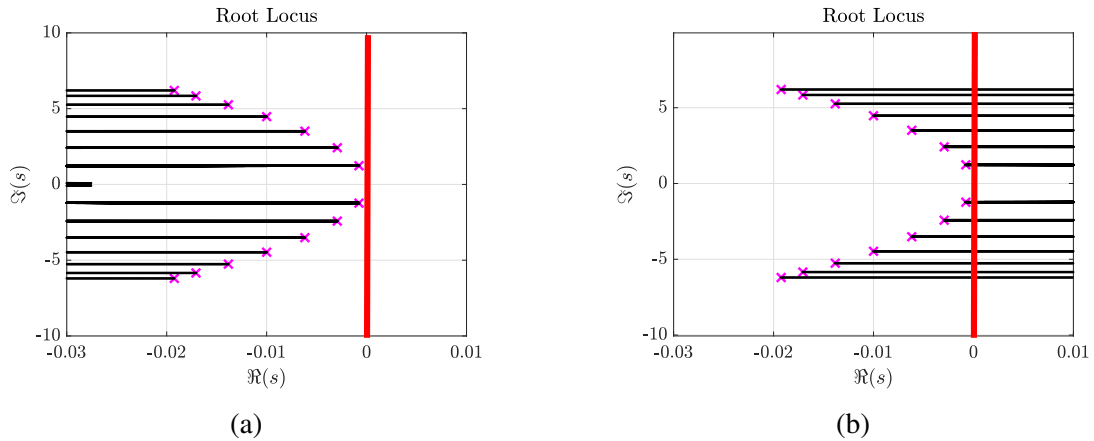


Figure 3.6 – Root locus plot for the structure with  $b = 0.01$  and derivative feedback. Results are shown for  $g < 0$  in (a) and  $g > 0$  in (b). Magenta  $x$  denotes the poles of the open loop structure, and the red line highlights the stability limit, intersecting the open left and right half-planes.

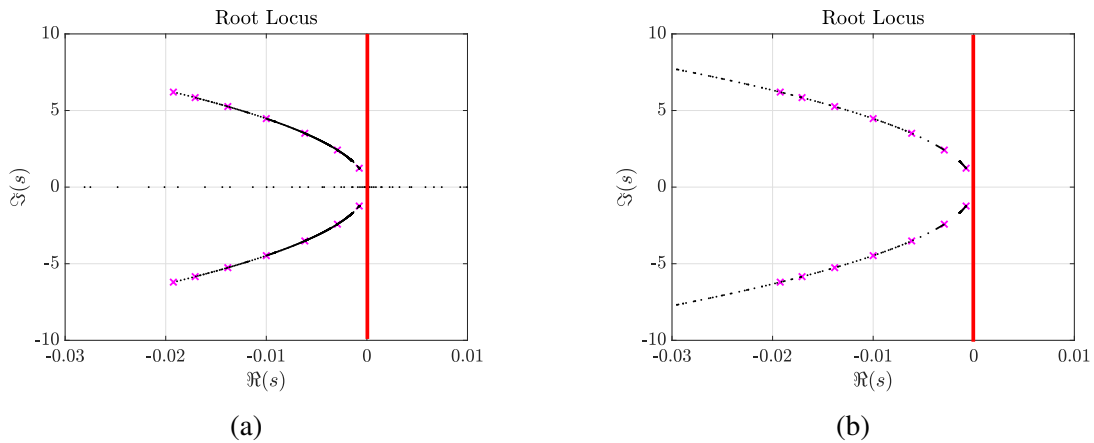


Figure 3.7 – Root locus plot for the structure with  $b = 0.01$  and double derivative feedback. Results are shown for  $g < 0$  in (a) and  $g > 0$  in (b). Magenta  $x$  denotes the poles of the open loop structure, and the red line highlights the stability limit, intersecting the open left and right half-planes.

$S$  decreases with the damping factor but assumes values similar to those in the proportional feedback case, which are higher than in the derivative case. Furthermore, in Fig. 3.8 (c), the performance of the structure as a function of the feedback gain shows both  $S$  and the system norms increase indefinitely with  $g$ , as illustrated by the *Bode* plot in (f).

Concerning stability, illustrates that  $\text{Re}(\lambda)_{max}$  is much closer to the imaginary axis for low values of damping, similar to the other feedback cases. Moreover, Fig. 3.7 shows that in the root locus of the closed loop structure with positive feedback, the eigenvalues remain on the left half-plane, which is the opposite behavior of the single derivative feedback case. Again, increasing  $b$  also increases considerably the value of  $\text{Re}(\lambda)_{max}$ , as depicted in Fig. 3.8 (f), although table 3.3 and Fig. 3.8 (i) show how  $S$  and the system norms drop with this change.

Table 3.3 – Double Derivative feedback varying  $\gamma_{dd}$  from  $-10$  to  $10$  with precision  $10^{-2}$ .

b	$\gamma_0$	$\gamma_1$	$\max S$	$\gamma_S$	$\text{Re}(\lambda)_{\max} \quad (g = g_S)$
0	#	#	#	#	#
0.01	-0.13	10.00	52.11	10.00	0.00
0.05	-0.15	10.00	25.08	10.00	0.01
0.08	-0.16	10.00	18.76	10.00	-0.01
0.1	-0.16	10.00	16.20	10.00	-0.01
0.12	-0.17	10.00	14.31	10.00	-0.02
0.15	-0.17	10.00	12.21	10.00	-0.02
0.2	-0.18	10.00	9.82	10.00	-0.03
0.3	-0.21	10.00	7.01	10.00	-0.04
0.4	-0.22	10.00	5.40	10.00	-0.06
0.5	-0.24	10.00	4.35	10.00	-0.07
0.6	-0.26	10.00	3.63	10.00	-0.08
0.7	-0.27	10.00	3.10	10.00	-0.10
0.8	-0.29	10.00	2.70	10.00	-0.11
0.9	-0.30	10.00	2.39	10.00	-0.13
1	-0.31	10.00	2.14	10.00	-0.14
1.5	-0.37	10.00	1.41	10.00	-0.21
2	-0.43	10.00	1.05	10.00	-0.27

It was shown in (Rosa; Ruzzene, 2020) that OBCs of any kind can be used to observe the NHSE. Another interesting question is whether the kind of restriction in the boundaries has an influence on the stability results. Fig. 3.9 shows the root locus for free-free boundaries in (a) and fixed-fixed in (c) for gains from  $-\infty$  to  $\infty$ , from where considerable change in stability is observed. Additionally, by wrapping around the structure (connecting the first and last masses) to emulate PBCs, the resultant root locus is depicted in (e), and the corresponding maximum real part of the eigenvalues for varying values of feedback gain in (b), (d), and (f).

Where free-free boundaries are imposed, a pole in the origin is always present, and  $I$  is shown to be a smaller interval in comparison with fixed boundaries. The wrap-around structures also exhibit this pole, and, in that case,  $I$  is even smaller.

Figure 3.10 shows the effect of increasing the number of masses  $N$  in the structure: for both boundary conditions, the system's poles approach the imaginary axis and eventually cross it, making the structure unstable, as  $N$  increases.

In summary, from the previous results, the derivative feedback is shown to have a stabilizable effect similar to the addition of damping. Thus, one can use it together with proportional feedback, for example. By adapting the periodically applied feedback law described

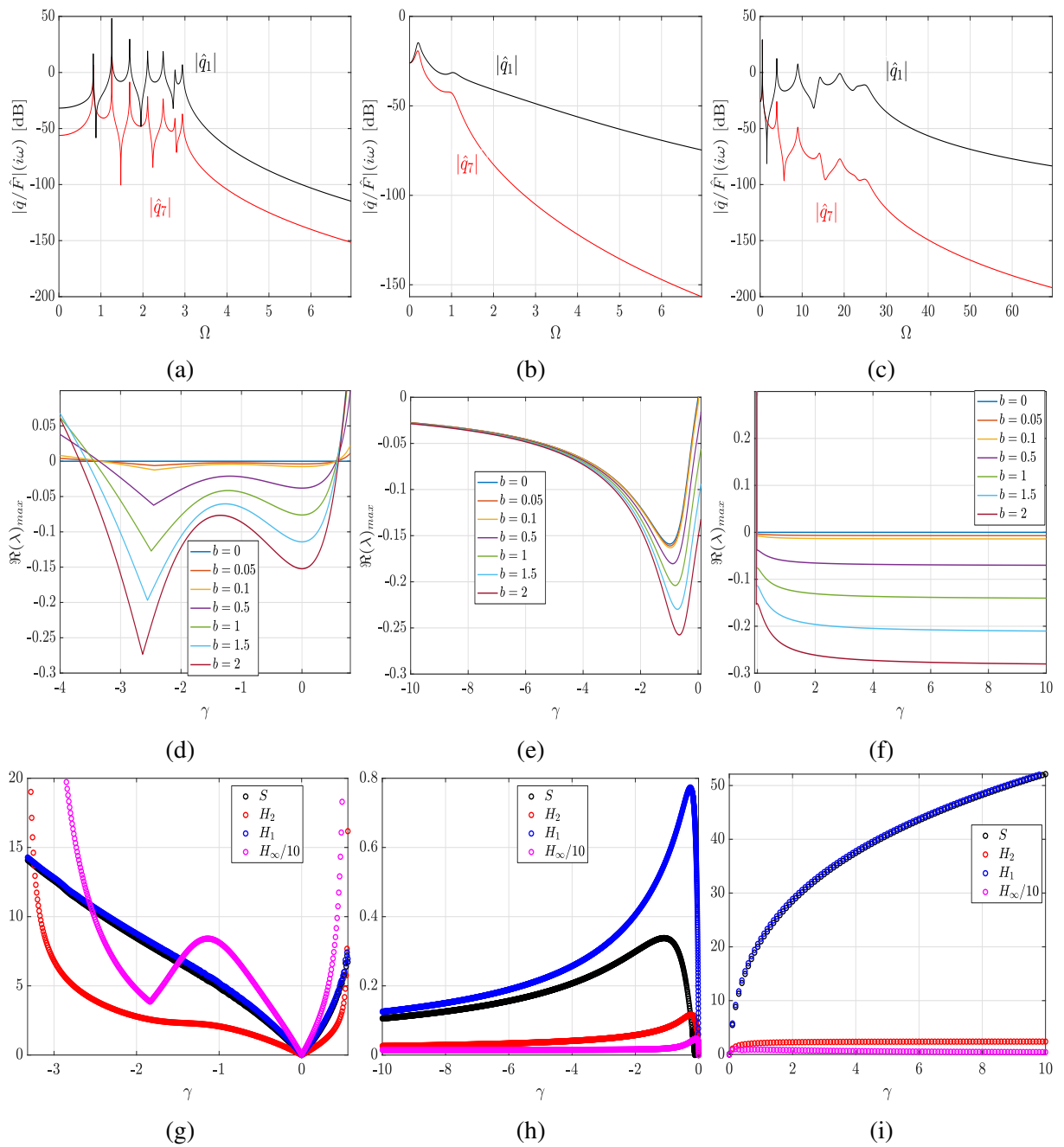


Figure 3.8 – Stability and performance results by varying the feedback gain and damping factor. Frequency responses of stable structures ( $b = 0.01$ ) with (a) proportional feedback with  $\gamma = -3$ , (b) derivative feedback with  $\gamma = -1.1$ , and (c) double derivative feedback with  $\gamma = 10$ . Stability margins under purely (d) proportional feedback, (e) derivative feedback, and (f) double derivative feedback, varying  $\gamma$  for increasing values of  $b$ . Performance under purely (g) proportional feedback, (h) derivative feedback, and (i) double derivative feedback with fixed  $b = 0.01$  and varying  $\gamma$  within the stability range.

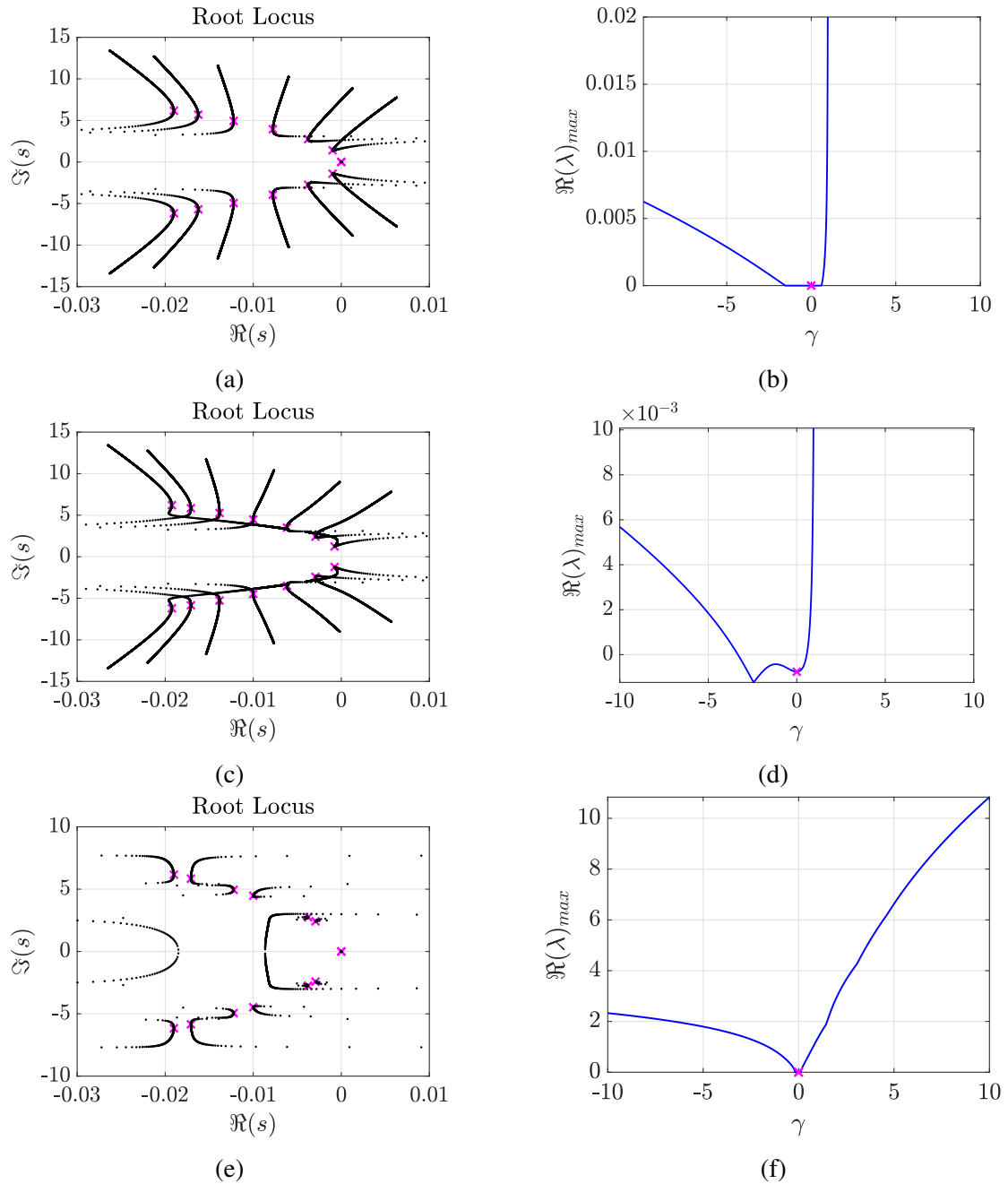


Figure 3.9 – Stability under proportional feedback gain for different boundary conditions. In (a), (c), and (e) the root locus under proportional feedback gain varying from  $\gamma_p = -10$  to 10 is shown considering free-free, fixed-fixed, and wrap-around boundary conditions, respectively, and fixed values of  $b = 0.01$  and  $N = 7$ . (b), (d), and (f) show the corresponding maximum real part of the eigenvalues of the system.

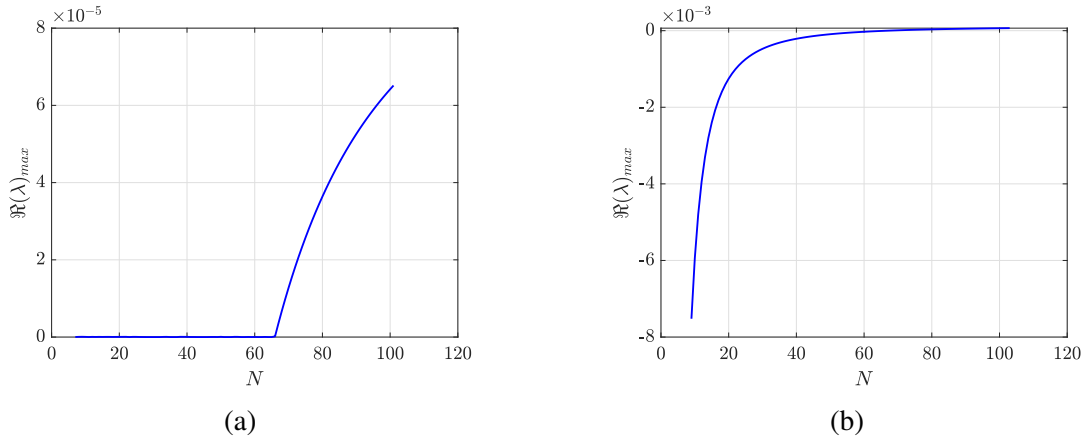


Figure 3.10 – Maximum real part of the eigenvalues of the NH system under proportional feedback by varying the number of masses. The maximum real part of the eigenvalues of the NH system is depicted for fixed parameters  $\gamma_p = -0.1$ .

in Chapter 2 as the following:

$$u_i(t) = g_p(q_{i+1}(t) - q_i(t)) + g_d(\dot{q}_{i+1}(t) - \dot{q}_i(t)) = \begin{bmatrix} g_p & g_d \end{bmatrix} \begin{bmatrix} q_{i+1}(t) - q_i(t) \\ \dot{q}_{i+1}(t) - \dot{q}_i(t) \end{bmatrix},$$

the output equation is given as, following the same procedure done to obtain Eq. (2.6), Eq. (2.7), and Eq. (2.8),

$$\mathbf{y}(t) = \begin{bmatrix} \mathbf{Y} & \mathbf{0}_{N-1 \times N} \\ \mathbf{0}_{N-1 \times N} & \mathbf{Y} \end{bmatrix} \mathbf{x}(t), \quad (3.19)$$

and thus

$$\mathbf{u} = \begin{bmatrix} g_p \mathbf{I}_{N-1} & g_d \mathbf{I}_{N-1} \end{bmatrix} \begin{bmatrix} \mathbf{Y} & \mathbf{0}_{N-1 \times N} \\ \mathbf{0}_{N-1 \times N} & \mathbf{Y} \end{bmatrix} \mathbf{x}(t) = \begin{bmatrix} g_p \mathbf{Y} & g_d \mathbf{Y} \end{bmatrix} \mathbf{x}(t).$$

The PD strategy is shown to increase performance and obtain stable undamped systems. Fig. 3.11 (a) shows that the system remains stable for negative derivative gains and a wide range of proportional gains. On the other hand, (b), (c), (d), and (e) depict the influence of both gains on the performance of the undamped NH system, leading to the conclusion that all the performance measures proposed herein behave similarly and thus can equally be used to choose an optimal gain ( $g_p, g_d$ ) for these cases. Notably, the  $H_1$  norm is the closest system norm to the measure  $S$ , which should be maximized.

Regarding distributed-parameter systems like the acoustic example used in Chapter 2, the standard approach consists in using the FEM to model it as a finite-dimensional system. This method was described in Chapter 2 and in Appendix A. Fig. 3.12 shows how interval

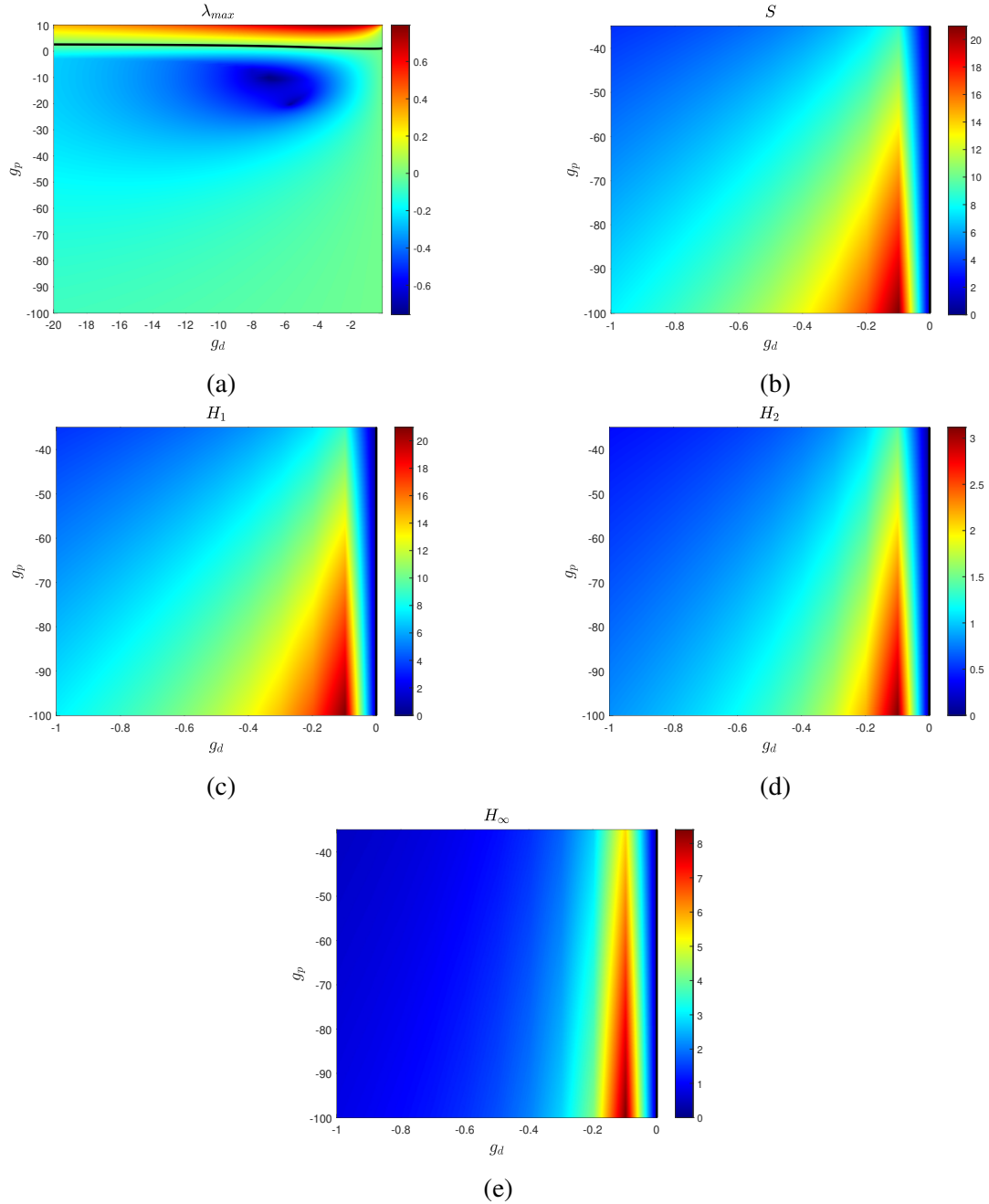


Figure 3.11 – Performance of undamped ( $b = 0$ ) NH system under proportional and derivative feedback as a function of parameters  $g_p$  and  $g_d$ . (a) Shows the maximum real part of the eigenvalues with a black line indicating the stability limit point  $\lambda_{max} = \max_j(\text{Re}(\lambda_j)) = 0$ . (b) shows the measure  $S$  compared with  $H_1$ ,  $H_2$ , and  $H_\infty$  norms as defined in this Chapter, represented in (c), (d), and (e), respectively.

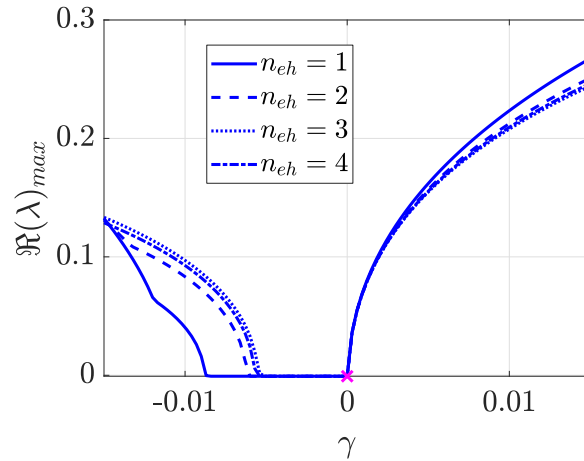


Figure 3.12 – Stability margin of the acoustic NH system by varying  $\gamma$  computed with a different number of finite elements. The *spill-over* effect may be inferred.

$I$  varies depending on the grid.  $n_{eh}$  is the number of finite elements in each homogeneous segment of each unit cell. The apparently converging interval may explain the bounded solution observed in Chapter 2, Fig. 2.16. However, the different results indicate how the *spill-over* effect (Zhao *et al.*, 1978; Eshraqi *et al.*, 2016) interfere in the analysis of a distributed-parameter system. To prove the stability of this kind of system and design optimal feedback laws, integration with the theory introduced in Appendix B may be necessary and is recommended for future works.

## 4 CONCLUDING REMARKS AND OUTLOOKS

*“The problems are solved, not by giving new information, but by arranging what we have known since long.”*  
*(Ludwig Wittgenstein)*

In this chapter, the results and contributions of this work are summarized, and suggestions for future works are presented. The resultant publications are also listed.

## 4.1 Summary

Chapter 1 introduces the key concepts used in this work with numerical examples. Specifically, mechanical Non-Hermitian metamaterials and the topological mode called NHSE are introduced in the context of recent developments in the fields known as phononics and topological metamaterials, tracing back to early studies in periodic systems.

In Chapter 2, the NHSE is observed by simulations using different models, although not exhaustively, which are divided into lumped-parameter and distributed-parameter systems. Single-band lumped-parameter systems are the simplest platforms to study this phenomenon, which can be done by computing analytical dispersion diagrams derived by hand. Moreover, a state-space framework detailed in Appendix A is used to compute the time responses of finite structures under transient tone-burst kind excitations. The same procedure is extended – by numerical methods – to systems with band-gap in the dispersion diagrams and generally non-local feedback gains in the considered laws: proportional, derivative, and double derivative.

The second part of Chapter 2 focuses on distributed-parameter systems. Two NH models are derived: acoustic and piezoelectric waveguides with feedback. Then, the analysis done in the lumped-parameter systems is repeated for these examples with the methods developed in Appendix A. Particularly, the acoustic model is chosen to build an experimental platform envisioned in Appendix C and further detailed in ANNEX A.

Finally, in Chapter 3, a general protocol is introduced aiming to optimize the non-reciprocity of structures exhibiting NHSE in one-dimensional systems considering the different kinds of non-reciprocal periodic feedback interactions presented in the previous chapter with varying numbers of unit cells in the structures. Furthermore, the effects of viscous damping and different boundary conditions on stability and performance are also considered.

For the distributed-parameter systems, an possible ad-hoc solution of adding filters to the feedback law is preliminarily investigated. It is shown that for non-ideal filters this solution is far from optimum, since it degenerates the topology resulting in a considerably lower performance in terms of  $S$ . Regarding this problem, Appendix B summarizes methods of analysis and control based on the extensive PIEs literature.

The main contributions of this work can be stated as follows:

- expands results of the NHSE to lumped-parameter and distributed-parameter systems subjected to different local and non-local feedback laws;
- introduces an investigation on the stability and performance of topological metamaterial in the context of the NHSE;
- shows the trade-off between stability and performance by adding viscous damping or derivative feedback;
- proposes an experimental setup to study the dynamics resultant from the NHSE and the control of the proposed system;

## 4.2 Outlooks

The following directions would lead to what, in the particular view of the authors, are interesting contributions to the field, rounding this work off:

- realize the proposed experiment on an electroacoustic platform using both analog and digital control implementations;
- work on the inverse problem of designing an optimized topological metastructure, which maximizes both  $\text{Re}(\lambda)_{max}$  and the metric  $S$  for guaranteed stability and performance;
- expand the stability analysis and design protocol to distributed-parameter systems using both early-lumping (FEM based) and no-lumping (PIEs) approaches.

## 4.3 List of Publications

Papers published in journals:

- Braghini, D.; Villani, L. G. G.; Rosa, M. I. N.; Arruda, J. R. F. Non-hermitian elastic waveguides with piezoelectric feedback actuation: non-reciprocal bands and skin modes. *Journal of Physics D: Applied Physics*, v. 54, n. 28, p. 285302, 2021

Full papers and abstracts published in conference proceedings:

- BRAGHINI, D.; Camino, J. F.; ARRUDA, J. R. F. Stability and Performance Analysis of Active Topological Non-Hermitian Metastructures. In: XLIV Ibero-Latin-American

Congress on Computational Methods in Engineering, 2023, Porto. Proceedings CIL-AMCE - PANACM 2023. Porto: ABMEC, 2023. v. 1. p. 1-9.

- Ribeiro, L.H.M.S., Braghini, D., Beli, D., Arruda, J. R.F.. “Computing dispersion relations with modal analysis methods”. proceedings of Noise and Vibration: Emerging Methods (NOVEM2023), Auckland, New Zeland, 2023.
- Braghini, D.; Peet, M. M. Computing optimal upper bounds on the h2-norm of ode-pde systems using linear partial inequalities. IFAC-PapersOnLine, v. 56, n. 2, p. 6994–6999, 2023.
- RIBEIRO, L. H. M. S. ; BRAGHINI, D. ; LIMA, V. D. ; ARRUDA, JOSE ROBERTO F . Design and test of a periodic NBR-steel frame structure considering manufacturing variability. In: ISMA 2022 - International Conference on Noise and Vibration Engineering, 2022, Leuven. Proceedings of ISMA 2022, 2022.
- BRAGHINI, D.; AM Goto ; NORA ROSA, MATHEUS INGUAGGIATO ; ARRUDA, J. R. F. . Non-Hermitian Acoustic Metamaterials with Periodically Distributed Electroacoustic Feedback. In: 19-th U.S. National Congress of Theoretical and Applied Mechanics, 2022, Austin, TX. Book of Abstracts, 2022. v. 1. p. 71-71. (Abstract only)
- BRAGHINI, D.; VILLANI, LUIS GUSTAVO GIACON ; NORA ROSA, MATHEUS INGUAGGIATO ; ARRUDA, JOSE ROBERTO F . Non-Hermitian Waveguides With Periodic Feedback. In: XLII Ibero-Latin-American Congress on Computational Methods in Engineering, 2021, Rio de Janeiro. Proceedings CILAMCE - PANACM 2021. Rio de Janeiro: ABMEC, 2021. v. 1. p. 1-9.

#### Preprint papers:

- Braghini, D.; Lima, V. D. de; Beli, D.; Rosa, M. I.; Arruda, J. R. d. F. Non-hermitian acoustic waveguides with periodic electroacoustic feedback. arXiv preprint arXiv:2210.05948, 2022

#### Technical manuals

- Shivakumar, S.; Jagt, Braghini, D.; Das, A.; Peet, M. PIETOOLS 2022: User manual. arXiv, 2022.

## REFERENCES

- Assis, G. F. C. A.; Beli, D.; de Miranda Jr., E. J. P.; Camino, J. F.; Dos Santos, J. M. C.; Arruda, J. R. F. Computing the complex wave and dynamic behavior of one-dimensional phononic systems using a state-space formulation. **International Journal of Mechanical Sciences**, v. 163, p. 105088, 2019.
- Atalla, N.; Sgard, F. **Finite element and boundary methods in structural acoustics and vibration**. [S.l.]: CRC Press, 2015.
- Batra, N.; Sheet, G. Physics with coffee and doughnuts: Understanding the physics behind topological insulators through su-schrieffer-heeger model. **Resonance**, v. 25, n. 6, p. 765–786, 2020.
- Beli, D. *et al.* **Vibration attenuation and elastic wave manipulation in periodic structures using band gaps and nonreciprocity**. Tese (Doutorado) — Universidade Estadual de Campinas (UNICAMP). Faculdade de Engenharia Mecânica, 2018.
- Bergholtz, E. J.; Budich, J. C.; Kunst, F. K. Exceptional topology of Non-Hermitian systems. **Reviews of Modern Physics**, v. 93, n. 1, p. 015005, 2021.
- Bertoldi, K.; Vitelli, V.; Christensen, J.; Van Hecke, M. Flexible mechanical metamaterials. **Nature Reviews Materials**, v. 2, n. 11, p. 1–11, 2017.
- Bloch, F. Über die quantenmechanik der elektronen in kristallgittern. **Zeitschrift Für Physik**, v. 52, n. 7, p. 555–600, 1929.
- Braghini, D.; Lima, V. D. de; Beli, D.; Rosa, M. I.; Arruda, J. R. d. F. Non-Hermitian acoustic waveguides with periodic electroacoustic feedback. **arXiv preprint arXiv:2210.05948**, 2022.
- Braghini, D.; Peet, M. M. Computing optimal upper bounds on the  $h_2$ -norm of ode-pde systems using linear partial inequalities. **IFAC-PapersOnLine**, v. 56, n. 2, p. 6994–6999, 2023.
- Braghini, D.; Villani, L. G. G.; Rosa, M. I. N.; Arruda, J. R. F. Non-Hermitian elastic waveguides with piezoelectric feedback actuation: non-reciprocal bands and skin modes. **Journal of Physics D: Applied Physics**, v. 54, n. 28, p. 285302, 2021.
- Brandenbourger, M.; Locsin, X.; Lerner, E.; Coulais, C. Non-reciprocal robotic metamaterials. **Nature Communications**, v. 10, n. 1, p. 4608, 2019.
- Brillouin, L. **Wave propagation in periodic structures**. [S.l.]: MGH, 1946.
- Budich, J. C.; Bergholtz, E. J. Non-Hermitian topological sensors. **Physical Review Letters**, v. 125, n. 18, p. 180403, 2020.
- Chen, Y.; Li, X.; Scheibner, C.; Vitelli, V.; Huang, G. Realization of active metamaterials with odd micropolar elasticity. **Nature Communications**, v. 12, n. 1, p. 5935, 2021.
- Das, A.; Shivakumar, S.; Weiland, S.; Peet, M.  $H_\infty$  optimal estimation for linear coupled PDE systems. In: IEEE. **2019 IEEE 58th Conference on Decision and Control (CDC)**. [S.l.], 2019. p. 262–267.

- Doyle, J. F. **Wave Propagation in Structures**. [S.l.]: Springer, 2021.
- Eshraqi, E.; Shahravi, M.; Azimi, M. Consideration of spillover effect in active vibration suppression of a smart composite plate using piezoelectric elements. **Latin American Journal of Solids and Structures**, v. 13, n. 14, p. 2643–2656, 2016.
- Faulkner, M.; Hong, D. Free vibrations of a mono-coupled periodic system. **Journal of Sound and Vibration**, v. 99, n. 1, p. 29–42, 1985.
- Feynman, R. P.; Leighton, R. B.; Sands, M. The feynman lectures on physics; vol. i. **American Journal of Physics**, v. 33, n. 9, p. 750–752, 1965.
- Fioravanti, A.; Bonnet, C.; H.Özbay; Niculescu, S. A numerical method for stability windows and unstable root-locus calculation for linear fractional time-delay systems. **Automatica**, v. 48, n. 11, p. 2824–2830, 2012.
- Fok, L.; Ambati, M.; Zhang, X. Acoustic metamaterials. **Materials Research Society Bulletin**, v. 33, n. 10, p. 931–934, 2008.
- Gahlawat, A.; Valmorbida, G. Stability analysis of linear partial differential equations with generalized energy functions. **IEEE Transactions on Automatic Control**, v. 65, n. 5, p. 1924–1939, 2019.
- Gong, Z.; Ashida, Y.; Kawabata, K.; Takasan, K.; Higashikawa, S.; Ueda, M. Topological phases of Non-Hermitian systems. **Physical Review X**, v. 8, n. 3, p. 031079, 2018.
- Goto, A.; Nobrega, E.; Pereira, V.; Costa, D.; Dos Santos, J. One-dimensional phononic crystal dynamic analysis by spectral transfer matrix method. In: ABCM. **Proceedings of the XVIII International Symposium on Dynamic Problems of Mechanics**. [S.l.], 2019.
- Gupta, M.; Ruzzene, M. Dynamics of quasiperiodic beams. **Crystals**, v. 10, n. 12, p. 1144, 2020.
- Gurtin, M. E. **An introduction to continuum mechanics**. [S.l.]: Academic press, 1982.
- Hall, J. F. Problems encountered from the use (or misuse) of rayleigh damping. **Earthquake Engineering & Structural Dynamics**, v. 35, n. 5, p. 525–545, 2006.
- Hasan, M. Z.; Kane, C. L. Colloquium: topological insulators. **Reviews of Modern Physics**, v. 82, n. 4, p. 3045, 2010.
- Huang, C.; Chen, L. Negative poisson's ratio in modern functional materials. **Advanced Materials**, v. 28, n. 37, p. 8079–8096, 2016.
- Huber, S. D. Topological mechanics. **Nature Physics**, v. 12, n. 7, p. 621–623, 2016.
- Hussein, M. I.; Biringen, S.; Bilal, O. R.; Kucala, A. Flow stabilization by subsurface phonons. **Proceedings of the Royal Society A: Mathematical, Physical and Engineering Sciences**, v. 471, n. 2177, p. 20140928, 2015.
- Hussein, M. I.; Hulbert, G. M.; A.Scott, R. Dispersive elastodynamics of 1d banded materials and structures: analysis. **Journal of Sound and Vibration**, v. 289, n. 4-5, p. 779–806, 2006.

Hussein, M. I.; Leamy, M. J.; Ruzzene, M. Dynamics of phononic materials and structures: Historical origins, recent progress, and future outlook. **Applied Mechanics Reviews**, v. 66, n. 4, p. 040802, 2014.

Iwasaki, T. Robust performance analysis for systems with norm-bounded time-varying structured uncertainty. In: **Proceedings of 1994 American Control Conference-ACC'94**. [S.l.: s.n.], 1994. v. 2, p. 2343–2347.

Jagt, D.; Peet, M. A PIE representation of coupled linear 2D PDEs and stability analysis using LPIs. In: **IEEE. 2022 American Control Conference (ACC)**. [S.l.], 2022. p. 1659–1666.

Jagt, D.; Peet, M. A PIE representation of coupled linear ODE-PDE systems with constant delay and stability analysis using LPIs. **arXiv**, 2022.

Jarlebring, E.; Vanbiervliet, J.; Michiels, W. Characterizing and computing the  $\mathcal{H}_2$  norm of time-delay systems by solving the delay Lyapunov equation. **IEEE Transactions on Automatic Control**, v. 56, n. 4, p. 814–825, 2011.

Johnson, C. **Numerical solution of partial differential equations by the finite element method**. [S.l.]: Courier Corporation, 2012.

Kinsler, L. E.; Frey, A. R.; Coppens, A. B.; Sanders, J. V. **Fundamentals of acoustics**. [S.l.]: John Wiley & Sons, 2000.

Krstic, M.; Smyshlyaev, A. **Boundary control of PDEs: A course on backstepping designs**. [S.l.]: SIAM, 2008.

Li, L.; Guo, Y. Analysis of longitudinal waves in rod-type piezoelectric phononic crystals. **Crystals**, v. 6, n. 4, p. 45, 2016.

Longhi, S. Non-Hermitian skin effect beyond the tight-binding models. **Physical Review B**, v. 104, p. 125109, 2021.

Ma, G.; Xiao, M.; Chan, C. T. Topological phases in acoustic and mechanical systems. **Nature Reviews Physics**, v. 1, n. 4, p. 281–294, 2019.

Mace, B.; Manconi, E. Modelling wave propagation in two-dimensional structures using a wave/finite element technique. In: **COMPADYN 2007: Computational Methods in Structural Dynamics and Earthquake Engineering (13/06/07 - 16/06/07)**. [S.l.: s.n.], 2007.

Maddi, A.; Auregan, Y.; Penelet, G.; Pagneux, V.; Achilleos, V. Exact analog of the hatano-nelson model in one-dimensional continuous nonreciprocal systems. **Physical Review Research**, v. 6, n. 1, p. L012061, 2024.

Maldovan, M. Sound and heat revolutions in phononics. **Nature**, v. 503, n. 7475, p. 209–217, 2013.

Mattenet, S.; Iuliis, V. D.; Gomez, M.; Michiels, W.; Jungers, R. An improved finiteness test and a systematic procedure to compute the strong  $h_2$  norm of differential algebraic systems with multiple delays. **Automatica**, v. 144, p. 110495, 2022.

Mencik, J.-M. New advances in the forced response computation of periodic structures using the wave finite element (wfe) method. **Computational Mechanics**, v. 54, p. 789–801, 2014.

- Meyer, C. D. **Matrix analysis and applied linear algebra**. [S.l.]: SIAM, 2023.
- Michiels, W.; Zhou, B. Computing delay Lyapunov matrices and  $\mathcal{H}_2$  norms for large-scale problems. **SIAM Journal on Matrix Analysis and Applications**, v. 40, n. 3, p. 845–869, 2019.
- Moran, M. J.; Shapiro, H. N.; Boettner, D. D.; Bailey, M. B. **Fundamentals of engineering thermodynamics**. [S.l.]: John Wiley & Sons, 2010.
- Morris, K.; Demetriou, M.; Yang, S. Using  $H_2$ -control performance metrics for the optimal actuator location of distributed parameter systems. **IEEE Transactions on Automatic Control**, v. 60, n. 2, p. 450–462, 2015.
- Morris, K.; Levine, W. Control of systems governed by partial differential equations. **The Control Systems Handbook**, 2010.
- Okuma, N.; Kawabata, K.; Shiozaki, K.; Sato, M. Topological origin of non-Hermitian skin effects. **Physical Review Letters**, v. 124, p. 086801, 2020.
- Pal, R. K.; Rosa, M. I.; Ruzzene, M. Topological bands and localized vibration modes in quasiperiodic beams. **New Journal of Physics**, v. 21, n. 9, p. 093017, 2019.
- Peet, M. A partial integral equation (PIE) representation of coupled linear PDEs and scalable stability analysis using LMIs. **Automatica**, v. 125, p. 109473, 2021.
- Peet, M. Representation of networks and systems with delay: DDEs, DDFs, ODE–PDEs and PIEs. **Automatica**, v. 127, p. 109508, 2021.
- Pekar, L.; Kureckova, E. Rational approximations for time-delay systems: case studies. In: **Proceedings of the 13th WSEAS international conference on Mathematical and computational methods in science and engineering**. [S.l.: s.n.], 2011. p. 217–222.
- Prajna, S.; Papachristodoulou, A.; Parrilo, P. A. Introducing sostools: A general purpose sum of squares programming solver. In: IEEE. **Proceedings of the 41st IEEE Conference on Decision and Control, 2002**. [S.l.], 2002. v. 1, p. 741–746.
- MS Ribeiro, L. H.; Braghini, D.; Beli, D.; Claeys, C.; Chronopoulos, D.; F Arruda, J. R. On the robustness of interface topological modes on rods. In: European Acoustics Association. **Proceedings of the Forum Acusticum 2023 Conference**. [S.l.], 2023. p. 1993–1997.
- Rosa, M.; Lima, V.; Santos, J.; Arruda, J. Numerical and experimental investigation of interface modes in periodic acoustic waveguides. **Proceedings of ICEDYN**, 2017.
- Rosa, M. I.; Pal, R. K.; Arruda, J. R.; Ruzzene, M. Edge states and topological pumping in spatially modulated elastic lattices. **Physical Review Letters**, v. 123, n. 3, p. 034301, 2019.
- Rosa, M. I. N. **Dynamics and topology of modulated elastic media**. Tese (Doutorado) — University of Colorado at Boulder, 2022.
- Rosa, M. I. N.; Ruzzene, M. Dynamics and topology of Non-Hermitian elastic lattices with non-local feedback control interactions. **New Journal of Physics**, v. 22, n. 5, p. 053004, 2020.
- Scherer, C.; Gahinet, P.; Chilali, M. Multiobjective output-feedback control via LMI optimization. **IEEE Transactions on Automatic Control**, v. 42, n. 7, p. 896–911, 1997.

- Shivakumar, S.; Das, A.; Weiland, S.; Peet, M. M. A generalized lmi formulation for input-output analysis of linear systems of odes coupled with pdes. In: IEEE. **2019 IEEE 58th conference on decision and control (CDC)**. [S.l.], 2019. p. 280–285.
- Shivakumar, S.; Das, A.; Weiland, S.; Peet, M. Extension of the partial integral equation representation to GPDE input-output systems. **arXiv**, 2022.
- Shivakumar, S.; Das, A.; Weiland, W. S.; Peet, M. Duality and  $\mathcal{H}_\infty$ -optimal control of coupled ODE-PDE systems. In: IEEE. **2020 59th IEEE Conference on Decision and Control (CDC)**. [S.l.], 2020. p. 5689–5696.
- Shivakumar, S.; Jagt, D.; Braghini, D.; Das, A.; Peet, M. PIETOOLS 2022: User manual. **arXiv**, 2022.
- Sigalas, M.; Economou, E. N. Band structure of elastic waves in two dimensional systems. **Solid State Communications**, v. 86, n. 3, p. 141–143, 1993.
- Silva, P. B. *et al.* **Dynamic analysis of periodic structures via wave-based numerical approaches and substructuring techniques**. Tese (Doutorado) — Universidade Estadual de Campinas (UNICAMP). Faculdade de Engenharia Mecânica, 2015.
- Simon, B. Holonomy, the quantum adiabatic theorem, and berry's phase. **Physical Review Letters**, v. 51, n. 24, p. 2167, 1983.
- Valmorbida, G.; Ahmadi, M.; Papachristodoulou, A. Stability analysis for a class of partial differential equations via semidefinite programming. **IEEE Transactions on Automatic Control**, v. 61, n. 6, p. 1649–1654, 2015.
- VanGessel, F.; Peng, J.; Chung, P. W. A review of computational phononics: the bulk, interfaces, and surfaces. **Journal of Materials Science**, v. 53, p. 5641–5683, 2018.
- Walter, R. **Real and complex analysis**. [S.l.]: McGraw-Hill Book Company, 1987.
- Wang, X. Dynamic behaviour of a metamaterial system with negative mass and modulus. **International Journal of Solids and Structures**, v. 51, n. 7-8, p. 1534–1541, 2014.
- Won, C.; Sparks, D.; Belvin, K.; Sulla, J. Application of piezoelectric devices to vibration suppression-from modeling and controller designs to implementation. In: American Institute of Aeronautics and Astronautics. **Aerodynamics Conference 1992**. [S.l.], 1992. p. 4610.
- Xiao, M.; Ma, G.; Yang, Z.; Sheng, P.; Zhang, Z.; Chan, C. T. Geometric phase and band inversion in periodic acoustic systems. **Nature Physics**, v. 11, n. 3, p. 240–244, 2015.
- Zhao, G.; Chen, B.; Gu, Y. Active control of flexible systems. **Journal of Optimization Theory and Applications**, v. 25, p. 415–436, 1978.
- Zhong, J.; Wang, K.; Park, Y.; Asadchy, V.; Wojcik, C. C.; Dutt, A.; Fan, S. Nontrivial point-gap topology and non-Hermitian skin effect in photonic crystals. **Phys. Rev. B**, v. 104, p. 125416, 2021.
- Zhou, W.; Lim, C. *et al.* Topological edge modeling and localization of protected interface modes in 1d phononic crystals for longitudinal and bending elastic waves. **International Journal of Mechanical Sciences**, v. 159, p. 359–372, 2019.

Zigoneanu, L.; Popa, B.-I.; Cummer, S. A. Three-dimensional broadband omnidirectional acoustic ground cloak. **Nature Materials**, v. 13, n. 4, p. 352–355, 2014.

## APPENDIX A – NUMERICAL METHODS

*“It is unnecessary to point out that the customary treatment of a canonical set of equations in the lumped theory has no parallel in the distributed context, except in a very formal and almost uninteresting sense. A more objectionable, though superficially appealing route, is to lump the distributed systems and then apply the lumped theory.”*

*(G.A. Phillipson in the preface of “Identification of Distributed Systems”)*

## A.1 FEM

FEM is a widely used, flexible, and computationally tractable method to obtain approximate solutions for systems governed by differential equations; it is especially appealing for PDE systems since sometimes there are no exact solutions. FEM is a particular case of *Galerkin* method, an approximation method that consists of projecting the solution  $u$ , an element of a *Hilbert* space of measures with continuity constraints and satisfying appropriate boundary conditions, into a finite-dimensional subspace with basis functions  $\{\phi_j\}_{e=1}^M$ , with respect to the corresponding inner-product (Johnson, 2012). The projection corresponds to the following approximation

$$u(t, x) \approx \sum_{e=0}^M c_e(t) \phi_e(x), \quad (\text{A.1})$$

provided that the approximate solution satisfies the essential boundary conditions, i.e. the solution value evaluated at some boundary.

In FEM, the basis functions are imposed as piecewise polynomials, and the dimension  $M$  is the number of internal nodes in the mesh, i.e., the partition of the domain into disjoint subintervals. Let's considered the simple case when  $\phi_e$  are piecewise linear as defined in Eq. (A.2) and the one-dimensional domain  $D = (0, L) = \cup_{e=1}^{M+1} D_e$ , such that  $D_e = (x_{e-1}, x_e)$ , are equally-spaced sub-domains of length  $L_e$  (Atalla; Sgard, 2015).

$$\phi_e(x) = \begin{cases} 0, & \text{if } x_0 \leq x < x_{e-1} \text{ or } x_e < x \leq x_{M+1} \\ \frac{x-x_{e-1}}{L_e}, & \text{if } x_{e-1} \leq x < x_e \\ \frac{x_{e+1}-x}{L_e}, & \text{if } x_e \leq x \leq x_{e+1} \end{cases} \quad (\text{A.2})$$

The result of applying the FEM formulation on PDE systems is a set of ODEs. Consider  $nd$  ODEs where  $nd \in \mathbb{N}$  is the number of degrees of freedom (DOF) of the metastructure corresponding to the metamaterial built by the periodic arrangement of  $nc \in \mathbb{N}$  unit cells:

$$\mathbf{M}\ddot{\mathbf{q}}(t) + \mathbf{R}\dot{\mathbf{q}}(t) + \mathbf{K}\mathbf{q}(t) = \mathbf{w}_a(t) + \mathbf{u}_a(t), \quad (\text{A.3})$$

where  $(\mathbf{M}, \mathbf{R}, \mathbf{K})$  are matrices  $\in \mathbb{R}^{N \times N}$  that result directly from the equations of motion in the case of ODE systems.  $\mathbf{q} : [0, T] \rightarrow \mathbb{R}^N$  is a vector-valued time signal, and  $\mathbf{q}(t)$  is the vector of which the entries are the physical variables at every node of the mesh. The vector-valued signal  $w_a$  represents an external perturbation, whereas  $u_a$  represents the applied

feedback effort. The matrix  $\mathbf{R}$  can be built to model structural (hysteretic) damping or viscous (*Rayleigh*) damping.

#### A.1.1 A state-space framework for periodically applied output feedback

By using state-space realizations of (A.3), it is possible to decouple the passive system and the feedback law. As shown here, this allows an algorithmic procedure to build a numerical model of the metastructure with a generalized feedback law, periodically applied or not, with next-neighborhood or even long-range, non-reciprocal coupling (local or non-local feedback).

First, the state vector  $\mathbf{x}(t) = (\mathbf{q}(t), \dot{\mathbf{q}}(t))$  is defined. Then, (A.3) can be rewritten in matrix form, with  $w : [0, T] \rightarrow \mathbb{R}$  denoting the external input signal, which is a real-valued function of time, as follows

$$\dot{\mathbf{x}}(t) = \begin{bmatrix} \mathbf{0} & \mathbf{I} \\ -\mathbf{M}^{-1}\mathbf{K} & -\mathbf{M}^{-1}\mathbf{R} \end{bmatrix} \mathbf{x}(t) + \begin{bmatrix} \mathbf{0} \\ \mathbf{M}^{-1}\mathbf{W} \end{bmatrix} w(t) + \begin{bmatrix} \mathbf{0} \\ \mathbf{M}^{-1}\mathbf{U} \end{bmatrix} \mathbf{u}(t), \quad (\text{A.4})$$

such that  $w_a(t) = \mathbf{W}w(t)$  and  $u_a(t) = \mathbf{U}u(t)$ , with  $\mathbf{W} \in \mathbb{R}^{N \times 1}$  and  $\mathbf{U} \in \mathbb{R}^{N \times N-1}$ . On the other hand, for the output signal  $z : [0, T] \rightarrow \mathbb{R}^N$  to give the physical variables, the following equation is defined

$$\mathbf{z}(t) = \begin{bmatrix} \mathbf{I} & \mathbf{0} \end{bmatrix} \mathbf{x}(t). \quad (\text{A.5})$$

For the measured states given by the sensors,  $y : [0, T] \rightarrow \mathbb{R}^{n_c - a}$ , the equation is

$$\mathbf{y}(t) = \begin{bmatrix} \mathbf{Y} & \mathbf{0} \end{bmatrix} \mathbf{x}(t), \quad (\text{A.6})$$

such that  $\mathbf{Y}$  selects the sensor DOFs as outputs, with the matrix coordinates below.  $n_1$  is the DOF where the sensor is placed, represented by  $x_1$  on Fig. 2.14 for example, in the first unit cell of the array. Note that, in the arbitrary non-local feedback case, one has  $n_c - a$  sensors and actuators, since the first  $a$  cells of the finite arrangement are endowed with sensors but no actuator, whereas the last  $a$  cells are endowed only with actuators.

$$Y_{ij} = \begin{cases} 1 & \text{if } j = n_1 + (i - 1)n_e \forall i \in \mathbb{Z} \text{ such that } 1 \leq i \leq n_c - a; \\ 0 & \text{otherwise.} \end{cases} \quad (\text{A.7})$$

Thus, one can define the passive (open-loop) linear, time-invariant, system  $S$  with inputs  $w$  and  $u$  and outputs  $z$  and  $y$  as expressed in A.8. Particularly,  $\mathbf{D}_{11}$ ,  $\mathbf{D}_{12}$ ,  $\mathbf{D}_{21}$  and  $\mathbf{D}_{22}$  are all null matrices.

$$\begin{cases} \dot{\mathbf{x}}(t) = \mathbf{A}\mathbf{x}(t) + \mathbf{B}_1 w(t) + \mathbf{B}_2 \mathbf{u}(t) \\ \mathbf{z}(t) = \mathbf{C}_1 \mathbf{x}(t) + \mathbf{D}_{11} w(t) + \mathbf{D}_{12} \mathbf{u}(t), \\ \mathbf{y}(t) = \mathbf{C}_2 \mathbf{x}(t) + \mathbf{D}_{21} w(t) + \mathbf{D}_{22} \mathbf{u}(t). \end{cases} \quad (\text{A.8})$$

The feedback law can be expressed in the state-space formulation for the system with  $n_c - a$  inputs (measured signals) and  $n_c - a$  outputs (actuation efforts) and any given transfer function  $H(s)$ . In particular, if the system is periodic, the same transfer function acts on every unit cell, and each cell has at most one sensor and one actuator, meaning that the state-space representation  $H^{(1)}(s)$ , with the measured signal  $y_{i-a}(t) \in \mathbb{R}$  and the feedback effort  $u_i(t) \in \mathbb{R}$ , applied to the  $i$ -th cell,  $\forall a + 1 \leq i < n_c$ , can be expressed generally as the  $n_{xi}$ -order linear system below, whose state vector is  $\mathbf{x}_i(t) \in \mathbb{R}^{n_{xi}}$ .

$$\begin{cases} \dot{\mathbf{x}}_i(t) = \mathbf{A}_c^{(1)} \mathbf{x}_i(t) + \mathbf{B}_c^{(1)} y_i(t), \\ u_i(t) = \mathbf{C}_c^{(1)} \mathbf{x}_i(t) + \mathbf{D}_c^{(1)} y_i(t). \end{cases} \quad (\text{A.9})$$

Now, define  $H^{(k-1)}$  as the  $k - 1$  system of a sequence of systems augmented by adding one feedback relation at each term of the sequence, such that the vectors  $\mathbf{x}_i^{(k-1)}(t) = (\mathbf{x}_i(t), \mathbf{x}_i(t), \dots)$ ,  $\mathbf{y}_i^{(k-1)}(t) = (y_i(t), y_i(t), \dots)$  and  $\mathbf{u}_i^{(k-1)}(t) = (u_i(t), u_i(t), \dots)$  were augmented with  $\mathbf{x}_i(t)$ ,  $u_i(t)$  and  $y_i(t)$ , respectively,  $k - 1$  times. Then, since the feedback laws are independent from each other, the  $(k - 1) \cdot n_{xi}$ -order system  $H^{(k-1)}$  has, by construction, block diagonal matrices  $(\mathbf{A}_c^{(k-1)}, \mathbf{B}_c^{(k-1)}, \mathbf{C}_c^{(k-1)}, \mathbf{D}_c^{(k-1)})$ , in the following way

$$\mathbf{A}_c^{(k-1)} = \begin{bmatrix} \mathbf{A}_c^{(1)} & \dots & \mathbf{0} \\ \vdots & \ddots & \vdots \\ \mathbf{0} & \dots & \mathbf{A}_c^{(1)} \end{bmatrix}, \quad \mathbf{B}_c^{(k-1)} = \begin{bmatrix} \mathbf{B}_c^{(1)} & \dots & \mathbf{0} \\ \vdots & \ddots & \vdots \\ \mathbf{0} & \dots & \mathbf{B}_c^{(1)} \end{bmatrix}, \quad (\text{A.10})$$

$$\mathbf{C}_c^{(k-1)} = \begin{bmatrix} \mathbf{C}_c^{(1)} & \dots & \mathbf{0} \\ \vdots & \ddots & \vdots \\ \mathbf{0} & \dots & \mathbf{C}_c^{(1)} \end{bmatrix}, \quad \mathbf{D}_c^{(k-1)} = \begin{bmatrix} \mathbf{D}_c^{(1)} & \dots & \mathbf{0} \\ \vdots & \ddots & \vdots \\ \mathbf{0} & \dots & \mathbf{D}_c^{(1)} \end{bmatrix} \quad (\text{A.11})$$

Thus, the next term of this sequence,  $H^{(k)}$ , is defined with the vectors  $\mathbf{x}_i^{(k)}(t) = (\mathbf{x}_i^{(k-1)}(t), \mathbf{x}_i(t))$ ,  $\mathbf{y}_i^{(k)}(t) = (\mathbf{y}_i^{(k-1)}(t), y_i(t))$  and  $\mathbf{u}_i^{(k)}(t) = (\mathbf{u}_i^{(k-1)}(t), u_i(t))$ . This system is clearly a  $k \cdot n_{xi}$ -order linear system represented by block diagonal matrices  $(\mathbf{A}_c^{(k)}, \mathbf{B}_c^{(k)}, \mathbf{C}_c^{(k)}, \mathbf{D}_c^{(k)})$

augmented from the previously defined matrices, in block form, as follows:

$$\mathbf{A}_c^{(k)} = \begin{bmatrix} \mathbf{A}_c^{(k-1)} & \mathbf{0} \\ \mathbf{0} & \mathbf{A}_c^{(1)} \end{bmatrix}, \mathbf{B}_c^{(k)} = \begin{bmatrix} \mathbf{B}_c^{(k-1)} & \mathbf{0} \\ \mathbf{0} & \mathbf{B}_c^{(1)} \end{bmatrix}, \quad (\text{A.12})$$

$$\mathbf{C}_c^{(k)} = \begin{bmatrix} \mathbf{C}_c^{(k-1)} & \mathbf{0} \\ \mathbf{0} & \mathbf{C}_c^{(1)} \end{bmatrix}, \mathbf{D}_c^{(k)} = \begin{bmatrix} \mathbf{D}_c^{(k-1)} & \mathbf{0} \\ \mathbf{0} & \mathbf{D}_c^{(1)} \end{bmatrix} \quad (\text{A.13})$$

Thus, by induction, one concludes that, by defining  $H = H^{(n_c - a)}$  one have the state-space representation of the feedback interactions as a  $(n_c - a) \cdot n_{xi}$ -order linear system with block diagonal matrices, as follows

$$\begin{cases} \dot{\mathbf{x}}_c(t) = \mathbf{A}_c \mathbf{x}_c(t) + \mathbf{B}_c \mathbf{y}(t), \\ \mathbf{u}(t) = \mathbf{C}_c \mathbf{x}_c(t) + \mathbf{D}_c \mathbf{y}(t). \end{cases} \quad (\text{A.14})$$

Finally, the interconnection  $(S, H)$  (closed-loop) can be written in terms of the previously defined state-space matrices, as

$$\begin{cases} \dot{\mathbf{x}}_a(t) = \mathbf{A}_{cl} \mathbf{x}_a(t) + \mathbf{B}_{cl} w(t), \\ \mathbf{z}(t) = \mathbf{C}_{cl} \mathbf{x}_a(t) + \mathbf{D}_{cl} w(t), \end{cases} \quad (\text{A.15})$$

with the augmented state  $\mathbf{x}_a(t) = (\mathbf{x}(t), \mathbf{x}_c(t))$ ,

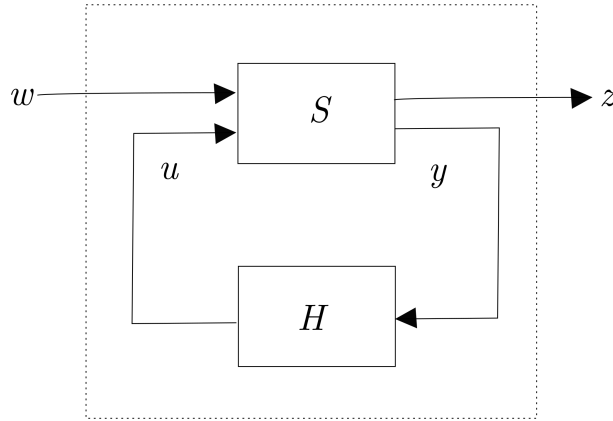


Figure A.1 –  $(S, H)$  interconnection scheme with corresponding signals  $w$ ,  $z$ ,  $u$  and  $y$ .

It can be shown that the closed-loop matrices are written, in terms of the previously defined matrices, as

$$\mathbf{A}_{cl} = \begin{bmatrix} \mathbf{A} + \mathbf{B}_2 \mathbf{D}_c \mathbf{C}_2 & \mathbf{B}_2 \mathbf{C}_c \\ \mathbf{B}_c \mathbf{C}_2 & \mathbf{A}_c \end{bmatrix}, \mathbf{B}_{cl} = \begin{bmatrix} \mathbf{B}_1 + \mathbf{B}_2 \mathbf{D}_c \mathbf{D}_{21} \\ \mathbf{B}_c \mathbf{D}_{21} \end{bmatrix}, \quad (\text{A.16})$$

$$\mathbf{C}_{cl} = \begin{bmatrix} \mathbf{C}_1 + \mathbf{D}_{21} \mathbf{D}_c \mathbf{C}_2 & \mathbf{D}_{21} \mathbf{C}_c \end{bmatrix}, \mathbf{D}_{cl} = \begin{bmatrix} \mathbf{D}_{11} + \mathbf{D}_{12} \mathbf{D}_c \mathbf{D}_{21} \end{bmatrix} \quad (\text{A.17})$$

Thus, the closed loop is a linear, time-invariant system that gives  $z$  as output for any external load  $w$ . The internal stability of this system can also be analyzed by computing the eigenvalues of  $\mathbf{A}_{cl}$ . This is a conservative way to analyze the behavior of  $z$  for any given load  $w$ , as internal stability is a sufficient, but not a necessary condition for input-output stability.

**Remark 1.** Define the signals in the frequency domain as given by the Laplace transform, for instance, indicated by  $\hat{(\cdot)}$ . Then,  $H(s) = \hat{u}(s)_i / \hat{y}(s)_{i-a}$ . Particularly for the acoustic system,  $y_{i-a} = p_s$  is the measured pressure, and  $u_i$  is the volume acceleration. Thus, the feedback law in terms of volume velocity, as previously defined on (2.61), is actually given more generically by the transfer function  $H_v(s) = \frac{H(s)}{s}$ .

**Remark 2.** Note that, in this model, since the passive ( $S$ ) part was separated from the active part ( $H$ ) of the structure, the coupling between measurements and applied feedback signals can be generically selected by the state-space model of  $S$  through the matrices involved in the relation between  $y$  and  $u$  on A.8 and A.14, following the design requirements.

For instance, in the lumped models used in (Rosa; Ruzzene, 2020), the feedback law was defined on the  $i$ -th lumped element as  $F_i = k(\mathbf{q}_{i-a} - \mathbf{q}_{i-a-1})$  with the same range  $a$  defined here, but with  $a+1 \leq i \leq N$ . Thus,  $n_c = N - a - 1$ , and one just need to replace  $C_{2ss}$  by the composition of  $Y^l$ , a bi-diagonal matrix of dimension  $n_c \times n_c + 1$  (defined in the following) with a zero matrix on the same way as in A.5.

$$Y_{ij}^l = \begin{cases} -1 \text{ if } j = i, 1 \text{ if } j = i + 1 \forall i \in \mathbb{Z} \text{ such that } 1 \leq i \leq n_c; \\ 0 \text{ otherwise.} \end{cases} \quad (\text{A.18})$$

As an example, consider  $N = 4$  masses fixed to rigid walls at the boundaries with proportional feedback. Thus, the matrices are

$$\mathbf{G} = g \begin{bmatrix} 0 & 0 & 0 & 0 \\ 1 & -1 & 0 & 0 \\ 0 & 1 & -1 & 0 \\ 0 & 0 & 1 & -1 \end{bmatrix} = g\mathbf{H} \quad \mathbf{M} = m \begin{bmatrix} 1 & 0 & 0 & 0 \\ 0 & 1 & 0 & 0 \\ 0 & 0 & 1 & 0 \\ 0 & 0 & 0 & 1 \end{bmatrix} \quad \mathbf{R} = b \begin{bmatrix} 2 & -1 & 0 & 0 \\ -1 & 2 & -1 & 0 \\ 0 & -1 & 2 & -1 \\ 0 & 0 & -1 & 2 \end{bmatrix} \quad \mathbf{K} = k \begin{bmatrix} 2 & -1 & 0 & 0 \\ -1 & 2 & -1 & 0 \\ 0 & -1 & 2 & -1 \\ 0 & 0 & -1 & 2 \end{bmatrix}$$

$$\mathbf{A} = \begin{bmatrix} 0 & 0 & 0 & 0 & 1 & 0 & 0 & 0 \\ 0 & 0 & 0 & 0 & 0 & 1 & 0 & 0 \\ 0 & 0 & 0 & 0 & 0 & 0 & 1 & 0 \\ 0 & 0 & 0 & 0 & 0 & 0 & 0 & 1 \\ -2k/m & k/m & 0 & 0 & -2b/m & b/m & 0 & 0 \\ k/m - g/m & -2k/m + g/m & k/m & 0 & b/m & -2b/m & b/m & 0 \\ 0 & k/m - g/m & -2k/m + g/m & k/m & 0 & b/m & -2b/m & b/m \\ 0 & 0 & k/m - g/m & -2k/m + g/m & 0 & 0 & b/m & -2b/m \end{bmatrix} \quad \mathbf{B}_1 = \begin{bmatrix} 0 \\ 0 \\ 0 \\ 0 \\ 0 \\ 0 \\ 1/m \\ 0 \end{bmatrix}$$

$$\mathbf{B}_2 = \begin{bmatrix} 0 & 0 & 0 \\ 0 & 0 & 0 \\ 0 & 0 & 0 \\ 0 & 0 & 0 \\ 1/m & 0 & 0 \\ 0 & 1/m & 0 \\ 0 & 0 & 1/m \end{bmatrix} \quad \mathbf{C}_1 = \begin{bmatrix} 1 & 0 & 0 & 0 & 0 & 0 & 0 & 0 \\ 0 & 1 & 0 & 0 & 0 & 0 & 0 & 0 \\ 0 & 0 & 1 & 0 & 0 & 0 & 0 & 0 \\ 0 & 0 & 0 & 1 & 0 & 0 & 0 & 0 \end{bmatrix} \quad \mathbf{C}_2 = \begin{bmatrix} -1 & 1 & 0 & 0 & 0 & 0 & 0 & 0 \\ 0 & -1 & 1 & 0 & 0 & 0 & 0 & 0 \\ 0 & 0 & -1 & 1 & 0 & 0 & 0 & 0 \end{bmatrix} \quad \mathbf{F} = \begin{bmatrix} 0 \\ 0 \\ 1 \\ 0 \end{bmatrix}$$

$$\mathbf{T} = \begin{bmatrix} 0 & 0 & 0 \\ 1 & 0 & 0 \\ 0 & 1 & 0 \\ 0 & 0 & 1 \end{bmatrix} \quad \mathbf{Y} = \begin{bmatrix} -1 & 1 & 0 & 0 \\ 0 & -1 & 1 & 0 \\ 0 & 0 & -1 & 1 \end{bmatrix} \quad \mathbf{D}_c = \begin{bmatrix} g & 0 & 0 \\ 0 & g & 0 \\ 0 & 0 & g \end{bmatrix}$$

## A.2 SEM

In SEM, developed in (Doyle, 2021), the goal is to find the analytical dynamic stiffness matrix  $\mathbf{D}_c(\omega)$  for all frequencies  $\omega \in \mathbb{C}$ . With this matrix, one can easily find the transfer matrix as explained in plenty of references, such as (Hussein *et al.*, 2014). The eigenvalues of the transfer matrix have well-known structure given by *Bloch's* theorem and, thus, the problem of finding  $\omega(\kappa)$ , i.e., the dispersion relation of an infinite waveguide as the complex frequency for imposed real values of wavenumber  $\kappa$ , can be solved.

Consider the general unit cell given by Fig. 2.14. One spectral element can be assigned for each continuous segment of the domain. This implies three spectral elements for this cell, one for each segment connecting the nodes  $x_0$ ,  $x_1$ ,  $x_2$ , and  $x_3$ . For the simple one-dimensional models used in this work, each element connects the left to the right nodes like in Eq. (A.19). The dynamic stiffness matrix  $\mathbf{K}_j(\omega)$  relates generalized forces to generalized displacements in the frequency domain (via Fourier transform) of the nodes of the  $j$ -th element.

$$\begin{bmatrix} \hat{F}_l(\omega) \\ \hat{F}_r(\omega) \end{bmatrix} = \mathbf{K}_j(\omega) \begin{bmatrix} \hat{q}_l(\omega) \\ \hat{q}_r(\omega) \end{bmatrix} \quad (\text{A.19})$$

Composing the nodes of the unit cell with the conditions of equilibrium and continuity in the interfaces leads to the global dynamic stiffness matrix  $\mathbf{K}(\omega)$

$$\begin{bmatrix} \hat{f}_0(\omega) \\ \hat{f}_1(\omega) \\ \hat{f}_2(\omega) \\ \hat{f}_3(\omega) \end{bmatrix} = \mathbf{K}(\omega) \begin{bmatrix} \hat{q}_0(\omega) \\ \hat{q}_1(\omega) \\ \hat{q}_2(\omega) \\ \hat{q}_3(\omega) \end{bmatrix}. \quad (\text{A.20})$$

Adding the previously defined feedback input, as in Eq. (A.21), to the left-hand side of the equation, such that  $H$  is the transfer function corresponding to the general non-local, concentrated feedback law being considered.

$$v = \begin{bmatrix} 0 \\ 0 \\ \hat{f}_{fb}(j\omega) \\ 0 \end{bmatrix} = \begin{bmatrix} 0 & 0 & 0 & 0 \\ 0 & 0 & 0 & 0 \\ 0 & H(j\omega)e^{ikaL_c} & 0 & 0 \\ 0 & 0 & 0 & 0 \end{bmatrix} \begin{bmatrix} \hat{q}_0(\omega) \\ \hat{q}_1(\omega) \\ \hat{q}_2(\omega) \\ \hat{q}_3(\omega) \end{bmatrix} \quad (\text{A.21})$$

Thus,  $v$  can be added to the dynamic stiffness matrix in the following way

$$\mathbf{K}(\omega) = \begin{bmatrix} \mathbf{K}_1(1,1) & \mathbf{K}_1(1,2) & 0 & 0 \\ \mathbf{K}_1(2,1) & \mathbf{D}_1 & \mathbf{K}_2(1,2) & 0 \\ 0 & \mathbf{C} & \mathbf{D}_2 & \mathbf{K}_3(1,2) \\ 0 & 0 & \mathbf{K}_3(2,1) & \mathbf{K}_3(2,2) \end{bmatrix}, \quad (\text{A.22})$$

with the auxiliary variables defined as

$$\begin{cases} \mathbf{D}_1 = \mathbf{K}_1(2,2) + \mathbf{K}_2(1,1), \\ \mathbf{D}_2 = \mathbf{K}_2(2,2) + \mathbf{K}_3(1,1), \\ \mathbf{C} = \mathbf{K}_2(2,1) - H(j\omega)e^{jkaL_c}. \end{cases} \quad (\text{A.23})$$

### A.3 Plane wave expansion (PWE)

In this subsection, a PWE method is developed for the special case of the acoustic systems in section 2.1 of Chapter 2. Applying the Fourier transform to variable  $t$  in Eq. (2.49)

yields

$$\frac{\partial}{\partial x} \left[ A \frac{\partial \hat{p}(\omega)}{\partial x} \right] + \frac{\omega^2}{c^2} A \hat{p}(\omega) + j\omega A \hat{Q}(\omega) = 0. \quad (\text{A.24})$$

Hereafter, the frequency dependency of signals will be omitted. Thus,  $(\hat{\cdot}) = f(\mathbf{x}, \omega)$  denotes a variable transformed to the frequency domain via *Fourier* transform.

The *Bloch-Floquet* theorem (Bloch, 1929) for wave propagation in the longitudinal direction of a periodic system is

$$\hat{p} = p_k e^{-jkx}. \quad (\text{A.25})$$

Expanding the periodic function  $p_k$  as a Fourier series yields

$$\hat{p} = e^{-jkx} \sum_{m=-\infty}^{+\infty} \bar{P}_k(g) e^{-jgx} = \sum_{m=-\infty}^{+\infty} \bar{P}_k(g) e^{-j(k+g)x}, \quad (\text{A.26})$$

with  $g = 2\pi m/L_c \forall m \in \mathbb{Z}$ . The section area also can be expanded as Fourier series

$$A = \sum_{\bar{m}=-\infty}^{+\infty} \bar{A}(\bar{g}) e^{-j\bar{g}x}, \quad (\text{A.27})$$

with  $\bar{g} = 2\pi \bar{m}/L_c \forall \bar{m} \in \mathbb{Z}$ .

Applying Eqs. (A.26)-(A.27) on each term of Eq. (A.24):

$$\frac{\partial}{\partial x} \left[ A \frac{\partial \hat{p}}{\partial x} \right] = - \sum_{\bar{m}=-\infty}^{+\infty} \sum_{m=-\infty}^{+\infty} (k+g)(k+g+\bar{g}) \bar{A}(\bar{g}) \bar{P}_k(g) e^{-j(k+g+\bar{g})x}, \quad (\text{A.28})$$

$$A \frac{\omega^2}{c^2} \hat{p} = \frac{\omega^2}{c^2} \sum_{\bar{m}=-\infty}^{+\infty} \sum_{m=-\infty}^{+\infty} \bar{A}(\bar{g}) \bar{P}_k(g) e^{-j(k+g+\bar{g})x}. \quad (\text{A.29})$$

Recalling the non-local feedback law in the frequency domain, with gain  $\gamma$  and  $\hat{Q}(\omega)$  denoting the *Fourier* transform of  $\bar{Q}(t)$ , becomes

$$\hat{Q} = \sum_{n=-\infty}^{+\infty} \frac{\rho_0}{A(x_2)} \gamma H(j\omega) \hat{p}(x_1 + (n-a)L_c) \delta(x - (x_2 + nL_c)), \quad (\text{A.30})$$

since the spatial domain was expanded to infinity, where  $x_2$  is the point of excitation,  $x_1$  is the point of measurement as in Fig. 2.14 and  $H(j\omega)$  depends on the type of gain. For instance,

$$H = 1 \text{ (proportional)}, H = j\omega \text{ (derivative)}, H = \frac{1}{j\omega} \text{ (integrative)} \quad (\text{A.31})$$

The third term in Eq. (A.24) is

$$j\omega A\hat{Q} = j\omega \sum_{\bar{m}=-\infty}^{+\infty} \bar{A}(\bar{g})e^{-j\bar{g}x} \sum_{n=-\infty}^{+\infty} \frac{\rho_0}{A(x_2)} \gamma H(j\omega) \hat{p}(x_1 + (n-a)L_c) \delta(x - (x_2 + nL_c)). \quad (\text{A.32})$$

From *Bloch* wave condition

$$\hat{p}(x_1 + (n-a)L_c) = \hat{p}(x_1) e^{-jk(n-a)L_c}, \quad (\text{A.33})$$

Eq. (A.32) becomes

$$j\omega A\hat{Q} = j\omega \frac{\rho_0}{A(x_2)} \gamma H(j\omega) \hat{p}(x_1) \sum_{\bar{m}=-\infty}^{+\infty} \bar{A}(\bar{g}) e^{-j\bar{g}x} \sum_{n=-\infty}^{+\infty} e^{-jk(n-a)L_c} \delta(x - (x_2 + nL_c)). \quad (\text{A.34})$$

Since  $a \in \mathbb{Z}$  and is constant,

$$\sum_{n=-\infty}^{+\infty} e^{-jk(n-a)L_c} \delta(x - (x_2 + nL_c)) = e^{jkaL_c} \sum_{n=-\infty}^{+\infty} e^{-jknL_c} \delta(x - (x_2 + nL_c)). \quad (\text{A.35})$$

The summation on the right side of Eq. (A.35) holds only if  $x = x_2 + nL_c$ . This is equivalent of sampling the  $f(x) = e^{jkx}$

$$e^{jkaL_c} \sum_{n=-\infty}^{+\infty} e^{-jknL_c} \delta(x - (x_2 + nL_c)) = e^{jkaL_c} e^{-jk(x-x_2)} \sum_{n=-\infty}^{+\infty} \delta(x - (x_2 + nL_c)). \quad (\text{A.36})$$

The Fourier series of the series of Dirac distribution is

$$\sum_{n=-\infty}^{+\infty} \delta(x - (x_2 + nL_c)) = \frac{1}{L_c} \sum_{m=-\infty}^{+\infty} e^{-jg(x-x_2)}. \quad (\text{A.37})$$

Applying Eqs. (A.35)-(A.37) results in

$$j\omega A\hat{Q} = j \frac{\omega \gamma \rho_0 H(j\omega)}{L_c A(x_2)} \hat{p}(x_1) e^{jk(aL_c+x_2)} \sum_{\bar{m}=-\infty}^{+\infty} \sum_{m=-\infty}^{+\infty} \bar{A}(\bar{g}) e^{-jg(x-x_2)} e^{-j(k+\bar{g})x}. \quad (\text{A.38})$$

Also, applying the change of variable  $\tilde{g} = \bar{g} + g$  in Eqs. (A.28), (A.29) and (A.38),

$$\frac{\partial}{\partial x} \left[ A \frac{\partial \hat{p}}{\partial x} \right] = - \sum_{\bar{m}=-\infty}^{+\infty} \sum_{m=-\infty}^{+\infty} (k+g)(k+\tilde{g}) \bar{A}(\tilde{g}-g) \bar{P}_k(g) e^{-j(k+\tilde{g})x}, \quad (\text{A.39})$$

$$A \frac{\omega^2}{c^2} \hat{p} = \frac{\omega^2}{c^2} \sum_{\tilde{m}=-\infty}^{+\infty} \sum_{m=-\infty}^{+\infty} \bar{A}(\tilde{g} - g) \bar{P}_k(g) e^{-j(k+\tilde{g})x}, \quad (\text{A.40})$$

$$j\omega A \hat{Q} = \alpha H(j\omega) \hat{p}(x_1) e^{jk(aL_c+x_2)} \sum_{\tilde{m}=-\infty}^{+\infty} \sum_{m=-\infty}^{+\infty} \bar{A}(\tilde{g} - g) e^{jgx_2} e^{-j(k+\tilde{g})x}, \quad (\text{A.41})$$

with  $\alpha = j \frac{\omega \gamma \rho_0}{L_c A(x_2)}$ . Next, the orthogonality of the exponential function is used in the following manner: multiplying Eqs. (A.39) – (A.41) by  $e^{j\tilde{g}x}$ , dividing by the unit cell length  $L_c$  and integrating over the unit cell after factoring  $e^{-jkx}$  ( $e^{-jkx} \neq 0$ ). Finally, substituting on Eq.(A.24) yields

$$\begin{aligned} & - \sum_{\tilde{m}=-\infty}^{+\infty} \sum_{m=-\infty}^{+\infty} (k+g)(k+\tilde{g}) \bar{A}(\tilde{g}-g) \bar{P}_k(g) \frac{1}{L_c} \int_{-L_c/2}^{L_c/2} e^{-j(\tilde{g}-\bar{g})x} dx + \dots \\ & \dots + \frac{\omega^2}{c^2} \sum_{\tilde{m}=-\infty}^{+\infty} \sum_{m=-\infty}^{+\infty} \bar{A}(\tilde{g}-g) \bar{P}_k(g) \frac{1}{L_c} \int_{-L_c/2}^{L_c/2} e^{-j(\tilde{g}-\bar{g})x} dx + \dots \\ & \dots + \alpha H(j\omega) \hat{p}(x_1) e^{jk(aL_c+x_2)} \sum_{\tilde{m}=-\infty}^{+\infty} \sum_{m=-\infty}^{+\infty} \bar{A}(\tilde{g}-g) e^{jgx_2} \frac{1}{L_c} \int_{-L_c/2}^{L_c/2} e^{-j(\tilde{g}-\bar{g})x} dx = 0. \end{aligned} \quad (\text{A.42})$$

Recalling that, due to the orthogonality previously mentioned, the *Kronecker* delta equals

$$\delta_{\tilde{g}\bar{g}} = \frac{1}{L_c} \int_{-L_c/2}^{L_c/2} e^{j(\tilde{g}-\bar{g})x} dx, \quad (\text{A.43})$$

and it is nonzero only when  $\tilde{g} = \bar{g}$ . Expanding  $\hat{p}(x_1)$ , with  $\hat{g} = 2\pi q/L_c, \forall q \in \mathbb{Z}$  results in

$$\hat{p}(x_1) = \sum_{q=-\infty}^{+\infty} \bar{P}_k(\hat{g}) e^{-j(k+\hat{g})x_1}. \quad (\text{A.44})$$

The series of Eqs. (A.44) and (A.44) can be truncated limiting the indexes to  $m, \bar{m}, q = [-M, M]$ . Thus, Eq. (A.42) becomes

$$\begin{aligned} & - \sum_{m=-M}^M (k+g)(k+\bar{g}) \bar{A}(\bar{g}-g) \bar{P}_k(g) + \frac{\omega^2}{c^2} \sum_{m=-M}^M \bar{A}(\bar{g}-g) \bar{P}_k(g) + \dots \\ & \dots + \alpha H(j\omega) e^{jk(aL_c+x_2)} \sum_{m=-M}^M \bar{A}(\bar{g}-g) e^{jgx_2} \mathbf{U}_M^T \mathbf{P}_M = 0, \end{aligned} \quad (\text{A.45})$$

wherein  $\mathbf{U}_M, \mathbf{P}_M \in \mathbb{R}^{2M+1 \times 1}$  are column matrices containing the terms  $e^{-j(k+\hat{g})x_1}$  and coefficients  $\bar{P}_k(\hat{g})$ , respectively, corresponding to the truncation of Eq. (A.44). Superscript  $T$  indicates the transpose of a matrix.

Eq. (A.45) is valid  $\forall \hat{m}$ . Thus, in matrix form, results in the following eigenvalue problem

$$(\mathbf{K} - \omega^2 \mathbf{M} - j\omega H(j\omega) \mathbf{C}) \mathbf{P}_M = 0, \quad (\text{A.46})$$

where  $\bar{\mathbf{A}}, \mathbf{K}, \mathbf{M} \in \mathbb{R}^{2M+1 \times 2M+1}$  are matrices such that its elements satisfy:  $\bar{A}_{ij} = \bar{A}(\bar{g}_i - g_j)$  and  $K_{ij} = (k + g_j)(k + \bar{g}_i) \bar{A}_{ij}$  and  $M_{ij} = \frac{1}{c^2} \bar{A}_{ij}$ , where  $g_i = 2\pi i / L_c$  is the subscript notation used for  $g$  and  $\bar{g}$ . Matrix  $\mathbf{C} \in \mathbb{R}^{2M+1 \times 2M+1}$  is defined as follows

$$\begin{aligned} \mathbf{C} &= \alpha e^{jk(aL+x_2)} \mathbf{E} \mathbf{U}_M^T, \\ \mathbf{E} &= \begin{bmatrix} \sum_{p=1}^{2M+1} D_{1,p} \\ \vdots \\ \sum_{p=1}^{2M+1} D_{2M+1,p} \end{bmatrix}, \\ \mathbf{D} &= \bar{\mathbf{B}} \circ \bar{\mathbf{A}}, \\ \bar{\mathbf{B}} &= \begin{bmatrix} e^{jx_2g_{-M}} & \dots & e^{jx_2g_M} \end{bmatrix} \otimes \mathbf{1}, \end{aligned}$$

where the symbols  $\circ$  represents the *Hadamard* product,  $\otimes$  the *Kronecker* product and  $\mathbf{1} \in \mathbb{R}^{2M+1 \times 1}$  is a column matrix wherein all entries equals 1.

## APPENDIX B – STABILITY ANALYSIS AND CONTROL OF INFINITE-DIMENSIONAL SYSTEMS

*“I admire the elegance of your method of computation;  
it must be nice to ride through these fields  
upon the horse of true mathematics  
while the like of us have to make our way laboriously on foot.”*  
*(Albert Einstein in correspondence to Tullio Levi-Civita  
during the development of the general theory of relativity)*

This Appendix is a brief introduction to PIEs framework focusing on solving analysis and control problems of distributed-parameter systems. For this aim, numerical results presented as examples in PIETOOLS user manual (Shivakumar *et al.*, 2022) and results available at (Braghini; Peet, 2023) are summarized in the following sections.

## B.1 ODE-PDE systems

In the usual ODE systems, it is usual to parameterize the dynamics by matrices, which form a computationally tractable algebraic structure. This approach is called state space representation and is the base of modern control techniques. The general form of a dynamic equation is,  $\forall t \in \mathbb{R}_{\geq 0}$ ,

$$\dot{x}(t) = Ax(t) + B_1w(t) + B_2u(t),$$

where the state vector  $x(t) \in \mathbb{R}^{nx}$  is an element of a finite-dimensional vector space, called the state space,  $u(t) \in \mathbb{R}^{nu}$ , is the controlled part of the input,  $w(t) \in \mathbb{R}^{nw}$  is the exogenous part of the input, and  $A, B_1, B_2$  are linear operators between the finite-dimensional vector spaces, which all have matrix representation.

Also, one may write a regulated equation as

$$z(t) = C_1x(t) + D_{11}w(t) + D_{12}u(t),$$

which the regulated output  $z(t) \in \mathbb{R}^{nz}$  and the operators  $C_1, D_{11}, D_{12}$  also having matrix representation.

Aiming to expand this approach to a 1D PDE system, one comes to the following representation

$$\begin{aligned} \dot{\phi}(t) &= \mathcal{A}\phi(t) + \mathcal{B}_1w(t) + \mathcal{B}_2u(t), \\ z(t) &= C_1\phi(t) + \mathcal{D}_{11}w(t) + \mathcal{D}_{12}u(t), \end{aligned} \tag{B.1}$$

where  $\phi(t) \in X$  is an element of an infinite-dimensional vector space  $X \subset L_2^{np}[a, b]$ , such that elements of  $X$  must also satisfy suitable boundary conditions and the continuity constraints related to the spatial partial derivatives contained in the dynamics (Peet, 2021a; Peet, 2021b). To cover a larger class of infinite-dimensional systems, including the TDS systems used in the final section, the next sections will treat a wider class of operators  $\mathcal{A}, \mathcal{B}_1, \mathcal{B}_2, C_1, \mathcal{D}_{11}, \mathcal{D}_{12}$  that are,

in general, differential operators not numerically parameterized. To get around this problem, allowing the formulation of numerically tractable problems for infinite-dimensional systems, it was shown that, for a large number of ODE-PDE systems, a state transformation  $\phi(t) = \mathcal{T}\varphi(t)$  is able to incorporate the constraints of  $X$  on the new state  $\varphi(t) \in L_2^{np}[a, b]$  (Shivakumar *et al.*, 2019).

These are the basis of a new representation of ODE-PDE systems, parametrized by a special class of operators, which form an algebraic structure akin to matrices. With this representation, numerically tractable problems called LPIs are formulated.

## B.2 PI Operators for 1D ODE-PDE systems

In this Section, 1D PI operators, a special class of operators that can be represented in PIETOOLS using *opvar* class objects, are presented. An operator  $\mathcal{P}$  is a 1D PI operator if it acts on functions  $\mathbf{v}(s)$  depending on just one spatial variable  $s$ , and the operation it performs can be described using partial integrals. Let's first define 3-PI operators, acting on functions  $\mathbf{v} \in L_2^n[a, b]$ , and then more general 4-PI operators, acting on functions  $\begin{bmatrix} v_0 \\ \mathbf{v}_1 \end{bmatrix} \in \begin{bmatrix} \mathbb{R}^{n_0} \\ L_2^{n_1}[a, b] \end{bmatrix}$ . 3-PI operators are enough to parameterize the PIE formulation of PDE systems, whereas 4-PI operators parameterize a more general ODE-PDE class of systems.

Take the matrix valued polynomials  $R_0 : [a, b] \rightarrow \mathbb{R}^{m,n}$ ,  $R_1, R_2 : [a, b] \times [a, b] \rightarrow \mathbb{R}^{m,n}$ . The associated 3-PI operator  $\mathcal{P}[R] : L_2^n[a, b] \rightarrow L_2^m[a, b]$  is given by

$$(\mathcal{P}[R]\mathbf{v})(s) = R_0(s)\mathbf{v}(s) + \int_a^s R_1(s, \theta)\mathbf{v}(\theta)d\theta + \int_s^b R_2(s, \theta)\mathbf{v}(\theta)d\theta, \quad s \in [a, b]. \quad (\text{B.2})$$

Now, take  $P : \mathbb{R}^{m_0 \times n_0}$ ,  $Q_1 : [a, b] \rightarrow \mathbb{R}^{m_1 \times n_0}$ ,  $Q_2 : [a, b] \rightarrow \mathbb{R}^{m_0 \times n_1}$  and 3-PI parameters  $R = \{R_0, R_1, R_2\}$ . The associated 4-PI operator is  $\mathcal{P} \begin{bmatrix} P & Q_1 \\ Q_2 & R \end{bmatrix} : \begin{bmatrix} \mathbb{R}^{n_0} \\ L_2^{n_1}[a, b] \end{bmatrix} \rightarrow \begin{bmatrix} \mathbb{R}^{m_0} \\ L_2^{m_1}[a, b] \end{bmatrix}$

$$\left( \mathcal{P} \begin{bmatrix} P & Q_1 \\ Q_2 & R \end{bmatrix} \mathbf{v} \right)(s) = \begin{bmatrix} Pv_0 & + \int_a^b Q_1(s)\mathbf{v}_1(s)ds \\ Q_2(s)v_0 & + (\mathcal{P}[R]\mathbf{v}_1)(s) \end{bmatrix}, \quad s \in [a, b],$$

for  $\mathbf{v} = \begin{bmatrix} v_0 \\ \mathbf{v}_1 \end{bmatrix} \in \begin{bmatrix} \mathbb{R}^{n_0} \\ L_2^{n_1}[a, b] \end{bmatrix}$ .

### B.3 PIE representation of ODE-PDE systems

A PIE representation of an ODE-PDE system with inputs and outputs is generally defined as shown below,

$$\begin{aligned}\mathcal{T}\dot{\varphi}(t) + \mathcal{T}_w\dot{w}(t) + \mathcal{T}_u\dot{u}(t) &= \mathcal{A}\varphi(t) + \mathcal{B}_1w(t) + \mathcal{B}_2u(t), \quad \varphi(0) = \varphi_0 \in \mathbb{R}^{n_x} \times L_2^{n_p}(a, b) \\ z(t) &= \mathcal{C}_1\varphi(t) + \mathcal{D}_{11}w(t) + \mathcal{D}_{12}u(t), \\ y(t) &= \mathcal{C}_2\varphi(t) + \mathcal{D}_{21}w(t) + \mathcal{D}_{22}u(t),\end{aligned}\tag{B.3}$$

where the signals are the state  $\varphi(t) \in \mathbb{R}^{n_x} \times L_2^{n_p}(a, b)$ , exogenous input  $w(t) \in \mathbb{R}^{n_w}$ , controlled input  $u(t) \in \mathbb{R}^{n_u}$ , regulated output  $z(t) \in \mathbb{R}^{n_z}$  and measured output  $y(t) \in \mathbb{R}^{n_y}$ . All the 12 operators of the PIE representation have an equivalent 4-PI operator representation.

### B.4 PIETOOLS: A Toolbox for Analysis and Control of Infinite-Dimensional Systems

PIETOOLS 2022 provides an intuitive environment for the control of ODE-PDE models, requiring a handful of mathematical details about the PIE operators from the user. In this section, this will be exemplified with an example extracted from PIETOOLS 2022 user manual (Shivakumar *et al.*, 2022).

Given a coupled ODE-PDE model, suppose that ODE dynamics is given by

$$\dot{x}(t) = -x(t) + u(t),\tag{B.4}$$

with controlled input  $u$ , and PDE dynamics given by

$$\ddot{\mathbf{x}}(t, s) = c^2\partial_s^2\mathbf{x}(t, s) - b\partial_s\mathbf{x}(t, s) + sw(t), s \in (0, 1), t \geq 0,\tag{B.5}$$

which is the one-dimensional wave equation with velocity  $c$ , added viscous damping coefficient  $b$  and external disturbance  $w$ . Since the PDE has a second-order derivative in time, one should make a change of variables to appropriately define a state space. Call  $\phi = (\partial_s\mathbf{x}, \dot{\mathbf{x}})$ . Thus the PDE part of the dynamic equation becomes

$$\dot{\phi}(t, s) = \begin{bmatrix} 0 & 1 \\ c & 0 \end{bmatrix} \partial_s\phi(t, s) + \begin{bmatrix} 0 & 0 \\ 0 & -b \end{bmatrix} \phi(t, s) + \begin{bmatrix} 0 \\ s \end{bmatrix} w(t), s \in (0, 1), t \geq 0.\tag{B.6}$$

Now, add to the system a regulated output equation, for instance

$$z(t) = \begin{bmatrix} r(t) \\ u(t) \end{bmatrix},\tag{B.7}$$

where  $r(t) = \int_0^1 \begin{bmatrix} 1 & 0 \end{bmatrix} \phi(t, s) ds = \mathbf{x}(t, s = 1) - \mathbf{x}(t, s = 0)$ . Adding  $u$  to the regulated output is a way of obtaining this signal from simulations.

To define these models, let's first create the following variables in MATLAB using the `state()` class:

```
>> x = state('ode');   phi = state('pde', 2);
>> w = state('in');    u = state('in');
>> z = state('out', 2)
```

Then, one can define/add equations to this `sys()` object using standard operations, such as `+`, `-`, `*`, `\diff`, `\subs`, `\int`, etc., as shown below.

```
>> odepde = sys();
>> eq_dyn=[diff(x,t,1)==-x+u
diff(phi,t,1)==[0 1; c 0]*diff(phi,s,1)+[0;s]*w+[0 0;0 -b]*phi];
>>eq_out=z==[int([1 0]*phi,s,[0,1]) u];
>>odepde=addequation(odepde,[eq_dyn;eq_out]);

    Initialized sys() object of type "pde"

    5 equations were added to sys() object
```

Whenever, equations are successfully added to the `sys()` object, a text message confirming the same is displayed in the command output window, as shown above. To verify if PIETOOLS got the right equations, the user just needs to type the system variable (“odepde” in this example) on the command window for PIETOOLS to display the added equations.

Since our system has a controlled input, which could have any name, onw must pass this information to PIETOOLS. This is done by the following command:

```
>> odepde=setControl(odepde,[u]);

    1 inputs were designated as controlled inputs
```

Similarly, observed outputs also need to be specified. Consider, for instance,

$$y(t) = r(t). \quad (\text{B.8})$$

Then the corresponding commands are

```

» y=state('out');
» eq_y=y==int([1 0]*phi,s,[0,1]);
» odepde=setObserve(odepde,[y]);

      1 equations were added to sys() object
      1 inputs were designated as observed output

```

Any PDE model requires appropriate boundary conditions to be well-conditioned. For example, take the following Dirichlet,

$$\dot{\mathbf{x}}(t, s = 0) = 0,$$

and Neuman,

$$\partial_s \mathbf{x}(t, s = 1) = x(t),$$

boundary conditions. These are incorporated to the model by the commands

```

» bc1 = [0 1]*subs(phi,s,0) == 0;
» bc2 = [1 0]*subs(phi,s,1) == x;
» odepde = addequation(odepde,[bc1;bc2]);

      2 equations were added to sys() object

```

One of the first things a user may need to do is to simulate the system. In PIETOOLS, simulations of linear ODE-PDE coupled systems are made by projection onto a finite-dimensional vector space spanned by Chebyshev polynomials with the command:

```
| » solution = PIESIM(odepde, opts, uinput, ndiff);
```

For instance, suppose, one wants to simulate the ODE-PDE model corresponding to (B.4) and (B.6) with constant velocity  $c = 1$ , damping coefficient  $b = 0.1$ , under the previously defined boundary conditions, and a specific choice of disturbance  $w(t)$ . In particular, take the problem of simulating the effect of  $w(t)$  on  $\dot{\mathbf{x}}$  and the value  $\mathbf{x}(t, s = 1) - \mathbf{x}(t, s = 0)$  given by the previously defined output.

To run this simulation in PIESIM, use the following `opts` to the function, which commands PIESIM to don't automatically plot the solution, to use 8 Chebyshev polynomials, to simulate the solutions up to  $t = 1s$  with a time-step of  $10^{-2}s$ , and to use Backward Differentiation Formula (BDF):

```

>opts.plot = 'no';
>opts.N = 8;
>opts.tf = 10;
>opts.dt = 1e-2;
>opts.intScheme=1;

```

PIESIM also requires information regarding the initial conditions and external perturbations. This is done as follows, for the zero-state response of the system perturbed by an exponentially decaying sinusoidal signal:

```

>uinput.ic.PDE = [0,0];
>uinput.ic.ODE = 0;
>uinput.u=0;
>uinput.w = sin(5*st)*exp(-st);

```

Note that the control input must also be zero since an open-loop response is to be simulated. The last argument is regarding the space differentiability of the states. In this example, the PDE state involves 2 first order differentiable state variables and this is passed through the input `ndiff` as:

```

| >ndiff = [0,2,0];

```

PIESIM gives discretized time-dependent arrays corresponding to the time vector used in the simulations and the resulting state variables and output. The result is depicted in Figures B.2 and B.1.

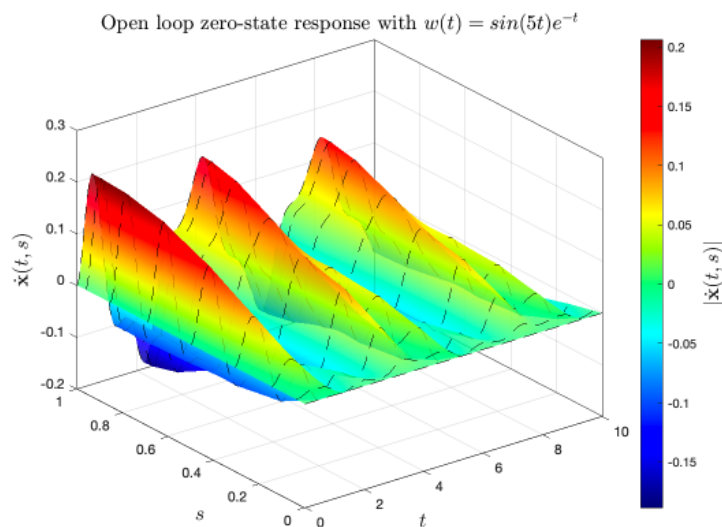


Figure B.1 – Transient response of the state variable  $\dot{x}(t, s)$  by simulating the ODE-PDE model (B.4) and (B.6) with  $u(t) = 0$  for external disturbance  $w(t) = \sin(5t)e^{-t}$ .

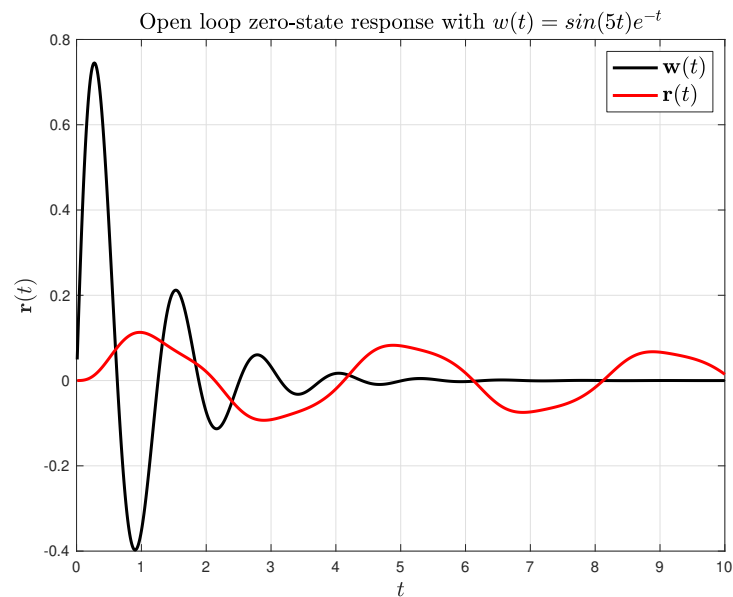


Figure B.2 – Transient response  $r(t)$  of the ODE-PDE model (B.4) and (B.6) with  $u(t) = 0$  for external disturbance  $w(t) = \sin(5t)e^{-t}$ .

Apart from simulation, you may be interested in knowing whether the model is internally stable or not. Moreover, what would be a good control input such that the effect of external disturbances for a specific choice of output can be suppressed? In PIETOOLS, such an analysis and synthesis are typically performed by first converting the ODE-PDE model to a new representation called Partial Integral Equations (PIEs), which is parameterized by a special class of operators, and then solving convex optimization problems.

Thus, PIEs are an equivalent representation of ODE-PDE models which provide a convenient and efficient way to analyze ODE-PDE models by numerically treatable methods. The conversion from the original system to the PIE representation is simply done using the following command, resulting in the next output on the command window (considering that every previous step was correctly done):

```

>>PIE = convert(odepde,'pie');

    --- Reordering the state components to allow for representation as PIE ---

The order of the state components x has not changed.

    --- Converting ODE-PDE to PIE ---
Initialized sys() object of type ``pde``
Conversion to pie was successful

```

Once the model is converted to a PIE, analysis, and control can be performed by calling one of the executive functions. There are plenty of executive functions available, starting from stability, computing  $H_\infty$  and  $H_2$  gain,  $H_\infty$  optimal state estimator, as well as  $H_\infty$  state feedback controllers.

For this example, the system is asymptotically stable only when  $b > 0$ . This can be shown by calling the executive after one of the following predefined settings had been chosen: extreme, stripped, light, heavy, veryheavy, or custom. A detailed description of the optimization settings may be found in the user manual.

```
| »settings = lpisettings('heavy');
| »[prog, P] = PIETOOLS_stability(PIE, settings);
```

If the resultant optimization problem can be solved with these settings, the following message will be displayed after the optimization outputs:

```
| The System of equations was successfully solved.
```

which provides an exponential stability certificate for the system.

Now, if one wants to improve the system's rejection of disturbances, the optimal solution is to design a state-feedback controller that provides a control input  $u(t)$  to be applied in (B.4), which minimizes the  $H_\infty$  norm of the closed-loop system, provided that such a controller exists. To compute this performance measurement on the open loop, one just need to call the executive:

```
| » [prog, P, gamma] = PIETOOLS_Hinf_gain(PIE, settings);
```

Provided, again, that the optimization problem can be solved, the command window output will display the  $H_\infty$  norm. In this example, the output is given as follows:

```
| The H-infty norm of the given system is upper bounded by:
| 5.1631
```

For PIETOOLS to synthesize a state feedback controller that minimizes this metric, one needs to call a third executive:

```
| » [prog, Kval, gam_val] = PIETOOLS_Hinf_control(PIE, settings);
```

which will make PIETOOLS search for the operator  $\mathcal{K}$  stored in variable `Kval` corresponding to the controller, and display the closed loop  $H_\infty$  norm if succeeded. For this example, the result is a great increase in performance, in terms of this metric:

```
The closed-loop H-infty norm of the given system is upper bounded by:
0.9779
```

The controller is generally a 4-PI linear operator, which has an image parameterized by matrix-valued polynomials. The resultant controller can be displayed by entering its variable name on the command window.

One may again use PIESIM to simulate the response of the resultant closed-loop system, as depicted in Figs. B.3 and B.4. The reader is encouraged to look at the file `DEMO1_Simple_Sta` included in the `PIETOOLS_demos` folder of PIETOOLS, which provides a complete guide to reproduce the results described and depicted on this section.

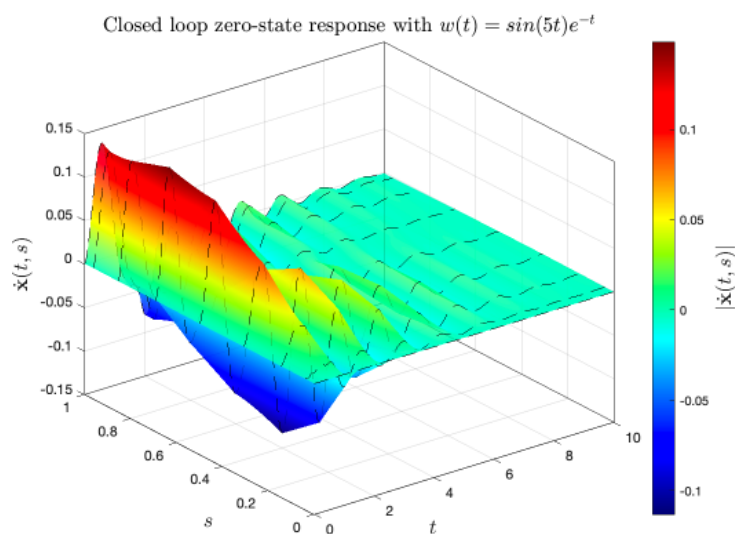


Figure B.3 – Transient response of the state variable  $\dot{\mathbf{x}}(t, s)$  on the closed-loop system for external disturbance  $w(t) = \sin(5t)e^{-t}$ .

In this chapter, an introduction to how PIETOOLS can be used to solve various control-relevant problems involving linear ODE-PDE models was presented. The example depicted here was highly sensitive to disturbances infinite-dimensional system. Figures. B.1 and. B.2 show that, even after the applied disturbance has ceased, the output signal  $r(t)$  remains affected, taking more time than the final time of the presented simulation to reject the disturbance. This behavior is measured by the computed  $H_\infty$  norm of the open-loop system.

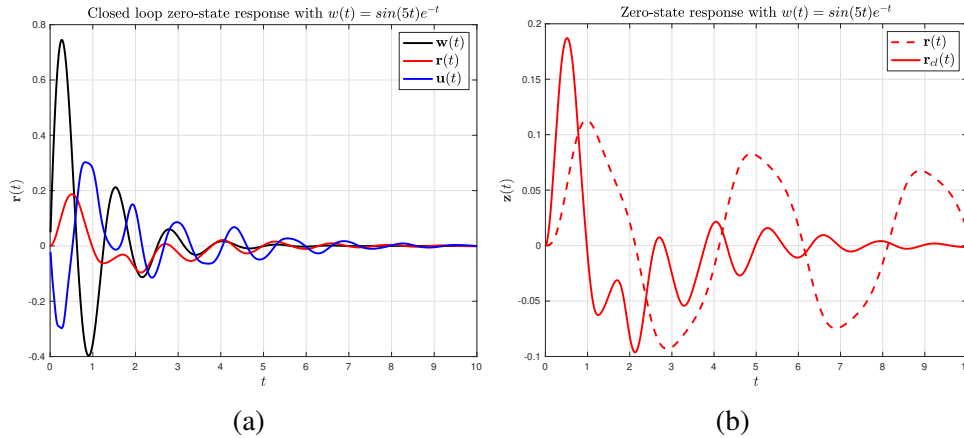


Figure B.4 – (a) Transient response of the output  $r(t)$  and controlled input  $u(t)$  of the closed-loop system for external disturbance  $w(t) = \sin(5t)e^{-t}$ . (b) Transient response of the output  $r(t)$  and controlled input  $u(t)$  of the closed-loop system for external disturbance  $w(t) = \sin(5t)e^{-t}$ .

On the other hand, with the synthesized feedback controller given by PIETOOLS, the closed-loop system quickly rejects the disturbance, as is clear from Figures. B.3 and. B.4. The increase in performance can be certified by the considerable reduction in the value of the  $H_\infty$  norm and by comparing the behavior of the outputs without and with the controller, in Figure. B.4 (b).

## B.5 $H_2$ Norm: A Metric for Initial-Condition to Output Performance

Having introduced the PIEs framework and PIETOOLS, in this section, let's summarize a theoretical work presented at (Braghini; Peet, 2023). This work provides a numerically tractable formulation for the problem of measuring the  $H_2$  norm of ODE-PDE and time-delay (TDS) systems. First, the  $H_2$  norm problem is introduced, reviewing the current literature in infinite-dimensional systems to finally present a resultant optimization problem that is used to solve some numerical examples.

The input-output properties of a linear system admit many characterizations, including small gain, passivity, Bounded Input Bounded Output Stability, Input-to-State Stability,  $H_\infty$  norm, and  $H_2$  norm. Of these, however, the  $H_2$ -norm is arguably the most well-established metric for system performance – defining white noise amplification, the mean energy of the impulse response, and gain from initial condition to output. Furthermore, the  $H_2$ -optimal control is the generalization of the classical Linear Quadratic Regulator (LQR) and Linear Quadratic Gaussian (LQG). While in the context of robust control, the  $H_2$  norm has been largely supplanted

by the  $H_\infty$  norm, the  $H_2$  norm still commonly appears in mixed-norm optimization problems where the goal is to improve performance while maintaining robustness with respect to model uncertainty – See, e.g. (Iwasaki, 1994) and (Scherer *et al.*, 1997). Unfortunately, despite the significance of the  $H_2$ -norm in analysis and control problems, and unlike in the finite-dimensional case, there are few (if any) results in the literature regarding the computation of *provable bounds* on the  $H_2$  norm for delayed and Partial Differential Equation (PDE) input-output systems.

The most common alternative to finding provable bounds on the  $H_2$  norm for infinite-dimensional systems is to approximate it numerically through some form of discretization – using so-called early or late lumping methods.

For early lumping methods, the most common approach is to project the system state onto a finite-dimensional subspace using methods such as Galerkin (for PDEs) or to represent the transcendental delay term using a Padé approximation (for delayed systems). These approaches result in an ODE which may be analyzed or controlled using standard computational approaches as in (Zhao *et al.*, 1978; Morris *et al.*, 2015) (for PDEs) and (Pekar; Kureckova, 2011) (for delayed systems).

Focusing on late-lumping methods, there exist operator-valued versions of both the Ricatti equation and Lyapunov equation characterization of the  $H_2$  norm – primarily for delay systems.

However, because the operators that define the Ricatti or Lyapunov equation are unbounded and do not form an algebra, the Ricatti equation is not easily solved without first projecting onto a finite-dimensional space. For example, by numerically solving the operator *Lyapunov* equation, numerical estimates of the  $H_2$ -norm of delayed linear systems of both retarded and neutral type were found in (Mattenet *et al.*, 2022) and efficient algorithms for larger scale delay systems were considered in (Michiels; Zhou, 2019). Alternatively, in the special case of commensurate delays, the delay system can be exactly reduced to an ODE, as was considered in (Jarlebring *et al.*, 2011).

Finally, in the special case of TDS systems, it is possible to obtain an analytical expression for the transfer function of the system, which is meromorphic. In many cases, it becomes possible to upper-bound the resulting chains of poles – yielding accurate stability analysis results like in (Fioravanti *et al.*, 2012).

To allow numerically tractable methods to be applied, let's rely on the PIE framework and the special class of PI operators. Assuming that the system is restricted to: finite-

dimensional inputs and outputs; inputs within the domain of PDEs, or on the finite-dimensional part of general ODE-PDEs, which excludes systems with boundary control; and has no algebraic delay terms – as exhibited by NDSs – the existence of a unitary map between the original system and the corresponding PIE can be shown. The resultant PIE representation is then used to derive our main result, a LPI for the computation of an upper bound to the  $H_2$  norm of the original system. By using polynomial methods, this LPI translates into a SDP.

**Theorem 9.** *Take the system B.1 defined by  $\{\mathcal{A}, \mathcal{B}_1, \mathcal{C}_1 X\}$ , with  $\mathcal{D}_{11} = 0$ ,  $u = 0 \in L_2^{nu}[0, \infty)$ . Suppose this system is observable. Let  $\mathcal{T}, \mathcal{A}, \mathcal{C}_1$  be 4-PI operators as defined in B.3, then  $\exists \mathcal{T} : \mathbb{R}^{n_x} \times L_2^{np}[a, b] \rightarrow X$ , and  $\mathcal{A} = \mathcal{A}\mathcal{T}$ ,  $\mathcal{C}_1 = \mathcal{C}_1\mathcal{T}$ ,  $\mathcal{B}_1 = \mathcal{B}_1$ . Moreover, there is a differential operator,  $\mathcal{D}$  such that  $\mathcal{T}\mathcal{D}\phi = \phi$  and  $\mathcal{D}\mathcal{T}\varphi = \varphi$  for any  $\phi \in X$  and  $\varphi \in \mathbb{R}^{n_x} \times L_2^{np}[a, b]$ .*

*One says  $\mu$  is the  $H_2$  norm of System B.1 defined as*

$$\mu := \sup_{\|\mathbf{w}_0\|_2=1} \|z\|_{L_2}, \quad s.t.$$

*$\{\phi, z\}$  is the solution of the system*

*for some initial condition  $\mathcal{B}_1\mathbf{w}_0$  and zero input.*

*Finally, suppose there is a positive definite PI operator  $W_0 \succ 0$  such that:*

$$\begin{aligned} \text{trace}(\mathcal{B}_1^* W_0 \mathcal{B}_1) &< \gamma^2, \\ \mathcal{A}^* W_0 \mathcal{T} + \mathcal{T}^* W_0 \mathcal{A} + \mathcal{C}_1^* \mathcal{C}_1 &\prec 0. \end{aligned} \tag{B.9}$$

*Then the system B.1 is internally stable and, if  $\{\phi, z\}$  satisfies B.1 for some initial condition  $\mathcal{B}_1\mathbf{w}_0$  and zero input, one has that  $\|z\|_{L_2} < \gamma\|\mathbf{w}_0\|_2$ , implying that  $\mu \leq \gamma$ .*

**Proof 1.** *The proof can be found in (Braghini; Peet, 2023). □*

The above theorem can be translated into a convex optimization problem thanks to the parametrization of PI operators by polynomial matrices. This occurs because the semi-positivity of polynomials can be relaxed to the restriction of the polynomial being of some of the squares (SOS) class (see (Prajna *et al.*, 2002)).

Thus, as detailed in the full paper, one may derive an optimization problem that seeks the operator  $\mathcal{W}_\gamma$  that minimizes the upper bound  $\gamma$ , with the additional restrictions of B.9. This kind of program can be easily implemented in PIETOOLS and if this problem is feasible, the optimal value of  $\gamma$  approximates the norm  $\mu$ . By solving this program for the numerical examples of the next section, the applicability of PIETOOLS to theoretical results is illustrated.

## B.6 Numerical examples of the $H_2$ norm

In this section, an optimization problem derived from Theorem 1 is applied to some delayed (ODE-PDE) and PDE systems. In each case, the PIE representation is constructed using the formulae in (Peet, 2021a) and (Peet, 2021b). Although there are very few analytic expressions for the  $H_2$  norm of delayed and PDE systems in the literature, the accuracy of the proposed algorithm can be estimated by comparing with approximation schemes such as that proposed in (Jarlebring *et al.*, 2011) based on a projection of the delay-Lyapunov Equation. This comparison was done on the aforementioned submitted paper.

The computed bound on the  $H_2$ -norm is obtained by first using PIETOOLS 2021b to construct the PIE representation. Then, the conditions of Theorem 1 are enforced using `poslpivar` to create an operator variable  $W_0$  and the PIETOOLS `lpi_ineq` command to enforce the inequality constraints. For both of these steps, the PIETOOLS ‘heavy’ settings were used.

**Example 1.** *First consider the scalar, single delay ( $\tau$ ) system*

$$\begin{aligned}\dot{x}(t) &= -ax(t - \tau) + bu(t), \\ y(t) &= cx(t),\end{aligned}$$

where  $a, b, c, > 0$ . This system has an analytic expression for the  $H_2$  norm, detailed on (Jarlebring *et al.*, 2011). For computation, let’s take values  $a = 1$ ,  $b = 2$ ,  $c = 2$ , and  $\tau = 0.5$ , for which the system is open-loop stable. The computed value is 3.6726, whereas the analytic solution is 3.6724.

**Example 2.** *Next, consider the two-delay system*

$$\dot{x}(t) = A_0x(t) + A_1x(t - \tau_1) + A_2x(t - \tau_2) + Bu(t), y(t) = Cx(t)$$

For numerical testing, let’s take  $\tau_1 = \pi/10$ ,  $\tau_2 = 1$ , so that the delays are incommensurate and

$$\begin{aligned}A_0 &= \begin{bmatrix} -1 & 1 & 2 \\ 1 & -3 & 2 \\ 0 & 0 & -1 \end{bmatrix}, & A_1 &= \frac{1}{5} \begin{bmatrix} -3 & 0 & 1 \\ 1 & -2 & 0 \\ 0 & 2 & -2 \end{bmatrix}, \\ A_2 &= \frac{1}{5} \begin{bmatrix} -4 & 1 & 0 \\ 0 & -2 & 1 \\ 2 & 1 & -3 \end{bmatrix}, & B &= \begin{bmatrix} 1 \\ 1 \\ 1 \end{bmatrix}, & C &= \begin{bmatrix} 1 & 1 & 1 \end{bmatrix}\end{aligned}$$

In this case, the method described in (Jarlebring et al., 2011) gives 3.8299 whereas our Theorem gives 3.8304.

**Example 3.** Consider a system modeled using PDEs with two incommensurate delays,  $\tau_1 = 0.25$ ,  $\tau_2 = 0.3$ , and  $h = \frac{\pi}{10}$ . The spatial domain is  $x \in [0, \pi]$ . The dynamics are as follows.

$$\begin{aligned} \frac{\partial \xi}{\partial t} &= \frac{\partial^2 \xi}{\partial x^2} - 20\xi(x, t) - 4\xi(x, t - \tau_1) \dots \\ &\quad \dots - 0.1\xi(x, t - \tau_2) + \mathbf{1}(x)u(t), \\ \xi(0, t) &= 0, \xi(\pi, t) = 0, \\ y(t) &= \frac{1}{h} \int_0^\pi \xi(x, t) dx. \end{aligned}$$

For this system, of course, there is neither an analytical expression nor a numerical method available to compute the  $H_2$  norm without performing a spatial discretization. However, this system admits a 2D PIE representation using the result in (Jagt; Peet, 2022b) (An extension of the PIE framework). The bound on the  $H_2$ -norm for this system is 2.3236.

**Example 4.** (Example (3), discretized) For the last example, let's consider the question of whether discretization of the PDE in Example (3) yields accurate estimates of the  $H_2$ -norm of the delayed PDE. Specifically, a finite-difference discretization of the last example is used, taking the spatial domain  $\bar{\Omega} = [0, \pi]$  and dividing it in  $n_e$  equally spaced of  $\frac{\pi}{n_e}$  disjoint subdomains such that  $\Omega_1 \cup \Omega_2 \cup \dots \cup \Omega_{n_e}$ , each with associated lumped state,  $v_i$ . The resulting system of delayed ODEs is given by

$$\begin{aligned} \dot{v}(t) &= (T + D_0)v(t) + D_1v(t - \tau_1) + D_2v(t - \tau_2) + B_2u(t) \\ y(t) &= C_2v(t) \end{aligned}$$

where

$$T = \frac{(n_e + 1)^2}{\pi^2} \begin{bmatrix} -2 & 1 & 0 & \dots & 0 \\ 1 & -2 & 1 & \dots & 0 \\ \vdots & \ddots & \ddots & \ddots & \\ 0 & \dots & & 1 & -2 \end{bmatrix} \in \mathbb{R}^{n_e \times n_e},$$

and

$$\begin{aligned}
 D_0 &= \begin{bmatrix} -20 & 0 & 0 \\ 0 & \ddots & 0 \\ 0 & 0 & -20 \end{bmatrix}, & D_1 &= \begin{bmatrix} -4 & 0 & 0 \\ 0 & \ddots & 0 \\ 0 & 0 & -4 \end{bmatrix}, \\
 D_2 &= \begin{bmatrix} -.1 & 0 & 0 \\ 0 & \ddots & 0 \\ 0 & 0 & -.1 \end{bmatrix}, & C_2 &= [1 \ 1 \ \dots \ 1] \in \mathbb{R}^{1 \times n_e}, \\
 & & B_2 &= [1 \ 1 \ \dots \ 1]^T \in \mathbb{R}^{n_e \times 1}.
 \end{aligned}$$

For this delayed ODE discretization of the delayed PDE, tests were performed at 10 discretization points. The bound can be computed as 1.3939 using our Theorem and 1.3696 using the method in ([Jarlebring et al., 2011](#)).

## APPENDIX C – CONCEPT OF AN EXPERIMENTAL REALIZATION

*“I have been impressed with the urgency of doing. Knowing is not enough; we must apply.*

*Being willing is not enough; we must do.”*

*(Leonardo Da Vinci)*

The proposed experimental platform is an electroacoustic duct system with microphones and speakers connected by feedback control interactions; these interactions are periodically constructed along the duct and implemented through a specific circuit. The circuit is shown in the Annex, whereas a scheme is displayed in Fig. C.2; it includes low-pass filters, high-pass filters, proportional, integral, derivative, and double-derivative feedback circuits built with operational amplifiers. The different types of feedback are selected via switching keys that also allow for combination, like in PID control.

For each unit cell, DC-DC Converters are required for microphone conditioning, ensuring the proper voltage and current levels for the microphone to operate. Moreover, the low-pass filters are set to a cutoff frequency of  $1500\text{Hz}$  and designed as 8-th-order *Butterworth* filters. One filter is placed between the microphone and the main circuit, and another one between the main circuit and the speaker. For the controllers, feedback gains are set with potentiometers and switches, allowing the activation of one or more feedback loops as well as the choice of feedback between positive and negative. As for the high-pass filters, they are also 8-th-order *Butterworth* filters, but their cut-off frequency is set to  $10\text{Hz}$ . These are placed in series with the integrator branch of the circuit. Finally, an audio amplifier circuit was built with a TDA2040.

The duct in Fig. C.1a represents one cell with spaces to insert microphones (sensors) and speakers (actuators); the microphones on the top right of Fig. C.1b are the ones used on the feedback loop together with the speakers shown on the left. Additionally, instrumentation microphones from Bruel& Kjaer 4958 were used to characterize the sensors and actuators. The controller may alternatively be implemented using a DSPACE board or microcontrollers for a digital implementation. The analogy implementation using operational amplifiers was designed by Diego Siviero and Fernando Ortolano and is available in Annex A.

This setup allows for various configurations of feedback control to study their effects on the dynamics of the acoustic duct as predicted by the topology presented in Chapter 2. A preprint was published by LVA with numerical results of the electroacoustic setup (Braghini *et al.*, 2022) showing that the stability of this system is an important problem to be addressed in future works. It is notable that a recent work of another research group realized a similar experiment independently of our vision (Maddi *et al.*, 2024).



Figure C.1 – Acoustic duct to be used as an experimental platform (a) with the electroacoustic components in (b).

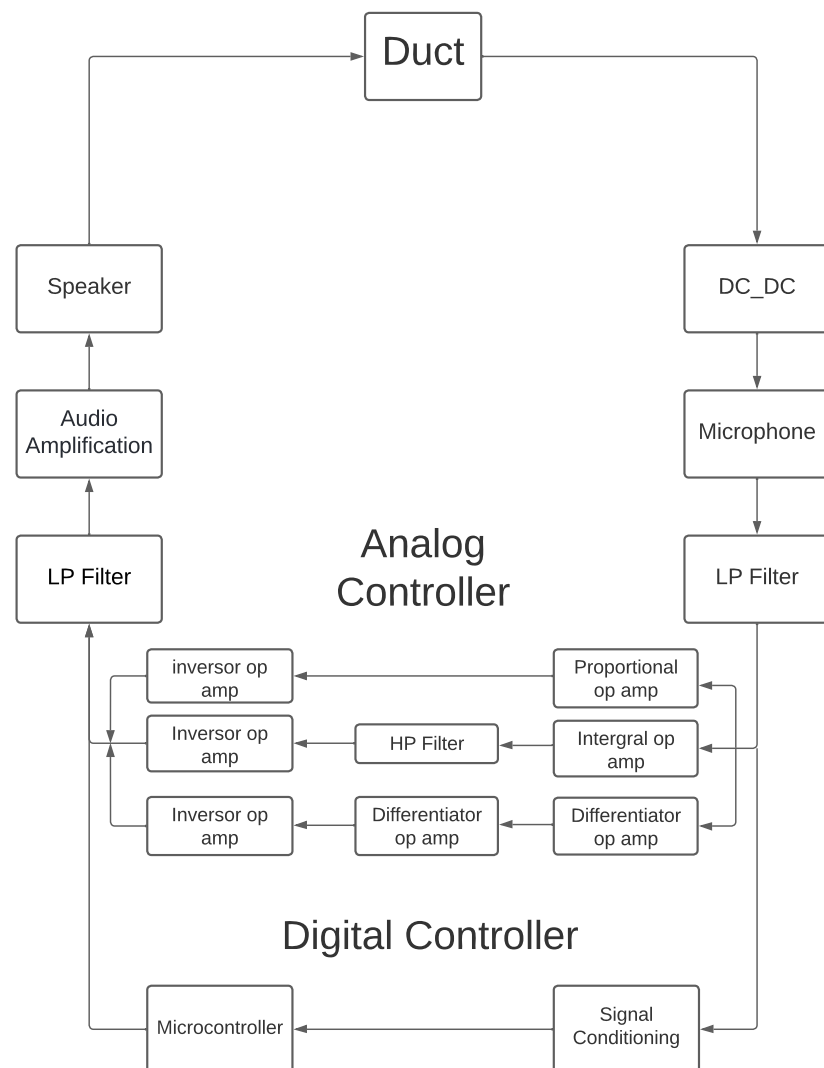
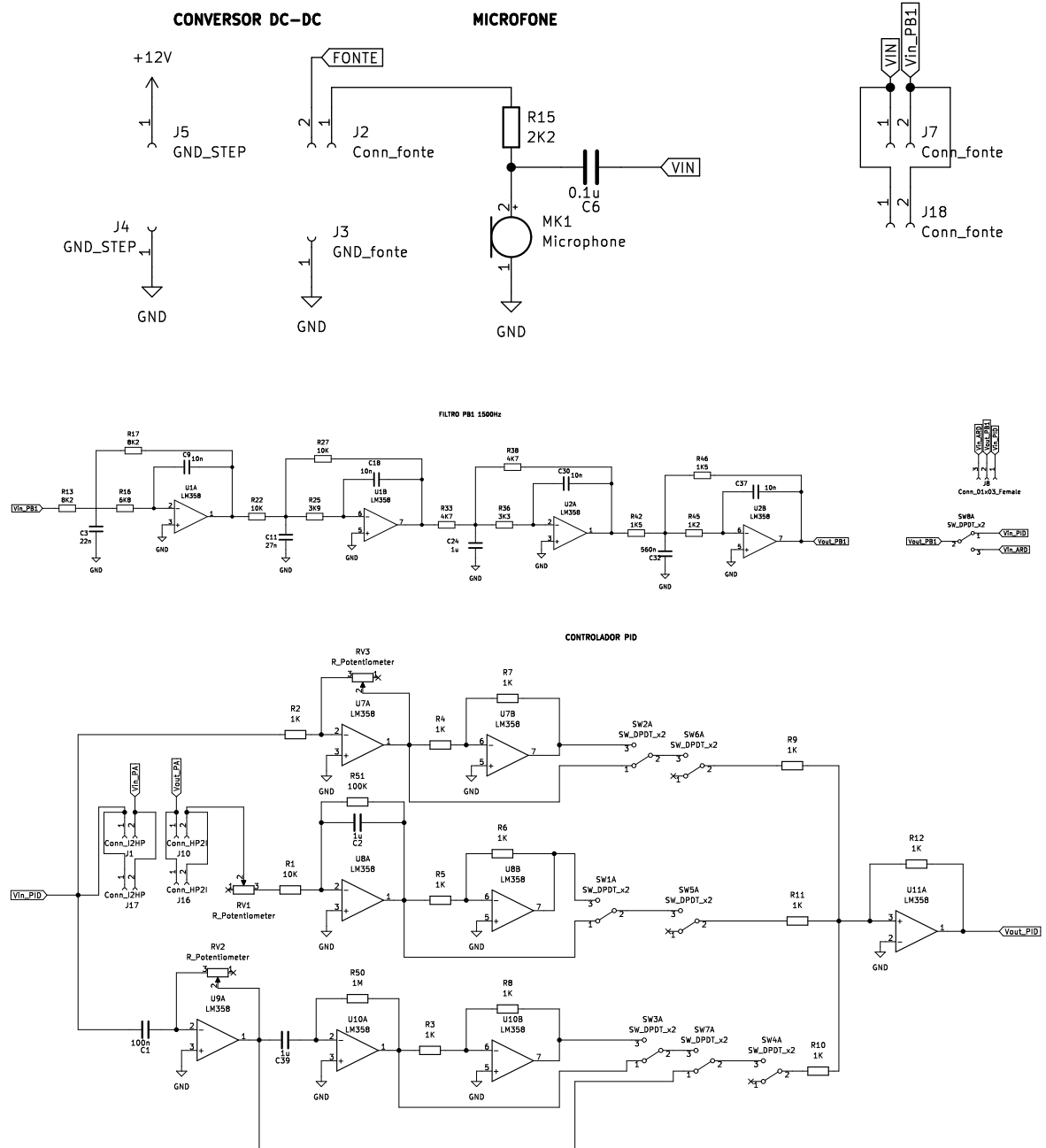
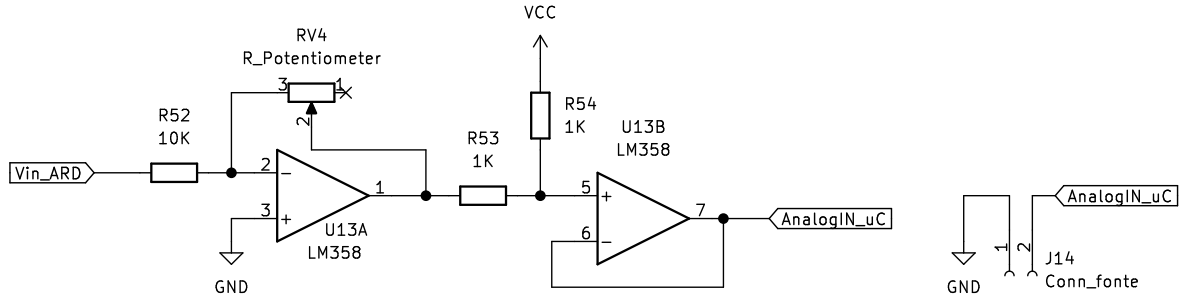
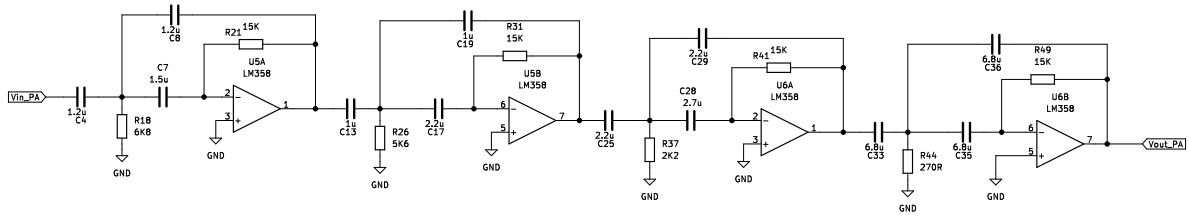


Figure C.2 – Scheme of the experimental platform.

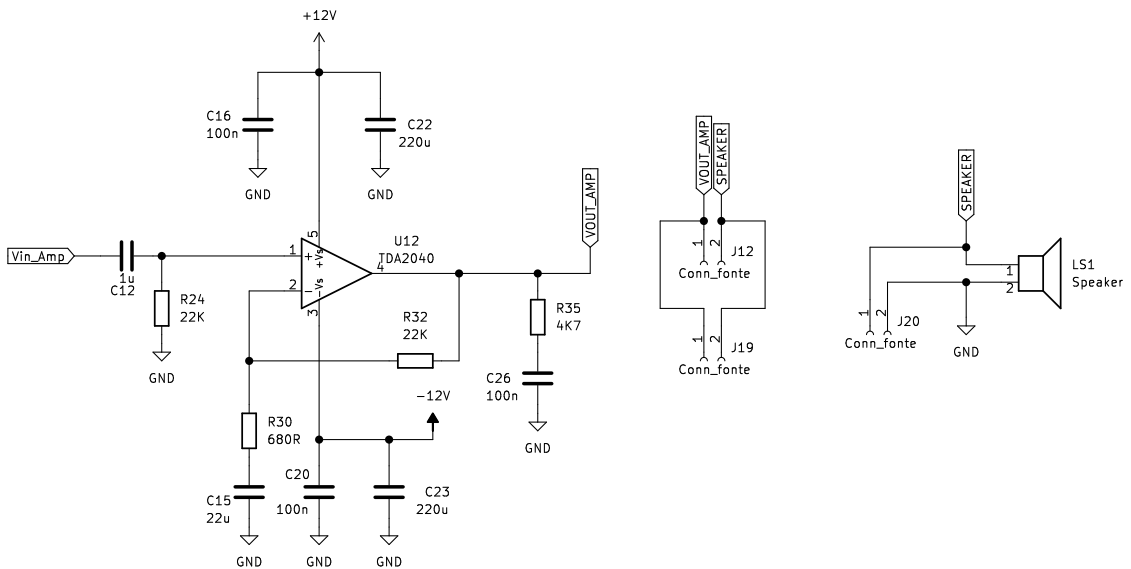
# ANNEX A – CIRCUIT IMPLEMENTATION FOR THE EXPERIMENTAL PLATFORM



FILTRO PA 10Hz (INTEGRADOR)



AMPLIFICADOR DE AUDIO



FONTES

